The Effects of Genetic Variant rs704 in the *VTN* Gene on the Pathobiology of Age-related Macular Degeneration (AMD)

Dissertation
zur Erlangung des Doktorgrades
der biomedizinischen Wissenschaften
(Dr. rer. physiol.)

der
Fakultät für Medizin
der Universität Regensburg

vorgelegt von

Fabiola Biasella

aus
Isernia (Italien)

im Jahr
2022

The Effects of Genetic Variant rs704 in the *VTN* Gene on the Pathobiology of Age-related Macular Degeneration (AMD)

Dissertation
zur Erlangung des Doktorgrades
der biomedizinischen Wissenschaften
(Dr. rer. physiol.)

der
Fakultät für Medizin
der Universität Regensburg

vorgelegt von

Fabiola Biasella

aus
Isernia (Italien)

im Jahr
2022

Dekan: Prof. Dr. Dirk Hellwig

Betreuer: Prof. Dr. Bernhard H.F. Weber

Tag der mündlichen Prüfung: 14.12.2022

Parts of this work have been published in peer-reviewed open-access journals:

Biasella F, Plössl K, Karl C, Weber BHF, Friedrich U. (2020). Altered protein function caused by AMD-associated variant rs704 links vitronectin to disease pathology. Invest Ophthalmol Vis Sci, 61(14):2. doi: 10.1167/iovs.61.14.2

Biasella F, Strunz T, Kiel C, on behalf of the International AMD Genomics Consortium (IAMDGC), Weber BHF, Friedrich U. (2022). Vitronectin and its interaction with PAI-1 suggests a functional link to vascular changes in AMD pathobiology. Cells, 11 (11):1766. doi.org/10.3390/cells11111766

Table of Contents

Zusammenfassung

Die altersabhängige Makuladegeneration (AMD) ist eine häufige Erkrankung der zentralen Netzhaut. Derzeit sind die Pathomechanismen der Krankheit nur unvollständig verstanden, was erfolgreiche therapeutische Strategien zur Bekämpfung der initialen Ereignisse der Krankheit wesentlich erschwert. In den letzten Jahren haben genomweite Assoziationsstudien (GWAS) eine Vielzahl von genetischen Variationen aufgezeigt, die sich auf bestimmte biologische Prozesse auswirken, wie z. B. die Organisation und Funktion der extrazellulären Matrix (ECM), die Komplementaktivierung und den Lipid-/Cholesterinstoffwechsel, die allesamt für die AMD eine wichtige Rolle spielen. Bis heute ist die molekulare und biologische Bedeutung der meisten AMD-assoziierten genetischen Varianten jedoch funktionell nicht geklärt.

In dieser Dissertation wurde eine funktionelle Untersuchung der AMD-assoziierten, nicht-synonymen rs704C>T-Variante im *VTN*-Gen, (ursprünglich reportiert von Fritsche und Kollegen, 2016), durchgeführt. Die rs704C>T-Variante führt zu einer Aminosäuresubstitution T400M im kodierten Vitronectin-Protein, einem zirkulierenden und matrizellulären Protein, das schon früher in die Pathologie der AMD als Schlüsselkomponente und koordinierender Faktor der abnormen extrazellulären Ablagerungen, die für die Krankheit charakteristisch sind, impliziert wurde. Hierzu wurde die nicht AMD-risikoassoziierte Vitronectin-Isoform VTN_rs704:C und die AMD-risikoassoziierte Isoform VTN_rs704:T in einer Reihe von *in vitro* Tests verglichen, um die Auswirkungen von rs704 auf die mRNA- und Proteinexpression, die Prozessierung und weitere funktionelle Aspekte von Vitronectin zu überprüfen.

Die Analyse der mRNA-Expression in retinalem Pigmentepithel (RPE), das aus humanen induzierten pluripotenten Stammzellen (hiPSC) differenziert wurde, und in Netzhautgewebe von Spendern, die heterozygot für rs704 waren, zeigte keine Auswirkung von rs704 auf die Transkription der beiden *VTN*-Isoformen. Nach heterologer Expression in humanen embryonalen Nierenzellen (HEK293-EBNA) und kultivierten RPE-Zellen (ARPE-19) wurde für die AMD-assoziierte Isoform VTN_rs704:T im Vergleich zur nicht AMD-assoziierten Isoform VTN_rs704:C ein dramatischer Anstieg der Proteinkonzentration und eine reduzierte endoproteolytische Prozessierung festgestellt.

Beide Vitronectin-Isoformen zeigten nach partieller thermischer Denaturierung eine ähnliche Suszeptibilität für den Trypsin-Verdau. Über Blue Native und nicht-reduzierende SDS-PAGE wurde gezeigt, dass beide Vitronectin-Isoformen eine ähnliche Multimerisierung aufweisen.

In Versuchen, welche die Bindung der beiden Vitronectin-Isoformen an Zellen adressierten, zeigte VTN_rs704:T im Vergleich zu VTN_rs704:C eine reduzierte Bindefähigkeit an die Zelloberflächen von ARPE-19, hiPSC-RPE und isolierten porcinen RPE-Zellen sowie an Y79-Retinoblastomzellen und humanen Nabelvenen-Endothelzellen (HUVECs).

Beide Isoformen von Vitronectin verstärkten in ähnlicher Weise die Adhäsion von porcinen RPE und ARPE-19 Zellen und führten zu einer Inhibierung des extrazellulären Signal-regulierten Kinase (ERK)-Signalwegs in ARPE-19-Zellen, wobei VTN_rs704:C hier eine stärkere Wirkung zeigte als VTN_rs704:T. In HUVECs reduzierten die Vitronectin-Isoformen Adhäsion und Tubulogenese, wohingegen nur die nicht risikoassoziierte Vitronectin-Isoform VTN_rs704:C die Migration dieser Zellen leicht reduzierte. Kein Einfluss von Vitronectin wurde auf die Regulierung des ERK-Signalwegs in HUVECs verzeichnet. Zudem zeigten beide Vitronectin-Isoformen Auswirkungen auf Autophagie und Zellviabilität von HUVECs und ARPE-19 Zellen.

Nach heterologer Vitronectin-Expression in ARPE-19 Zellen verbesserten die Vitronectin-Isoformen die extrazelluläre Ablagerung und das Clustering der integralen ECM-Komponenten Fibronektin, Elastin und Kollagen, aber nicht von Laminin. Darüber führten beide Vitronectin-Isoformen zu einer verstärkten extrazellulären Ablagerung des angiogenen Faktors VEGF und der Komplementkomponenten C9 und CFH, hatten aber keinen Effekt auf die extrazelluläre Ablagerung des Gewebsinhibitors der Metalloproteinasen-3 (TIMP3). Interessanterweise zeigte die risikoassoziierte AMD-Isoform VTN_rs704:T dabei eine stärkere Wirkung als die nicht risikoassoziierte Isoform VTN_rs704:C.

Schließlich wurde die Interaktion der Vitronectin-Isoformen mit dem Vitronectin-Bindungspartner Plasminogen-Aktivator-Inhibitoren (PAI-1), einem in der AMD-Pathologie involvierten Angiogenese-Regulator, untersucht. In Co-Präzipitationsexperimenten zeigte AMD-assoziiertes VTN_rs704:T eine stärkere Bindung an PAI-1 als nicht-AMD-assoziiertes VTN_rs704:C, wohingegen in Enzymaktivitätstests beide Isoformen die PAI-1-Aktivität auf vergleichbare Weise stabilisierten. Die Exposition von ARPE-19 Zellen und HUVECs mit VTN_rs704:C und VTN_rs704:T erhöhte in ähnlicher Weise die Expression und ECM-Ablagerung von PAI-1.

Zusammengefasst wird durch die Ergebnisse der Arbeit der Beitrag von Vitronectin zur Pathogenese der AMD unterstützt. Darüber hinaus werden neue biologische Wege aufgezeigt, über die dieses Protein die pathologischen Prozesse, die zu dieser schweren Krankheit führen, beeinflussen könnte.

Summary

Age-related macular degeneration (AMD) is a frequent disorder of the central retina. So far, the pathomechanisms of the disease are incompletely understood, precluding successful therapeutic strategies to address initiating events of the disease. In recent years, genome-wide association studies (GWAS) implicated a plethora of genetic variation affecting specific biological pathways, like extracellular matrix (ECM) organization and function, complement activation and lipid/cholesterol metabolism, as determinants of AMD. Still to date, for most genetic variants associated with AMD the molecular and biological significance remains to be functionally defined.

In this doctoral thesis, a functional investigation of the AMD-associated, non-synonymous rs704C>T variant within the *VTN* gene, originally reported by Fritsche and colleagues (2016), was conducted. This work aimed to explore the pathological significance of the amino acid substitution (T400M) resulting from rs704 in the encoded vitronectin, a circulatory and matricellular protein implicated previously in the pathology of AMD as a key component and coordinating factor of the abnormal extracellular deposits characteristic for the disease. To this end, the non-AMD risk-associated vitronectin isoform VTN_rs704:C and the AMD risk-associated VTN_rs704:T isoform were compared in a number of *in vitro* assays to assess the effects of rs704 on mRNA and protein expression, processing and functional aspects of vitronectin.

First, risk and non-risk associated *VTN* mRNA expression in human-induced pluripotent stem cells (hiPSC)-derived retinal pigment epithelium (RPE) and in retinal tissues from donors heterozygous for rs704 revealed no difference between the two *VTN* alleles. In turn, after heterologous expression in human embryonic kidney (HEK293-EBNA) and cultured RPE (ARPE-19) cells a dramatic increase in protein concentration and reduced endoproteolytic processing was found for the AMD risk-associated VTN_rs704:T isoform compared to the non-AMD risk-associated VTN_rs704:C isoform.

Second, after partial thermal denaturation both isoforms of vitronectin revealed similar susceptibility to trypsin digestion. Likewise, vitronectin isoforms exhibited an analogous multimerization, as demonstrated by Blue Native and non-reducing SDS-PAGE.

Third, in cell-binding assays, VTN_rs704:T relative to VTN_rs704:C showed a reduced ability to bind to the cell surfaces of ARPE-19, hiPSC-RPE and isolated porcine RPE cells, as well as to Y79 retinoblastoma cells and human umbilical vein endothelial cells (HUVECs). Both isoforms of vitronectin similarly increased the adhesion of porcine-derived RPE and ARPE-19 cells. Furthermore, the two isoforms of vitronectin inhibited extracellular signal-regulated kinase (ERK) signalling in ARPE-19 cells, with VTN_rs704:C showing a greater effect than VTN_rs704:T. In HUVECs, vitronectin isoforms reduced adhesion and tubulogenesis, while only the non-risk VTN_rs704:C isoform slightly reduced migration. The analysis revealed no

effect of vitronectin on the regulation of ERK signalling in HUVECs. Both isoforms of vitronectin failed to show any effect on autophagy and cell viability in HUVECs and ARPE-19 cells.

Fourth, after heterologous vitronectin expression in ARPE-19 cells, vitronectin isoforms increased the deposition and clustering of the integral ECM components fibronectin, elastin, and collagen, but not laminin. Furthermore, both isoforms increased the extracellular deposition of the angiogenic factor VEGF and the complement components C9 and CFH but had no effect on the deposition of the tissue inhibitor of metalloproteinase 3 (TIMP3). Interestingly, AMD risk-associated isoform VTN_rs704:T showed a stronger effect than non-risk-associated VTN_rs704:C.

Finally, the interaction of vitronectin isoforms with vitronectin binding partner plasminogen activator inhibitor 1 (PAI-1), an angiogenic regulator implicated in AMD pathology, was investigated. In co-precipitation experiments, AMD-associated VTN_rs704:T showed a stronger binding to PAI-1 than non-AMD-associated VTN_rs704:C, while in enzyme activity assays both isoforms similarly maintained PAI-1 activity. Exposure of ARPE-19 cells and HUVECs to VTN_rs704:C and VTN_rs704:T similarly increased expression and ECM deposition of PAI-1.

Taken together, the results of the thesis confirm and strengthen the contribution of vitronectin to the pathogenesis of AMD and suggest new biological pathways through which this protein might influence the pathological events leading to this devastating disease.

1. Introduction

1.1 Age-related Macular Degeneration

Age-related macular degeneration (AMD) is a neurodegenerative disorder of the retina, with pathological changes mostly pronounced in the central part termed the macula [1]. Emerging in a spectrum of clinical phenotypes, AMD is the leading cause of severe vision loss in individuals over 60 years of age in the developed world, accounting for 6-9% of legal blindness globally [1,2]. In the European population, the disease shows a pooled annual incidence of 1.4 per 1,000 people (95% confidence interval [CI] 0.8-2.6) [3], and it has been estimated that 3.9-4.8 million people in Europe will be severely affected by AMD by 2040 [2]. Three main elements are generally accepted as risk factors for AMD including increasing age, environmental factors (in particular smoking), and genetic predisposition [4-7]. The interplay between those factors defines AMD as a member of the so-called complex diseases. However, although several etiological possibilities have been formulated, AMD aetiology is far from complete, and much remains elusive about the pathophysiological events that culminate in the disease and how these are affected by genetic and environmental risk factors.

1.1.1 The Retina Under Healthy Conditions

In fundoscopic examination, a healthy retina appears orange-red in colour with a highly pigmented round spot in the macular centre, which has no visible blood vessels. The macula is located laterally and slightly below the optic disc, which can be distinguished as a pale pink region with sharp margins in which all retinal vessels converge [8] (**Figure 1A**). A vertical section through the healthy retina depicts a sophisticated multi-layered architecture (**Figure 1B**), in which different cell types work closely together to maintain retinal homeostasis and process visual information [9]. The neurosensory retina comprises specialised neurons interconnected by synapses and glial cells (Müller cells, astroglia and microglia), which support the structure and homeostasis of the retina [10]. Among neuronal cells, photoreceptors are responsible for the conversion of light into electrical stimuli (visual phototransduction) [11]. Two types of photoreceptors can be distinguished: rods, which specialise in processing dim light and contribute to black and white vision (scotopic vision), and cones, which are responsible for fine resolution and bright colour vision (photopic vision) [12]. The photoreceptor axons communicate with bipolar cells, which transmit signals from the photoreceptors to the retinal ganglion cells, whose axons meet in the optic nerve. The latter conveys the signal to the cerebral cortex. Laterally interconnected neurons, including horizontal cells and amacrine cells, modulate this flow of information [13]. On the outer side, photoreceptor cell bodies extend into a stack of membranous discs (outer segments) filled with rhodopsin, a pigment-containing protein that acts as a light receptor and drives phototransduction [11,14,15]. Supported

by the interphotoreceptor matrix [16], the outer segments of the photoreceptors are enclosed by microvillous structures of the underlying retinal pigment epithelium (RPE) [13].

RPE cells are densely packed, single-layered polarised epithelial cells. The apical microvillus of the RPE phagocytoses the outer segments of shed photoreceptors. This essential function ensures the maintenance of a relatively constant outer segment length, which is required for proper photoreceptor function [17-19]. Furthermore, the RPE plays a key role in both the regeneration and storage of retinoids, precursors of the visual pigment rhodopsin [20,21]. The cytoplasm of RPE cells abounds in pigment granules, including melanin, which absorbs the excess light from the photoreceptors and thus has the function of protecting the neuroretina from phototoxicity. Pigmentation of the RPE is also essential for focusing clear images onto the retina [19,22]. To maintain its own survival and the homeostasis of neural and vascular tissue in the retina, the RPE produces growth factors, including vascular endothelial growth factor (VEGF) [23], which promotes cell viability and regulates retinal vascular permeability and angiogenesis [24,25]. Laterally, RPE cells are connected by tight junctions [26]. This makes this layer act as a physical barrier limiting the transepithelial transport of ions, fluids, and metabolites to selective transport proteins within the apical and basal plasma membranes [27,28].

The RPE basal lamina is rich in collagen IV (non-fibrillar), fibronectin and laminin, and participates in the formation of Bruch's membrane, a 2-4 µm thick extracellular matrix (ECM)[29]. The remainder of Bruch's membrane consists of two structural collagen layers (inner and outer) rich in type I and III (fibrillar) collagen, which embrace the Bruch's membrane central layer mainly composed of elastin [29]. The choriocapillaris basement membrane, a labyrinth of thin-walled, fenestrated vessels forming the underlying choroid also is part of Bruch's membrane [29]. The function of Bruch's membrane is primarily that of a molecular sieve that regulates the diffusion of biomolecules between the choroid and the RPE. In addition, it provides physical support for RPE cell adhesion, also limiting the migration of choroidal and retinal cells [29,30].

Together with the RPE and Bruch's membrane, the endothelium of the choriocapillaris form the outer blood retinal barrier [31,32], which play a major role in rod and cone photoreceptor integrity. The choroidal circulation supplies oxygen and nutrients to the outer portion of the retina simultaneously removing metabolic waste products. In contrast to the outer retina, the inner retinal layers are mainly supplied and cleared by the retinal vasculature. The complex tight junctions of retinal capillary endothelial cells contribute to the formation of the inner blood retinal barrier [33,34].

In the macula, the retina is adapted for high acuity vision: The exceptionally high density of cone photoreceptors in the centre of the macular region (fovea) enables high-resolution vision [35]. Furthermore, RPE cells are denser, taller, and more pigmented than in the

periphery [36,37]. The extremely high metabolic demand associated with photoreceptor activity at a density above average make this region more vulnerable to oxidative stress, inflammatory events, and degenerative processes [35].
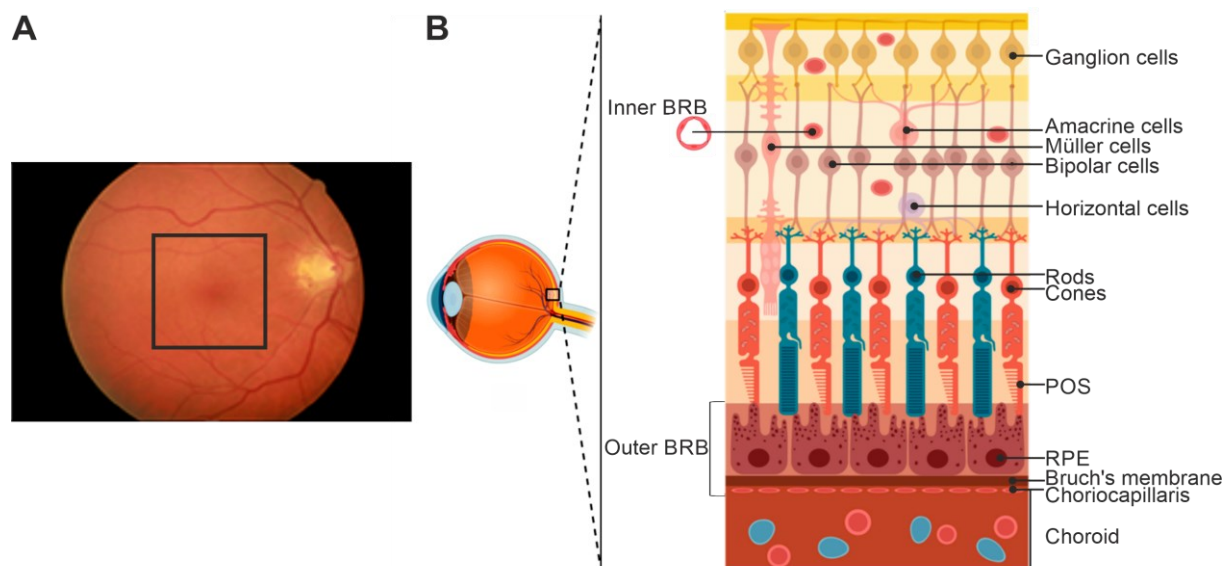
Figure 1: Overview of the healthy human retina.
Colour photograph of the fundus (**A**) and schematic illustration of the retinal layers (**B**) in a healthy condition. Square boxes highlight the macula. BRB, blood retinal barrier. POS, Photoreceptors outer segments. RPE, retinal pigment epithelium. (Fundus photograph modified from https://www.luxotticalearning.com.au/pages/luxottica-new-advances-in-the-imaging-and-management-of-age-related-macular-degeneration, accessed on 20 May 2022; Illustration of retinal layers modified from Jensen et al., 2020 [38]).

1.1.2 The Pathology of AMD

1.1.2.1 Clinical Findings

The first clinical manifestation of AMD is the appearance of abnormal extracellular deposits in the macula (known as drusen). On ophthalmoscopy, drusen appear as focal yellow polymorphic spots (**Figure 2**) [1]. Size and number of drusen are indicative of AMD initiation and stage: While the formation of small drusen (< 63 µm in diameter) manifests with ageing but does not represent a clinically relevant risk for developing AMD, medium-sized drusen (≥ 63 and ≤ 125 µm in diameter) are associated with early AMD (**Figure 2A**) and large drusen (> 125 µm in diameter), often associated with RPE pigment abnormalities, are considered a sign of intermediate AMD (**Figure 2B**) [39]. Immunohistochemical and proteomic studies have shown that drusen are mainly located between the basal membrane of the RPE and Bruch's membrane and contain a variety of proteins (e.g. circulating serum proteins, immunoglobulins, complement components, amyloid), different lipids (membrane phospholipids, cholesterol, neutral lipids), glycosaminoglycans and hydroxyapatite [40-43]. Furthermore, the appearance of basal laminar deposits (composed mainly of fibrous long-spacing collagen type VI and amorphous material) between the RPE and its basal lamina,

and linear deposits (composed mainly of lipoproteins and membranous material) in the inner collagenous zone of Bruch's membrane, is among the pathological changes seen in early AMD [44-48]. In addition to sub-RPE deposits, the formation of subretinal drusenoid deposits (SDD) between the apical processes of the RPE and the photoreceptors was observed in many patients, representing a risk factor for AMD progression independent of drusen [48-51]. The growth of subretinal deposits becomes more rapid in late-stage forms of AMD [52].

Two clinically distinct late-stage forms of AMD are described: Atrophic or "dry" AMD is characterised by geographic atrophy (GA-AMD), which reveals circumscribed macular areas in which RPE abnormalities become more pronounced and manifest as foci of hypopigmentation and/or hyperpigmentation, and atrophy. This is accompanied by loss of photoreceptors and of the underlying choriocapillaris membrane (**Figure 2C**). Furthermore, GA-AMD is associated with Bruch's membrane thickening, secondary to deposition of basal laminar and basal linear deposits, and scotoma [45,53]. The progression and enlargement of GA-AMD within the foveal region typically results in a precipitous decline in visual function [54].

The neovascular form of AMD (NV-AMD) is characterised by the abnormal growth of new blood vessels within the macula (**Figure 2D**) and comprises three subtypes. Type 1 is characterised by the growth of vessels initially from the choriocapillaris into and within the sub-RPE space. In type 2 (commonly called choroidal neovascularisation, CNV), neovascular events originate from the choroid and cross Bruch's membrane and the RPE monolayer and proliferate into the sub-retinal space. Finally, neovascularisation originates from the retinal vasculature in type 3 [55]. Typically, AMD-associated newly formed vessels are fragile and prone to leakage [56]. Consequently, exudative events including haemorrhage and fluid formation accompany the progression of exudative or "wet" NV-AMD, leading to diffuse cell loss, RPE or retinal detachment, retinal fibrosis and/or subsequent disciform scarring. Metamorphopsia (perception of distorted images) and vision loss appear very rapidly [57,58]. Non-exudative forms of NV-AMD characterised by the presence of new vessels in macular tissue without signs of exudation have also been reported and represent important predictor of exudative complications in NV-AMD [59].

AMD evolution from early to advanced stages varies from one patient to another [60,61], however, the reasons behind this variability have not been clarified so far. Of note, GA-AMD and NV-AMD are not necessarily mutually exclusive and can occur simultaneously in the same eye [62]. Also, GA is considered a relevant risk factor for the development of NV-AMD [63].
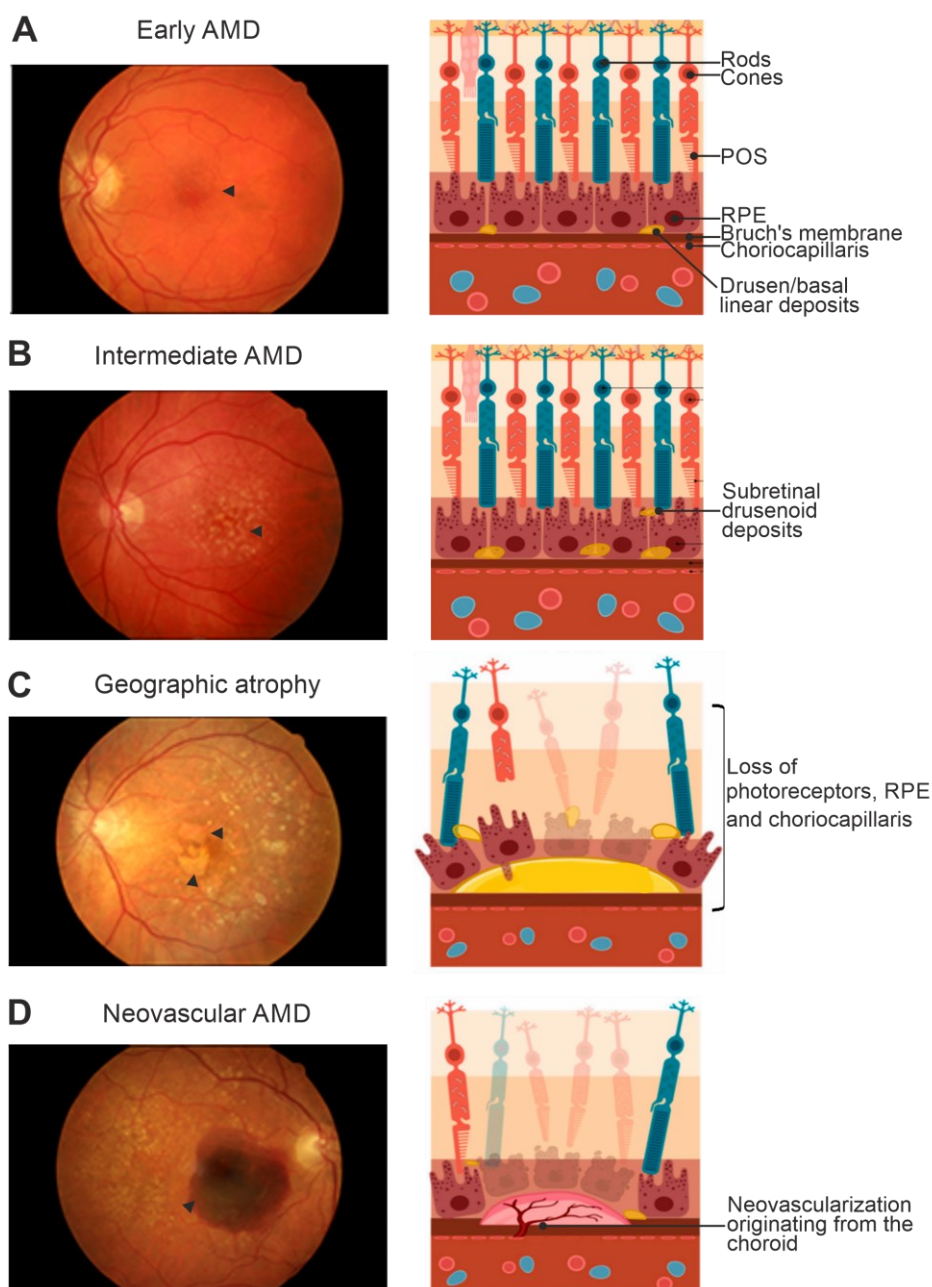
Figure 2: Retinal pathology associated with AMD subtypes.
(**A**) Early AMD with medium-sized drusen (black arrowheads in the fundus photograph). (**B**) Intermediate AMD with non-confluent large drusen and subretinal drusenoid deposits. (**C**) Geographic atrophy, extensive confluent drusen along the vascular arcades, growing subretinal drusenoid deposits and marked area of cellular atrophy (black arrowheads in fundus photograph). (**D**) Neovascular AMD, abnormal growth of blood vessels from the choroid plexus invading the overlying retinal layers and causing subretinal haemorrhage (black arrowheads in fundus photograph). Fundus photograph modified from https://www.luxotticalearning.com.au/pages/luxottica-new-advances-in-the-imaging-and-management-of-age-related-macular-degeneration (accessed on 20 May 2022); illustration of retinal layers modified from Jensen et al., 2020 [38].

1.1.2.2 Aetiology and Pathobiology

The molecular mechanisms that initiate the early formation of AMD-associated deposits and/or lead to progression of the disease in its more advanced stages are not fully understood. However, environmental conditions such as ageing and oxidative stress that accumulate in the eye over time have been implicated in the pathogenesis of AMD [64,65].

1.1.2.2.1 Age-related Changes of the Retina

The accumulation of metabolic debris and drusen may result from age-dependent changes in the RPE, which has long been suspected to be the primary site of pathology in AMD [66]. As a result of cumulative age-related oxidative damage, RPE cells decrease in concentration, probably due to increased apoptosis [67,68]. In aged RPE cells, reduced lysosomal capacity, impaired autophagy, and altered degradation of the photoreceptor outer segments result in the accumulation of intracellular metabolic debris, including non-degradable lipofuscin [69-71]. By reducing the pigment-free cytoplasmic space, the high lipofuscin content impairs cytoplasmic function of the RPE [72], e.g., phagolysosomal degradation of photoreceptor phospholipids [73,74]. In addition, the accumulation of lipofuscin and lipids, which are continuously exposed to light, enhance the production of reactive oxygen species (ROS) [75-77]. Defects then follow in oxidative stress-sensitive organelles, such as RPE mitochondria, eventually impacting cellular energy production and ultimately RPE function [78,79]. Oxidative damage and cellular senescence cause RPE cells to adopt a senescence-associated secretory phenotype, which involves the secretion of proinflammatory cytokines, chemokines, and growth factors such as VEGF [80-83]. Abnormal secretion of ECM components by dysfunctional RPE cells and deposition of cytoplasmic material in Bruch's membrane contribute to the age-associated impairment of Bruch's membrane [84,85]. Filamentous membrane debris, glycosaminoglycans, heparan sulphate, cholesterol and calcium phosphate increase their concentration in Bruch's membrane in adulthood, contributing to its thickening [30,86,87]. Furthermore, advanced glycation end products (AGEs) and fat accumulate in this layer [30]. This, together with the increase in collagen density and cross-linking in Bruch's membrane inner and outer collagen layers [88,89], participates in the reduction of the hydraulic conductivity of Bruch's membrane observed with advancing age [30,90]. Age-dependent changes in Bruch's membrane may also be related to an imbalanced regulation of matrix metalloproteinases (MMPs) and their tissue inhibitors (TIMPs), which play an essential role in the turnover of matrix components (including collagen, elastin, gelatin, matrix glycoproteins and proteoglycans) [85]. Finally, it has been reported that age-dependent changes in the choriocapillaris also play a causal role in the thickening of Bruch's membrane during ageing [64]: Senescence-associated stiffening of choroidal endothelial cells, reduction in choriocapillaris density and lumen diameter lead to a decrease in choroidal blood flow and loss of choriocapillaris cleaning function [88,91,92]. The observed changes in the RPE-Bruch's membrane-choroid complex contribute to chronic low-grade inflammation in the ageing retina [93].

1.1.2.2.2 AMD-related Changes of the Retina

The age-related processes in the retina coincide with those associated with AMD, although not every aged individual develops AMD [94]. The fact that 33% of the proteins derived from

drusen of AMD donors were not observed in drusen of healthy donors [41] appears to indicate that additional mechanisms may be involved in AMD pathology. Furthermore, while only small drusen (hard drusen) are formed during ageing, large drusen (soft drusen/basal linear deposits) appear during AMD, suggesting that typical debris clearance processes deteriorate over time but at an accelerated rate in AMD development [94].

Inherited genetic variation together with environment/lifestyle factors (e.g., cigarette smoking, obesity, hypertension) are thought to exacerbate and/or accelerate age-dependent changes and increase the risk of AMD [7]. For example, Bruch's membrane changes, particularly thickening, may worsen disease processes in AMD by a pathological alteration of ECM turnover due to an imbalanced secretion of proteins such as tissue inhibitor of metalloproteinase 3 (TIMP3) and activated MMP-2 and -9 in AMD [95,96]. Such alterations are likely dependent on individual genetic variability [4,97,98]. Also, an aggravated response to oxidative stress appeared in AMD compared to normal ageing, as indicated by significantly elevated oxidative stress markers (including malondialdehyde, protein carbonyl and 8-hydroxy-29-deoxyguanosine) and decreased antioxidant capacity in the serum of AMD patients compared to controls [99,100]. This, in turn, may lead to a culmination of age-related ultrastructural changes in RPE: When cultured on an extracellular substrate like that of AMD, primary RPE cells manifested altered ECM turnover, deposit formation, and complement activation [101]. Furthermore, RPE cells from AMD specimens showed a more pronounced mitochondrial dysfunction than age-matched controls [102], the extent of which is thought to be determined by genetic variability of mitochondrial and nuclear DNA repair enzymes [103,104]. In addition, RPE cells from AMD donors showed increased accumulation of lipid droplets and glycogen particles, as well as impaired autophagy function [105]. The increased oxidative stress in RPE cells might lead to increased secretion of growth factors such as VEGF, which may amplify normal age-associated changes and promote retinovascular complications in AMD [106,107]. In line with this, an increased concentration of VEGF has also been measured in the ocular fluid and serum of AMD patients [108,109].

Choroidal density and diameter decrease with age in healthy human eyes; however, these changes appeared more pronounced in eyes with AMD near regions of basal laminar deposits, GA or disciform scars [88]. This, together with a notably reduced choroidal blood flow as seen in patients with AMD [110-112], would be sufficient, according to the vascular theory of AMD [113], to initiate RPE dysfunction, accumulation of metabolic debris and drusen formation. Moreover, the decreased choroidal perfusion may lead to ischaemic/hypoxic damage and increased oxidative stress, which could signal the initiation of abnormal choroidal neovascularisation [113,114]. Inevitably, the inflammatory processes that begin in ageing become increasingly active in AMD and include complement and glial activation, as well as macrophage infiltration [115,116]. Increased activation of these pathways results in an increased

pro-inflammatory response that includes the generation of membrane attack complexes (MACs) mediating cell lysis, the release of chemokines to attract inflammatory cells to the site of damage and increased choroidal endothelial permeability to promote the overflow of infiltrating leukocytes [117]. In recent years, genetic association studies have identified polymorphisms in genes encoding complement factors as being associated with AMD and suggested a role for complement dysregulation in disease pathogenesis [118,119]. In line with this, serum concentrations of a number of complement components were higher in AMD patients. Furthermore, in contrast to age-matched control eyes, AMD eyes exhibited an increased immunoreactivity against the inflammatory C-reactive protein in the RPE/Bruch's membrane/choroid complex, whereas significantly less immunoreactivity for the major soluble complement inhibitor, complement factor H (CFH) [120]. Likewise, serum pro-inflammatory cytokines (e.g., IL-22) were significantly increased in AMD patients compared to age-matched controls [121]. Finally, age-related impairment of glial cells (Müller cells, astrocytes) has also recently been discussed as a potential initial cause of deficient retinal homeostasis and AMD development [122-124].

1.1.3 Treatment and Emerging Therapies in AMD

The incomplete understanding of AMD pathogenesis and the heterogeneity of its phenotypic expression has slowed the development of effective therapies. The use of therapeutics that inhibit VEGF, a key mediator of choroidal neoangiogenesis [125], has become the gold standard of treatment for NV-AMD, however only allowing temporary effects of improvement of exudative damage in the retina. Available on the market in the early 2000s, these inhibitors replaced laser therapy approaches previously used to ablate abnormal blood vessels [126-128]. Although different anti-VEGF agents are available nowadays, including antibodies and recombinant receptor-like proteins, the need for repeated intravitreal injections, recurrences and large variability in response are burdensome for patients [1,129]. Several clinical trials are currently testing gene therapy approaches for the sustained delivery of a range of angiostatic proteins [130]. Of interest, subretinal or intravitreal delivery of adeno-associated virus (AAV) vectors expressing soluble VEGF-neutralizing proteins has been shown to be safe in clinical trials [131,132]. Since multiple pathogenic pathways such as angiogenesis, complement activation and inflammation are involved in NV-AMD, multitarget gene therapy strategies addressing multiple genes or proteins are gaining increasing interest [133].

Unlike for NV-AMD, there are no approved therapeutic options for GA-AMD. Given the known involvement of abnormal complement system activation in the pathogenesis of AMD [134], many clinical trials are underway to investigate the effect of complement-targeted therapies to halt or delay disease progression to the atrophic form. These include the use of complement C3 and C5 inhibitors [135,136], as well as AAV-mediated supplementation of

complement factor inhibitor (CFI) [137]. In addition, neuroprotection, visual cycle modulators, cell-based therapies and anti-inflammatory agents are currently under investigation [129].

1.2 The Genetics of AMD

The role of genetics in AMD development is supported by several lines of evidence, including increased risk of AMD among the relatives of patients [138,139] and twin pairs, with higher disease rates in monozygotic than in dizygotic twins [140,141]. Furthermore, genome-wide linkage screens, candidate gene studies and genome-wide association studies (GWAS), have identified multiple genetic variants that influence AMD susceptibility [142,143]. Based on genome-wide genotyping data, GWAS compare in a hypothesis-free approach the allelic frequency of hundreds of thousands of genetic variants, particularly single nucleotide polymorphisms (SNPs), between a large cohort of probands with a given trait or disease (cases) and healthy controls. This allows the identification of genomic regions harbouring DNA sequence variations that are statistically associated with the disease or trait of interest [144]. Through these studies, precise information has been obtained on the genomic location of genetic variants that may influence susceptibility to AMD. Using only 50 controls and 96 cases, the first GWAS for AMD identified genetic variants around the *CFH* gene to be reproducibly associated with AMD [118]. This initial study was followed by several GWAS, which included an increasing number of individual DNA samples, consequently revealing additional AMD-associated loci [145]. The currently largest GWAS for AMD was published in 2016 by the International AMD Genomics Consortium (IAMDGC), which compared >12 million variants between 16,144 patients with advanced AMD and 17,832 controls in a European cohort [119]. In this study, 52 independent genetic variants across 34 loci were found to be linked to the AMD phenotype with genome-wide significance ($p < 5 \times 10^{-8}$) (**Figure 3**). Despite these advances, for most of the associated variants the molecular and biological significance remains to be functionally clarified.
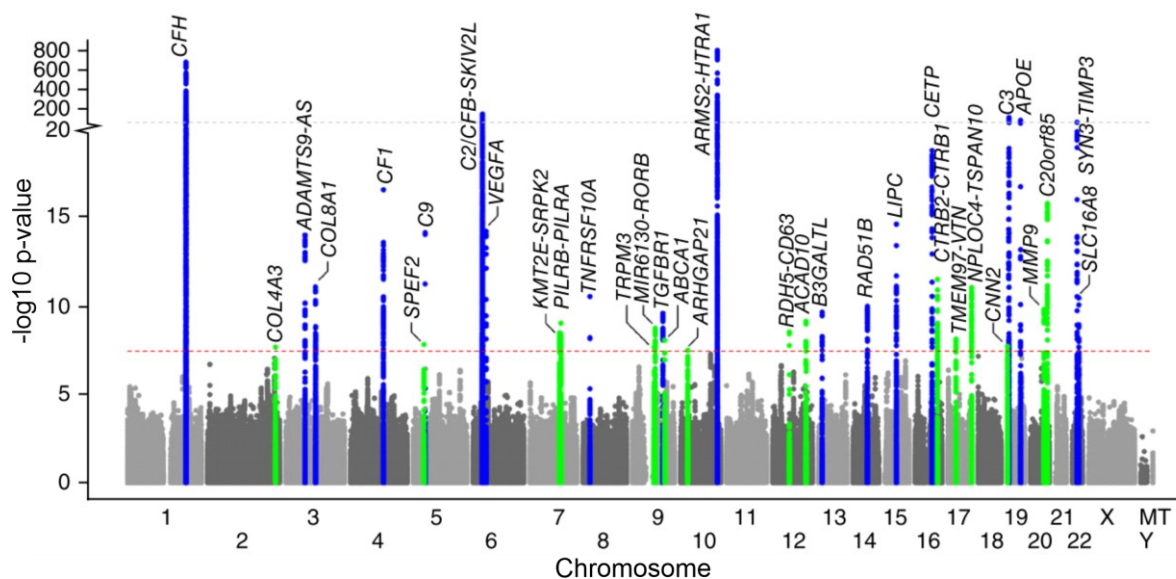
Figure 3: AMD-associated loci from the International AMD Genomics Consortium (IAMDGC) GWAS.
Genome-wide single variant association analysis for >12 million variants in 16,144 advanced AMD patients vs. 17,832 controls. Shown is the Manhattan plot exhibiting p-values for association. The horizontal red line indicates genome-wide significance ($p < 5 \times 10^{-8}$). In green novel genome-wide significant loci associated with AMD, in blue previously known AMD loci. Despite the great potential of the analysis, for most of the associated variants within susceptible loci the molecular and biological significance remains to be functionally investigated. (Figure taken from Fritsche et al., 2016 [119]).

1.2.1   From GWAS-associated Genetic Loci to Causal Susceptibility Variants

GWAS susceptible loci are typically named after the gene(s) showing the closest physical proximity to the genetic variant revealing the most significant association with the disease or trait of interest (the so-called lead variant) (**Figure 3**). These loci typically include multiple variants that may contribute to the association signal. Very often these variants are in linkage disequilibrium (LD) with each other, which tend to be inherited together during the meiotic recombination process [146-148]. LD results in multiple variants present within a certain locus by virtue of this correlation. The LD structure of genetic loci is exploited by GWAS studies to impute subsets of SNPs in addition to those directly interrogated by genotyping. This results in the availability of genetic markers that tag (or co-occur with) actual associated variants in complex traits [148,149]. However, the phenomenon of LD makes it difficult to identify variants that specifically underlie the association signal at a GWAS-associated locus (causal variant) from the physically close non-causal variants in LD [148,150].

The determination of the actual causal variant is fundamental to obtain biological insights from the list of associations provided by GWAS, allows to identify target genes and, especially, to connect causal variants and target genes to molecular, cellular, and physiological phenotypes. In order to assess the contribution of each variant to the association signal detected by GWAS, a dissection of a GWAS-identified locus aimed at clarifying the relationship between identified variants is crucial [151]. Numerous post-GWAS analysis strategies, including statistical methods and functional genomic annotations, have been widely applied to prioritise causal variants (referred to as fine mapping) and their target

genes [151,152]. Statistical approaches focus mainly on the strength of the association signal [151,152]. Conditional analysis of the regional variants is often used to estimate the number of variants at a susceptible locus that are associated with disease or trait of interest independent from each other. The conditional approach is based on an iterative association analysis of most GWAS-identified variants that include lead or other selected variants as covariates. If a neighbouring variant remains significant, it is interpreted as a distinct association signal [153]. Variants related to independent association signals identified by conditional analysis can be further sorted based on their respective p- or LD values. A common approach is to consider, for example, all SNPs with a p-value below 5×10^{-8} (standard p-value for genome-wide significance) as candidates for causality [154]. Alternatively, posterior probabilities of causality can be assigned to each variant of a given locus using the Bayesian method. This approach assumes that each locus associated with GWAS harbours exactly one causal variant and provides minimal sets of variants that contain the causal variant with 95% probability (95% credible interval) [154,155].

Fine mapping is followed by a full mechanistic analysis of a GWAS-identified locus to identify the immediate effects of causal variants, the gene(s) involved in the locus that mediate the disease association, and the downstream effects on networks or pathways that lead to changes in cellular and physiological function [156,157]. Only 2-3% of GWAS hits fine-map to coding variants [144]. Such variants are a first choice to be considered for causality, as they are expected to change the amino acid sequence of an encoded protein with structural and functional implications. The causative gene candidates and underlying molecular mechanism can thus be suggested based on the genomic position and the type of the coding variant (e.g., non-synonymous, nonsense, or frameshift variant) [156,158]. Non-coding variants including intragenic or deep-intronic, mostly cannot be directly linked to a causative candidate gene, making interpretation of possible functional consequences difficult [159,160]. These variants are thought to exert regulatory effects on target gene expression through mechanisms such as promoter modification and enhancer or silencer activity [160]. Colocalization of non-coding variants with genomic regulatory regions, e. g. by correlation analysis between those variants and gene expression (known as eQTL analysis), DNA methylation or transcription factor binding makes it possible to link non-coding variants to their target genes and reveal their potential functional consequences [144,156,161,162] Finally, pathway enrichment analyses assess overrepresentation of a group of functionally related SNPs or genes in particular biological pathways and serve to evaluate signals that might be biologically significant but are overlooked among numerous potentially false positive signals [163].

Statistical fine mapping and functional annotation of GWAS findings have so far revealed a variety of candidate variants and genes of potential relevance to AMD pathogenesis. These include genes related to ECM organisation and function, key regulators in immune defence,

as well as lipid/cholesterol metabolism and trafficking [119]. Experimental functional analyses of these candidate genes are mandatory to unequivocally establish their causality.

1.2.2 Genetic Variant rs704 and Its Association With AMD

Among the SNPs successfully genotyped in the GWAS by Fritsche and colleagues, the non-synonymous variant rs704, located within the *VTN* gene on chromosome 17 (17q11.2), was strongly associated with AMD (p= 1.71 × 10^{-7}) [119]. In the European population, rs704 represent a common polymorphism with an estimated gene frequency of about 51% for the ancestral C allele and 49% for the alternative T allele [164].

Found in high LD ($r^2 > 0.6$) with lead variant rs11080055 located in intron 1 of the *TMEM97* gene (**Figure 4**), rs704 is part of a 95% credible set of 22 genetic variants at the AMD-associated *TMEM97-VTN* locus. Within this 95% credible interval, rs704 is the only missense and protein-altering variant, thus receiving a high priority score for SNP causality. Located in exon 7 of the *VTN* gene, variant rs704 leads to a cytosine (C) to thymine (T) substitution at nucleotide position 1199, resulting in a threonine to methionine amino acid exchange at amino acid position 400 (T400M) of the encoded vitronectin protein. Given the previously reported detection of vitronectin in AMD-related retinal tissues and deposits [42,165,166], this variant appeared to be an excellent candidate for targeted functional analysis.
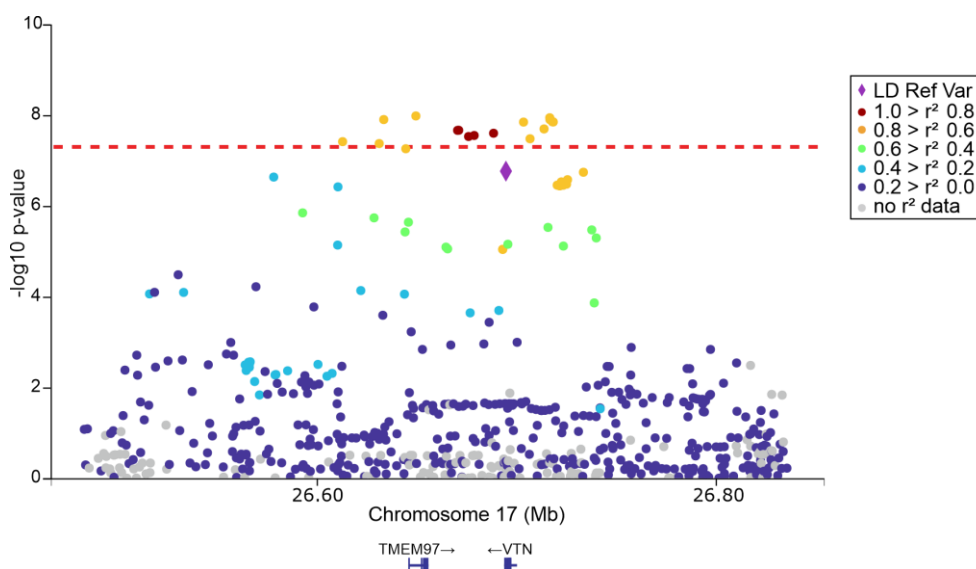
Figure 4: Association of genetic variant rs704 with late-stage AMD.
The rs704 association signal within the *TMEM97/VTN* locus were plotted using LocusZoom [167] and the GWAS summary statistics published by Fritsche and colleagues [119]. Each dot represents a genetic variant and is plotted according to its AMD association displayed by its -log10 (p-value). The horizontal red line indicates genome-wide significance (p < 5 × 10^{-8}). Variant rs704 is presented as a purple diamond and serves as a reference linkage disequilibrium (LD) variant. LD between variants is symbolised by a range of colours from red (complete LD, r^2=1) to dark blue (no LD, r^2=0). Transcript map with direction of transcription is given at the bottom. (LocusZoom plot was exported and modified from https://my.locuszoom.org/gwas/894486/region/?chrom=17&start= 26194861&end=27194861, accessed on 9 May 2022).

In addition to AMD, rs704 has been linked to other traits, such as vascular tumours in patients with the Von Hippel–Lindau gene defect [168], altered concentration of circulating

lipoproteins and apolipoproteins with risk of coronary artery disease [169,170], as well as radiation pneumonitis in lung cancer patients [171]. Furthermore, normal cognitive processing and blood pressure were also associated to rs704 [172,173].

1.3   Vitronectin

The genetic variant rs704 causes an amino acid substitution in vitronectin, a secreted glycoprotein abundant in human blood plasma (0.2-0.5 mg/ml), e.g., as a component of high-density lipoproteins [174,175], and in the ECM of various tissues, including the retina [29,176-178].

1.3.1   Vitronectin Expression, Structure and Processing

While vitronectin is mainly synthesised in the liver [179], it is also expressed in the brain [180], in vascular smooth muscle cells [181] and in the retina [165,182]. The full-length protein comprises 478 amino acids. It contains a signal peptide (the first 19 amino acid residues) which is cleaved off during cellular secretion. Secreted mature vitronectin comprises 459 amino acids organised in several structural domains (**Figure 5**), including three N-glycosylation motifs and potential sites for sulphation and post-translational phosphorylation interspersed within the domain structure of vitronectin [178,183]. The first 44 amino acids at the N-terminal site of the mature protein form the somatomedin domain (SMD), with a partial 3_{10}-helix and a single turn α-helix as its classical secondary structural elements [184]. The SMD motif mediates the binding of vitronectin to plasminogen activator inhibitor 1 (PAI-1) [185,186] and urokinase plasminogen activator receptor (uPAR) [187]. This enables vitronectin regulation of PAI-1- and uPAR-associated biological processes, such as haemostasis, angiogenesis, cell adhesion and motility [186,188,189]. Next, an arginine-glycine-aspartate (RGD) motif follows, which represents the main vitronectin binding site for integrin receptors [190], and thus the cell attachment site. Through RGD-mediated integrin binding, vitronectin activates intracellular signalling pathways, including the MAP kinase pathway which regulates cell adhesion, spreading, migration, proliferation, and apoptosis [191-194].

The major proportion of vitronectin is composed of three variable regions and four hemopexin (HX)-like repeats that fold as a single four-bladed β/α thruster, known as the HX domain [195]. The variable regions exhibit low conservation and low conformation order. Variable region 1 (amino acid 66 to 154) hosts a binding site for collagen and heparin, as well as phosphorylation, sulfation, and N-glycosylation sites [178,195,196]. Furthermore, an additional site for PAI-1 binding was recently reported within this region [197,198]. Variable region 2 (amino acid 283 to 324) is only slightly variable and located very close to thrombin cleavage sites. Variable region 3 (amino acid 355 to 435) shows high variability and contains a furin cleavage site at residue R398 [195]. It also harbours binding sites for heparin [195], complement component C9, plasminogen, PAI-1 and the thrombin/antithrombin complex [199-201]. *Via* the HX domain, vitronectin binds to soluble ionic calcium and crystalline

hydroxyapatite [202]. Calcium binding by vitronectin was recently proposed to be crucial in the formation of abnormal extracellular deposits, such as those associated with AMD [202]. Among complement factors, vitronectin also binds the terminal complement complex C5b-7, however the domain used by vitronectin for this interaction is debated and has so far implicated both the heparin and non-heparin binding sites [178,203]. Near the RGD domain and within the C-terminal portion, vitronectin additionally possesses binding domains for several bacterial pathogens [196].

The full-length three-dimensional structure of the vitronectin protein has not yet been experimentally resolved [197]. Crystallographic studies are challenged by the conformational lability and heterogeneity of vitronectin both *in vitro* and *in vivo*. The protein normally circulates as a mixture of single-chain and disulphide cross-linked two-chain form which is produced by furin-mediated cleavage on the carboxy-terminal side of R398 [204] consisting of a heavy chain (65 kDa) and a C-terminal light chain of approximately 10 kDa molecular weight [204] connected *via* a disulphide bridge between C293 and C472 [178]. Recently, Shin and colleagues proposed that the two-chain form of vitronectin is further maintained by the central structure of its HX domain, with the chains linked by disulphide bonds between C156 and C472 [195]. Moreover, although the majority of circulating vitronectin is monomeric, the tissue form of the protein adopts an altered, multimeric conformation [205]: Unfolding of vitronectin due to protease activity and/or physical binding with specific interaction partners results in self-association into multimeric aggregates. Such higher ordered forms of vitronectin were specifically detected in the ECM and within platelet α-granules [205,206]. The multimeric state reveals previously cryptic sites that enhance vitronectin activity [205,207]. As a result, the multimeric form of vitronectin represents a more potent molecule, binding to ligands with higher affinity than native vitronectin [208]. Finally, extensive posttranslational modifications (e.g., N-linked glycosylation, phosphorylation, and sulphation) increase the structural heterogeneity of this protein [183].
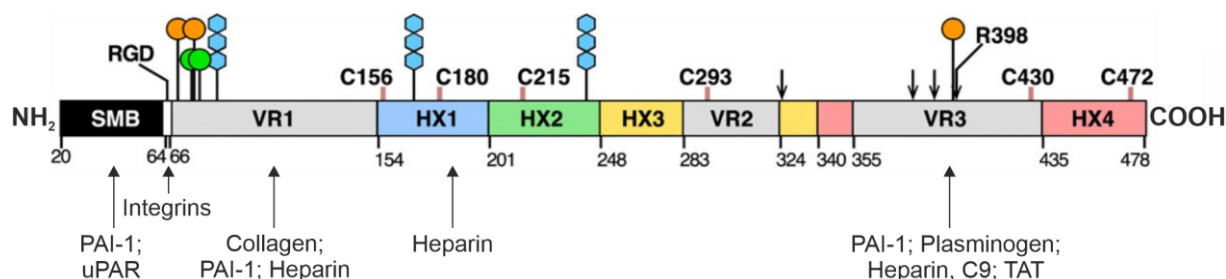
Figure 5: Domain organization of vitronectin.
Representation of vitronectin domains: the somatomedin domain (SMB) (in black), the RGD sequence (in white), the four hemopexin domains (HX) (in blue, green, yellow, and pink) and the three variable regions VR1 to VR3 (in grey). Also shown are the cysteines (C) (pink lines) and the sites of phosphorylation (orange circles), sulphation (green circles), N-glycosylation (blue hexagons) and cleavage by proteases (arrows). Binding sites for vitronectin interaction partners are indicated for each domain and involve binding for plasminogen activator inhibitor 1 (PAI-1), urokinase plasminogen activator receptor (uPAR), integrin receptors, collagen, heparin, plasminogen, complement factor 9 (C9) and thrombin/antithrombin complex (TAT). (Figure modified from Shin et al., 2019 [195]).

1.3.2 Functionality of Vitronectin

Vitronectin functions as a potent matricellular factor, coordinating a variety of cellular processes like cell adhesion, migration, angiogenesis, complement activation, tissue remodelling and growth factor signalling at the cell-ECM interface [177,178], all processes which have also been associated with AMD pathogenesis [134,209-211].

Extracellular vitronectin acts as a bond between cells and ECM promoting cell attachment to the ECM [178]. These adhesive properties are mediated by the binding of vitronectin to cellular transmembrane integrin receptors. After vitronectin binding to these receptors, actin microfilaments of the cytoskeleton connect to integrin to form focal adhesions and evoke a molecular clutch [178,212]. On the other hand, vitronectin also promotes cell adhesion in an integrin-independent manner. By binding to the urokinase receptor uPAR, vitronectin triggers a crosstalk between these receptors and integrins upon membrane tension, also resulting in integrin activation and subsequent focal adhesion formation [213,214]. Furthermore, binding of vitronectin to cell surface-associated proteoglycans also appears to stimulate cell adhesion [178]. Through its adhesive properties, vitronectin is supposed to regulate many cellular processes, including the maintenance of endothelial barrier function [215,216], the role of adherent leukocytes enhancing the chronic inflammatory phase [217,218], or tumour development and progression [219,220].

Through binding to integrin $\alpha v\beta 3$ on endothelial cells, vitronectin has been observed to activate vascular endothelial growth factor receptor 2 (VEGFR-2), thereby contributing to the regulation of angiogenesis mediating processes such as adhesion, migration, and proliferation [221]. In line with this, binding of vitronectin to integrins and uPAR appears to be required for the survival and maturation of new blood vessels in several vascular beds, including the retina [177,222].

Vitronectin is furthermore involved in regulating the terminal pathway of complement activation to limit the self-reactivity of the innate immune response [178]. Specifically, it binds to complement proteins C5b-7 and C9 to prevent their cell membrane insertion and polymerisation, respectively. This ultimately prevents the formation of the membrane attack complex (MAC) and thus the creation of cytotoxic pores on the cell surface [178,201]. This process may be particularly important in vitronectin-rich sites (i.e., the vessel wall), implying that these sites may be protected from autologous complement attack [178]. In addition, vitronectin mediates complement escape and cell invasion of microbial pathogens that recruit vitronectin to their cell surfaces by exploiting its adhesive properties [196,223].

Through interaction with the urokinase plasminogen activator (uPA), its receptor uPAR, integrins and PAI-1, vitronectin is also part of the plasminogen activation system, an extracellular proteolytic enzyme system involved in the regulation of cell migration, fibrinolysis, ECM degradation, tissue remodelling and inflammation [224]. Specifically, the

binding of uPA to uPAR promotes extracellular proteolysis by activating plasmin from inactive plasminogen. Once activated, the plasmin system causes the degradation of fibrin (fibrinolysis), several blood clotting factors and ECM components, including also vitronectin [224]. Binding of vitronectin to uPAR promotes cell adhesion and migration in a uPA-stimulated manner [213,225].Through allosteric modulation, vitronectin prolongs the half-life of PAI-1, the major inhibitor of uPA [226]. PAI-1 competitively displaces adhesion receptors from vitronectin, and thus can detach cells from ECM [227-229].

Finally, vitronectin also regulates blood system-related protein cascades such as coagulation and fibrinolysis through its interaction with heparin and thrombin-antithrombin III [177,230]. In the presence of vitronectin, the antithrombotic and procoagulant functions of heparins and thrombin are neutralised [177,230]. This is in addition to the enhanced thrombin-inhibiting properties of PAI-1 resulting from the interaction of PAI-1 with vitronectin [177].

1.3.3 Contribution of Vitronectin to AMD Development

In the retina, vitronectin mRNA expression was detected in the RPE, photoreceptors and ganglion cells [165,166], with higher expression in the neural retina than in the RPE [231]. However, extracellular detection of vitronectin protein in the retina was mainly restricted to Bruch's membrane and the retinal vasculature [165]. In particular, the inner collagenous layer of Bruch's membrane [29] and the basement membrane of endothelial cells [232] contain significant amounts of vitronectin. During AMD development, altered vitronectin expression and deposition in the retina was described: Retinal tissue sections from donors with a clinical diagnosis of atrophic AMD showed significant vitronectin immunoreactivity in the cytoplasm of RPE cells [233]. Furthermore, manifold immunocytochemical and proteomic analysis of human eye donor tissues supported the localisation of vitronectin in drusen and suggested this protein as the main constituent and marker of extracellular deposits associated with AMD, but also with Alzheimer disease, atherosclerosis, and other degenerative disorders [40-42,166]. Recently, Dr Marassi's group suggested that the ability of vitronectin to bind soluble calcium ions and mineralised hydroxyapatite is the initiating factor in the formation of abnormal calcified protein-lipid extracellular deposits that accumulate with AMD progression [202]. Additionally, although vitronectin was also visualised in areas of intact RPE without drusen, the greatest immunoreactivity was reported in RPE cells flanking or overlying drusen and in small sub-RPE deposits containing RPE cell debris [233]. Consistent with this, vitronectin mRNA expression was increased in hiPSC-RPE cells generated from patients with a history of AMD compared to cells derived from healthy donors [234].

In addition to AMD-associated alterations of vitronectin expression and deposition in the retina, mass spectrometry-based expression analysis of plasma proteins from 255 AMD patients and 221 controls revealed an association between altered plasma vitronectin concentrations and AMD [235]. Finally, an upregulation of vitronectin in the aqueous humour of

patients with NV-AMD with little or no response to anti-VEGF treatment was detected in comparison to the healthy control group, suggesting an involvement of this protein also in biological events underlying vascular complications in AMD [236].

1.3.4 Effect of rs704 on Vitronectin

Only few studies addressed the impact of rs704 on vitronectin: In 1990, Tollefsen and colleagues showed that rs704 affects the cleavage of vitronectin *in vivo* [237]. Specifically, the rs704-induced amino acid exchange T400M renders vitronectin less susceptible to proteolytic cleavage at R398 [237]. This leads to an increase in the 75 kDa single-chain form of the protein and to a reduction in the cleaved, disulphide-bound two-chain form composed of the 65 kDa and 10 kDa subunits [237-239]. These two physiological isoforms of vitronectin revealed a distinct conformation as suggested by different susceptibility to protein kinase A, an enzyme which phosphorylates vitronectin in plasma [240]. Chain and colleagues reported that protein kinase A can only phosphorylate the single-chain form but not the two-chain form of vitronectin, due to burial and inaccessibility of the phosphorylation site in the two-chain form [239,241]. However, after binding of the two-chain vitronectin to heparin [242], the phosphorylation site becomes exposed and capable to undergo phosphorylation at physiological pH [239,241]. Finally, a proteomic analysis of human plasma from 3,301 individuals revealed an impact of rs704 on vitronectin protein expression in blood, which identified this polymorphism as a protein quantitative trait locus (pQTL) [243].

1.4 Aim of the Study

Despite considerable research efforts, the aetiology of AMD is far from being fully understood, and much remains elusive about the pathophysiological events that lead to the disease. Although GWAS studies strongly suggest the contribution of genomic variation in AMD susceptibility, the translation of GWAS findings into clinical aspects of the disease is limited by the difficulty of interpreting GWAS results and the notable lack of follow-up laboratory studies of suggested causal candidate variants/genes [244]. A functional validation of the causal variants and their targets would facilitate the understanding of the molecular and cellular mechanisms of the disease and would allow the identification of useful biomarkers for preventive and/or therapeutic purposes. To this end, the present study aimed to explore the functional meaning of the statistical association of *VTN*-related genetic variant rs704 with AMD and by that to provide a deeper insight into the contribution of the two vitronectin isoforms to AMD pathology. Based on a comparison of the non-AMD risk-associated vitronectin isoform (VTN_rs704:C) and the AMD risk-associated isoform (VTN_rs704:T), this study first assessed the impact of rs704 on vitronectin protein expression, secretion, processing, stability, multimerization, as well as the ability to bind to cell surfaces. In addition, the role of vitronectin and the impact of rs704 on vitronectin functionality were followed in

AMD-associated cellular processes such as cell adhesion, autophagy, viability, migration, and ECM deposition. Finally, the impact of rs704 on the interaction of vitronectin with its interaction partner PAI-1 was studied. The results of these investigations will provide a basis for further understanding one aspect of AMD pathogenesis in the hope of ultimately facilitating the development of novel strategies for treatment and prevention of this devastating disease.

2. Materials

2.1 Eukaryotic Cell Lines

Table 1: Name, origin and source of cell lines used in this work

Cell Line	Organism of origin	Tissue of origin	Source
HEK293-EBNA	*Homo sapiens*	Embryonic kidney	(Invitrogen) Thermo Fisher Scientific, Waltham, MA, USA
ARPE-19	*Homo sapiens*	Retinal pigment epithelium	ATCC; LGC Standards GmbH, Wesel, Germany
hiPSC-RPE	*Homo sapiens*	Dermal skin or peripheral blood	Institute of Human Genetics, University of Regensburg, Germany
HUVEC	*Homo sapiens*	Umbilical cord vein	Life Technologies, Carlsbad, CA, USA
Y-79	*Homo sapiens*	Retinoblastoma	ATCC; LGC Standards GmbH, Wesel, Germany
WERI-Rb1	*Homo sapiens*	Retinoblastoma	ATCC; LGC Standards GmbH, Wesel, Germany

2.2 Escherichia (E.) Coli Strains

E. coli strain DH5α from Life Technologies (Carlsbad, CA, USA) was used in this work.

2.3 Oligonucleotide Primers and Probes for PCR and Sequencing Reactions

Table 2: Name, sequences, target genes and application of oligonucleotides primers and probes used in this work

Primer name	Sequence (5'-3')	T_a [°C]	Target	Application
hGusB-RT-F	GTTGGAGAGCTCATTTGGA	60	*GUSB*	RNA expression analysis
hGusB-RT-R	CACGCAGGTGGTATCAGTCTT			
VTN_SeqInt2_F	AAGAACGGTTCCCTCTTTGC	61	*VTN*	Endogenous *VTN* expression analysis
VTN_SeqInt_R	AAGGCTGCATCCACGTTGTC			
hVTN_Ex7-R	GACACTCTGGATGGGTTCACAG	61		*VTN* amplification from genomic DNA and
VTN_SeqInt2_F	AAGAACGGTTCCCTCTTTGC			

				RNA
hVTN_Ex7-R	GACACTCTGGATGGGTTCACAG	55		rs704 genotyping by Sanger sequencing
RT_hSox2_F	ACACCAATCCCATCCACACT	62	SOX2	RNA expression analysis
RT_hSox2_R	GCAAACTTCCTGCAAAGCTC			
hOCT4_RT_Z_F	CGAGCAATTTGCCAAGCTCCTGAA	62	OCT4	RNA expression analysis
hOCT4-RT_Z_R	TCGGGCACTGCAGGAACAAATTC			
hRPE65-RT-F	CAATGGGTTTCTGATTGTGGA	60	RPE65	RNA expression analysis
Rpe65-R	GGGTGAGAAACAAAGATGGG			
hITGB8-RT-F	ATCCTGTGCCAGGTGCCTT	60	ITGB8	RNA expression analysis
hITGB8-RT-R	TGGACGCAGCTGGATAGACAC			
hBEST1-RT-F	CCTGCTGAACGAGATGAACA	60	BEST1	RNA expression analysis
hBEST1-RT-R	GGACACCTGCAAATTCCTGT			
hRLBP1-RT-F	ACAAGTATGGCCGAGTGGTC	60	RLBP1	RNA expression analysis
hRLBP1-RT-R	CCACATTGTAGGTCGTGGTG			
hTYR-RT-F	CCATGGATAAAGCTGCCAAT	60	TYR	RNA expression analysis
hTYR-RT-R	GCCCAGARCTTTGGATGAAA			
PAI-1-EcoRI-F	GAATTCATGCAGATGTCTCCAGCCCTCA	60	PAI-1 (Aka SERPINE1)	Expression cloning into pGEM®-T
PAI-1-XhoI-R	CTCGAGTCAGGGTTCCATCA			
PAI-1-EcoRI-F	GAATTCATGCAGATGTCTCCAGCCCTCA	60		Expression cloning into pEXPR-IBA103
PAI-1-XhoI_wostop-R	CTCGAGGGGTTCCATCACTTGGCCCAT			
PAI-1-seq1-F	ACAGACGCGATCTTGGTCCA	55		
PAI-1-seq2-F	TATACTGAGTTCACCACGCCCG			
M13_F	CGC CAG GGT TTT CCC AGT CAC GAC	55	pGEM®-T cloning vector (flanking cloning sites)	
M13_R	AGC GGA TAA CAA TTT CAC ACA GGA			
T7_F	TAA TAC GAC TCA CTA TAG GG	55	pCDNA3.1 expression vector (flanking cloning sites)	Sanger sequencing
BGH_R	TAG AAG GCA CAG TCG AGG			
pEXPR-IBA3-F	GAGAACCCACTGCTTACTGGC	55	pEXPR-IBA103 expression vector (flanking cloning sites)	
pEXPR-IBA3-R	TAGAAGGCACAGTCGAGG			
FH1_SERPINE1	GCTGCAGAAAGTGAAGATCG	60	PAI-1 (Aka SERPINE1)	qPCR expression analysis
RH1_SERPINE1	GTCCATGATGATCTCCTCGG			

PH1_SERPINE1 (Probe)	(6FAM)GTGGCCTCCTCATCCAAC AGCTGTC(OQA)			
FH1_HPRT1	CTTTGCTTTCCTTGGTCAGG			
RH1_HPRT1	TCAAATCCAACAAAGTCTGGC	60	*HPRT1*	
PH1_HPRT1 (Probe)	(6FAM)GCTTGCTGGTGAAAAGGA CCCCACG(OQA)			

qRT-PCR: quantitative real-time reverse transcription (RT)-PCR; T$_a$: annealing temperature

All oligonucleotides were purchased from Metabion (Planegg, Germany) except for those used for qRT-PCR which were purchased from Sigma-Aldrich (St. Louis, MO, USA).

2.4 Plasmids and Expression Constructs

Table 3: Name, application and source of plasmids and expression constructs used in this work

Plasmid name	Application	Source
pGEM®-T	Cloning vector	Promega Corporation, Madison, WI, USA
pCDNA3.1	Expression vector	Thermo Fisher Scientific, Waltham, MA, USA
pEXPR-IBA103	Expression vector	Iba Life Sciences, Götting, Germany
pCDNA3.1-GFP	Expression of recombinant GFP	Institute of Human Genetics, University of Regensburg, Germany
pcDNA3.1-VTN_rs704:C	Expression of recombinant VTN_rs704:C	Institute of Human Genetics, University of Regensburg, Germany
pcDNA3.1-VTN_rs704:T	Expression of recombinant VTN_rs704:T	Institute of Human Genetics, University of Regensburg, Germany
pEXPR-IBA103-VTN_rs704:C	Expression of recombinant Strep-tagged VTN_rs704:C	Institute of Human Genetics, University of Regensburg, Germany
pEXPR-IBA103-VTN_rs704:T	Expression of recombinant Strep-tagged VTN_rs704:T	Institute of Human Genetics, University of Regensburg, Germany
pcDNA3.1-PAI-1	Expression of recombinant PAI-1	Generated during this work
pEXPR-IBA103-PAI-1	Expression of recombinant Strep-tagged PAI-1	Generated during this work

2.5 Primary Antibodies

Table 4: Name, origin, application, and source of primary antibodies used in this work

Antibody	Class	Host species	Dilution	Application	Source
Anti-ACTB (A5441)	mAB	mouse	1:10000	WB	Sigma-Aldrich, St. Louis, MO, USA
Anti-ATP1A1 (55187-1-AP)	pAB	rabbit	1:100	IF	Proteintech Group, Rosemont, IL, USA
Anti-ATP1B1	pAB	rabbit	1:100	IF	Proteintech Group,

(15192-1-AP)					Rosemont, IL, USA
Anti-BEST1 (ab2182)	mAB	mouse	1:500	IF	Abcam, Cambridge, United Kingdom
Anti-C9 (ab17931)	mAB	mouse	1:100	IF	Abcam, Cambridge, United Kingdom
Anti-CFH (ab121056)	mAB	mouse	1:100	IF	Abcam, Cambridge, United Kingdom
Anti-COL V (ab6582)	pAB	rabbit	1:100	IF	Abcam, Cambridge, United Kingdom
Anti-COL VI (SD83-03)	mAB	rabbit	1:100	IF	ThermoFisher Scientific, Waltham, MA, USA
Anti-ELA (324756)	pAB	rabbit	1:100	IF	(Calbiochem) Merck KGaA, Darmstadt, Germany
Anti-FN (F7387)	mAB	mouse	1:100	IF	Sigma-Aldrich, St. Louis, MO, USA
Anti-GFP (sc-8334)	pAB	rabbit	1:10000	WB	Santa Cruz Biotechnology, Dallas, TX, USA
Anti-LAM (ab11575)	pAB	rabbit	1:100	IF	BIOZOL Diagnostica Vertrieb GmbH, Eching, Germany
Anti-LC3B (D11) XP® (3868S)	mAB	rabbit	1:1000 in BSA	WB	Cell Signaling Technology, Danvers, MA, USA
Anti-MAP Kinase (ERK1/2) (M5670)	pAB	rabbit	1:2000 in BSA	WB	Sigma-Aldrich, St. Louis, MO, USA
Anti-PAI-1 (11907S)	mAB	rabbit	1:1000 1:100	WB IF	Cell Signaling Technology, Danvers, MA, USA
Anti-TIMP3 (MAB3318)	mAB	mouse	1:100	IF	Sigma-Aldrich, St. Louis, MO, USA
Anti-VEGF (P802)	pAB	rabbit	1:100	IF	Thermo Fisher Scientific, Waltham, MA, USA
Anti-VTN (MAB2349)	mAB	mouse	1:5000 1:250	WB IF	R&D Systems, Inc., Minneapolis, MN, USA
Anti-ZO1 (61-7300)	pAB	rabbit	1:500	IF	(Invitrogen) ThermoFisher Scientific, Waltham, MA, USA
Phospho-p44/42 MAPK (ERK1/2) (Thr202/Tyr204) (D13.14.4E) XP® Rabbit (4370S)	mAB	rabbit	1:2000 in BSA	WB	Cell Signaling Technology, Danvers, MA, USA

WB: Western Blot; IF: Immunofluorescence staining; mAB: monoclonal antibody. pAB: polyclonal antibody
Indicated in brackets are manufacturer's product catalogue numbers where available.

Unless labelled "in BSA" (antibodies prepared in BSA-based solution) (see Table 11), all antibodies used in the western blot analysis were prepared in a milk-based antibody solution (see Table 11).

2.6 Secondary Antibodies

Table 5: Name, origin, application, and source of secondary antibodies used in this work

Antibody	Dilution	Application	Source
Goat anti-mouse IgG, peroxidase-conjugate	1:10000	WB	(Calbiochem) Merck KGaA, Darmstadt, Germany
Goat anti-rabbit IgG, peroxidase-conjugate	1:10000	WB	(Calbiochem) Merck KGaA, Darmstadt, Germany
Goat anti-mouse IgG, Alexa Fluor®594	1:800	IF	Life Technologies, Carlsbad, CA, USA
Goat anti-mouse IgG, Alexa Fluor®488	1:800	IF	Life Technologies, Carlsbad, CA, USA
Goat anti-rabbit IgG, Alexa Fluor®594	1:800	IF	Life Technologies, Carlsbad, CA, USA
Goat anti-rabbit IgG, Alexa Fluor®488	1:800	IF	Life Technologies, Carlsbad, CA, USA

WB: Western Blot; IF: Immunofluorescence staining

2.7 Enzymes

Table 6: Name and source of enzymes used in this work

Enzyme	Source
Antarctic phosphatase	New England Biolabs, Ipswich, MA, USA
EcoRI-HF (restriction enzyme)	New England Biolabs, Ipswich, MA, USA
GoTaq® DNA-Polymerase	Promega Corporation, Madison, WI, USA
Papain	Sigma-Aldrich, St. Louis, MO, USA
RevertAid M-MuLV Reverse Transcriptase	(Fermentas) Thermo Fisher Scientific, Waltham, MA, USA
T4 DNA Ligase	New England Biolabs, Ipswich, MA, USA
TrypLE™ Select Enzyme, no phenol red	Life Technologies, Carlsbad, CA, USA
Trypsin, TPCK-Treated	Thermo Fisher Scientific, Waltham, MA, USA
Trypsin-EDTA (0.5%), no phenol red	Life Technologies, Carlsbad, CA, USA
XhoI (restriction enzyme)	New England Biolabs, Ipswich, MA, USA

2.8 Molecular Weight Standards

Table 7: Molecular weight standards and their source used in this work

Molecular Weight Standard	Source
Color-coded Prestained Protein Marker, High Range (43-315 kDa)	Cell Signaling Technologies, Danvers, MA, USA
Gene Ruler DNA Ladder Mix	Thermo Fisher Scientific, Waltham, MA, USA
NativeMark™ Unstained Protein Standard	(Invitrogen) ThermoFisher Scientific, Waltham, MA, USA
PageRuler™ Prestained Protein Ladder, 10 to 180 kDa	Thermo Fisher Scientific, Waltham, MA, USA

2.9 Kit Systems

Table 8: Name and source of molecular biological kits used in this work

Kit system	Source
BigDye Terminator v1.1, v3.1 Cycle Sequencing Kit	Thermo Fisher Scientific, Waltham, MA, USA
CHEMICON PAI Activity Assay Kit	(Merck) Sigma-Aldrich, St. Louis, MO, USA
Clarity Max™ Western Blotting Substrate	Bio-Rad Laboratories GmbH, Munich, Germany
Clarity ™ Western Blotting Substrate	Bio-Rad Laboratories GmbH, Munich, Germany
KiCqStart® Probe Assays	(Merck) Sigma-Aldrich, St. Louis, MO, USA
Lipofectamine™ 3000 Transfection Reagent	Thermo Fisher Scientific, Waltham, MA, USA
Mirus TransIT®-LTI Transfection Reagent	Mirus Bio LLC, Madison, WI, USA
NucleoBond® Xtra	MACHEREY-NAGEL GmbH & Co. KG, Düren, Germany
NucleoSpin® Gel and PCR Clean-up	MACHEREY-NAGEL GmbH & Co. KG, Düren, Germany
NucleoSpin® Plasmid	MACHEREY-NAGEL GmbH & Co. KG, Düren, Germany
NucleoSpin® Tissue	MACHEREY-NAGEL GmbH & Co. KG, Düren, Germany
PureLink™ RNA Micro Kit	(Invitrogen) Thermo Fisher Scientific, Waltham, MA, USA
RNase-Free DNase Set	Qiagen, Hilden, Germany
Strep-tag® protein purification system	Iba Life Sciences, Götting, Germany
Takyon™ Low Rox Probe MasterMix dTTP Blue	Eurogentec, Seraing, Liège, Belgium

2.10 Chemicals

Table 9: Name and source of chemicals used in this work

Chemical	Source
4-(2-hydroxyethyl)-1-	Merck KGaA, Darmstadt, Germany

piperazineethanesulfonic acid, $C_8H_{18}N_2O_4S$ (HEPES)	
3-(4,5-dimethylthiazol-2-yl)-2,5-diphenyl tetrazolium bromide (MTT)	Sigma-Aldrich, St. Louis, MO, USA
4′,6-diamidino-2-phenylindole (DAPI)-Stain-solution	Life Technologies GmbH, Darmstadt, Germany
5-Bromo-4-chloro-3-indolyl β-D-galactopyranoside, $C_{14}H_{15}BrClNO_6$ (X-Gal)	AppliChem GmbH, Darmstadt, Germany
Acidic acid, CH_3COOH	Merck KGaA, Darmstadt, Germany
Ammonia solution 25%, NH_4OH	Merck KGaA, Darmstadt, Germany
Ammonium persulfate (APS), $(NH_4)_2S_2O_8$	AppliChem GmbH, Darmstadt, Germany
Ampicillin sodium salt, $C_{16}H_{18}N_3NaO_4S$	Carl Roth GmbH + Co. KG, Karlsruhe, Germany
bisBenzimide Hoechst (H) 33342 trihydrochloride, $C_{27}H_{28}N_6O\cdot3HClx\cdot H_2O$	Sigma-Aldrich, St. Louis, MO, USA
Bromophenol blue sodium salt, $C_{19}H_9Br_4O_5SNa$	Sigma-Aldrich, St. Louis, MO, USA
Calcium chloride, $CaCl_2$, 2M	Carl Roth GmbH + Co. KG, Karlsruhe, Germany
Chloroquine, $C_{18}H_{26}ClN_3$	Merck KGaA, Darmstadt, Germany
Coomassie Brilliant Blue R-250 (sodium salt), $C_{45}H_{44}N_3NaO_7S_2$	VWR International Germany GmbH, Darmstadt, Germany
Dimethyl sulfoxide (DMSO), C_2H_6OS	AppliChem GmbH, Darmstadt, Germany
Disodium hydrogen phosphate, Na_2HPO_4	Merck KGaA, Darmstadt, Germany
Dithiothreitol (DTT)	Carl Roth GmbH + Co. KG, Karlsruhe, Germany
Ethanol ≥99,8, C_2H_6O	Carl Roth GmbH + Co. KG, Karlsruhe, Germany
Ethidium bromide-solution 0,07%, $C_{21}H_{20}BrN_3$ in H_2O	AppliChem GmbH, Darmstadt, Germany
Ethylendiamintetraacetat disodium dihydrate salt, $C_{10}H_{14}N_2Na_2O_8\cdot2H_2O$ (EDTA)	Merck KGaA, Darmstadt, Germany
Glucose, $C_6H_{12}O_6$	Merck KGaA, Darmstadt, Germany
Glutaraldehyde 25%, $C_5H_8O_2$ in H_2O	Carl Roth GmbH + Co. KG, Karlsruhe, Germany
Glycerol 87%, $C_3H_8O_3$	University of Regensburg, Chemical Supplies
Glycin, $C_2H_5NO_2$	AppliChem GmbH, Darmstadt, Germany
HiDi™ Formamide, CH_3NO	Thermo Fisher Scientific, Waltham, MA, USA
Hydrochloric acid 1M, HCl	Merck KGaA, Darmstadt, Germany
Hydrogen peroxide (H_2O_2) 30%	Sigma-Aldrich, St. Louis, MO, USA
Isopropanol, C_3H_8O	Merck KGaA, Darmstadt, Germany
Isopropyl β-d-1-thiogalactopyranoside, $C_9H_{18}O_5S$ (IPTG)	AppliChem GmbH, Darmstadt, Germany
L-Cysteine	Sigma-Aldrich, St. Louis, MO, USA
Magnesium chloride, $MgCl_2$	Merck KGaA, Darmstadt, Germany
Methanol, CH_4O	Sigma-Aldrich, St. Louis, MO, USA
Paraformaldehyde (PFA), $(CH_2O)_n$	AppliChem GmbH, Darmstadt, Germany
Peptone	Carl Roth GmbH + Co. KG, Karlsruhe, Germany
Potassium chloride, KCl	Merck KGaA, Darmstadt, Germany
Potassium dihydrogen phosphate, KH_2PO_4	Merck KGaA, Darmstadt, Germany
Sodium acetate trihydrate, $CH_3COONa\cdot H2O$	Merck KGaA, Darmstadt, Germany
Sodium chloride, NaCl	VWR International Germany GmbH, Darmstadt, Germany
Sodium dodecyl sulphate (SDS) ≥99%, $C_{12}H_{25}NaO_4S$	Carl Roth GmbH + Co. KG, Karlsruhe, Germany
Sodium hydroxide, NaOH	Merck KGaA, Darmstadt, Germany
Tetramethylethylenediamine (TEMED), $(CH_3)_2NCH_2CH_2N(CH_3)_2$	Merck KGaA, Darmstadt, Germany
Tris(hydroxymethyl)aminomethane (Tris), $NH_2C(CH_2OH)_3$	Affymetrix, Santa Clara, CA, USA
Tris-HCl	VWR International Germany GmbH, Darmstadt, Germany

β-Mercaptoethanol, $HSCH_2CH_2OH$	Sigma-Aldrich, St. Louis, MO, USA

2.11 Readymade Solutions/Buffers

Table 10: Name and source of readymade solutions/buffers used in this work

Solution/buffer	Source
2x Rapid Ligation buffer	Promega Corporation, Madison, WI, USA
5x Reaction buffer for RevertAid™ Reverse Transcriptase	(Fermentas) Thermo Fisher Scientific, Waltham, MA, USA
Agarose (Biozym LE)	Biozym Scientific GmbH, Hessisch Oldendorf, Germany
Antarctic phosphatase buffer	New England Biolabs, Ipswich, MA, USA
Bacto Agar	BD Bioscience, Heidelberg, Germany
Bacto yeast extract	BD Bioscience, Heidelberg, Germany
Bovine serum albumin (BSA)	AppliChem GmbH, Darmstadt, Germany
CutSmart®buffer	New England Biolabs, Ipswich, MA, USA
Dako Fluorescent Mounting Medium	Agilent, Santa Clara, CA, USA
Dulbecco's phosphate-buffered saline (DPBS)	Sigma-Aldrich, St. Louis, MO, USA
Goat serum	Abcam, Cambridge, United Kingdom
NativePAGE™ 5% G-250 Sample Additive	(Invitrogen) ThermoFisher Scientific, Waltham, MA, USA
NativePAGE™ Cathode buffer Additive (20X)	(Invitrogen) ThermoFisher Scientific, Waltham, MA, USA
NativePAGE™ Running buffer (20x)	(Invitrogen) ThermoFisher Scientific, Waltham, MA, USA
NativePAGE™ Sample buffer (4x)	(Invitrogen) ThermoFisher Scientific, Waltham, MA, USA
NuPAGE™ Transfer buffer (20x)	(Invitrogen) ThermoFisher Scientific, Waltham, MA, USA
Random Hexamer Primers	Thermo Fisher Scientific, Waltham, MA, USA
Roti®-Quant reagent	Carl Roth GmbH + Co. KG, Karlsruhe, Germany
Rotiphorese Gel 40% Acrylamide/ Bisacrylamide	Carl Roth GmbH + Co. KG, Karlsruhe, Germany
Skimmed milk powder	Carl Roth GmbH + Co. KG, Karlsruhe, Germany
Strep-Tactin ®elution buffer (buffer E)	Iba Life Sciences, Götting, Germany
Strep-Tactin ®regeneration buffer (buffer R)	Iba Life Sciences, Götting, Germany
Strep-Tactin ®wash buffer (buffer W)	Iba Life Sciences, Götting, Germany
T4 DNA Ligase buffer	New England Biolabs, Ipswich, MA, USA
Triton® X-100	AppliChem GmbH, Darmstadt, Germany
Tween® 20	VWR International Germany GmbH, Darmstadt, Germany
Vitronectin Protein, Human, Recombinant (His-Tag)	Sino Biological, Inc., Beijing, China

2.12 Solutions and Buffers

Table 11: Composition of solution and buffers prepared in this work

Buffer/Solutions	Composition	Amounts
2x HBS	NaCl KCl Na$_2$HPO$_4$ HEPES dH$_2$O	280 mM 10 mM 1.5 mM 50 mM
5x DNA-Gel Loading buffer	Bromophenol Blue Glycerol 87% dH$_2$O	0.01% (w/v) 40% (v/v)
5x Laemmli-buffer	Bromophenol Blue Tris-HCl pH 6.8 β-Mercaptoethanol SDS Glycerol dH$_2$O	0,01% v/v 60 mM 5% (w/v) 2% (w/v) 10% (v/v)
Agarose gel solution	Agarose TBE pH 8.0	0.8 – 1.5% (w/v)
Antibody solution for IF	Goat serum TritonX-100 DPBS	2.5% (v/v) 0.1% (v/v)
Antibody solution for WB	1x TBS-T Skimmed Milk Powder or BSA	5% (w/v)
Blocking solution for IF	Goat serum TritonX-100 DPBS	10% (v/v) 0.3% (v/v)
Blocking Solution for WB	Skimmed Milk Powder 1x TBS-T	5% (w/v)
Coomassie destaining solution	Methanol Acidic acid 100% Coomassie Brilliant Blue dH$_2$O	30% (v/v) 10% (v/v) 0,1% (w/v)
Coomassie staining solution	Methanol Acidic acid 100% dH$_2$O	30% (v/v) 10% (v/v)
Decellularization buffer	TritonX-100 NH$_4$OH DPBS	0.5 % (v/v) 20 mM
Dissociation buffer	L-Cysteine Papain BSA PBS-EDTA	260 mM 0.15% (v/v) 1.2% (v/v)
IPTG Solution	IPTG dH$_2$O	0,1 M
LB-Agar	Peptone Bacto-yeast extract NaCl Bacto-Agar dH$_2$O	1% (w/v) 0.5% (w/v) 1% (w/v) 15% (w/v)
Lysogeny Broth (LB)-Medium	Peptone Bacto-yeast extract NaCl	1% (w/v) 0.5% (w/v) 1% (w/v)

	dH$_2$O	
MTT Solution	MTT 1x PBS	0.5 % (w/v)
PB, pH 7.2	Na$_2$HPO$_4$ NaH$_2$PO$_4$ dH$_2$O	78 mM 26 mM
PBS, pH 7.4	NaCl KCl Na$_2$HPO$_4$ KH$_2$PO$_4$ dH$_2$O	137 mM 0.27 mM 10 mM 1.8 mM
PBS-EDTA	EDTA DPBS	0.2% (v/v)
PFA Solution	PFA PBS	2% (w/v)
SDS Running buffer, pH 8.6	Tris-HCl Glycine SDS dH$_2$O	0.25 mM 0.2 M 1% (w/v)
SOC medium	Trypton Yeast extract NaCl KCl MgCl2 Glucose	2% (w/v) 0.5% (w/v) 10 mM 2.5 mM 10 mM 20 mM
TBE, pH 8.0	Tris Boric acid EDTA dH$_2$O	100 mM 100 mM 1 mM
TBS, pH 7.5	Tris NaCl dH$_2$O	50 mM 150 mM
TBS-T	Tween® 20 TBS	0,1% (v/v)
Towbin transfer buffer	Glycine Tris Methanol dH$_2$O	190 mM 0.25 mM 20% (v/v)
Tris-buffered saline w	Tris-HCl [pH 8] NaCl	150 mM 100 mM
TritonX-100-Solution	TritonX-100 dH$_2$O	1.5% (v/v)
X-Gal Solution	X-Gal Dimethylformamide	0.04% (w/v)

dH$_2$O: distilled water

2.13 Cell Culture Mediums and Supplements

Table 12: Type and source of cell culture media and supplements used in this work

Medium/supplement	Source
Ascorbic acid, C$_6$H$_8$O$_6$ (30 µg/ml)	Cayman Chemical, Ann Arbor, MI, USA
Corning® Matrigel® Growth Factor Reduced (GFR) Basement Membrane Matrix, LDEV-Free	Corning, NY, USA

Dextran sulphate sodium salt (200 µg/ml)	Carl Roth GmbH + Co. KG, Karlsruhe, Germany
DMEM/Nutrient Mixture F-12 Ham medium (DMEM/F12)	Sigma-Aldrich, St. Louis, MO, USA
Dulbecco's modified eagle medium (DMEM) high-glucose medium (4.5 g/l)	Thermo Fisher Scientific, Waltham, MA, USA
Dulbecco's phosphate-buffered saline (DPBS)	Sigma-Aldrich, St. Louis, MO, USA
EGMPlus Endothelial Cell Growth Media	Lonza Group, Ltd., Basel, Switzerland
EGM-Plus SingleQuot Kit: Fetal Bovine Serum (FBS), Hydrocortisone, bovine brain extract (BBE), L-Glutamine, Heparin, Ascorbic acid, recombinant human epidermal growth factor (rhEGF)	Lonza Group, Ltd., Basel, Switzerland
Fetal Calf Serum (FCS)	Life Technologies, Carlsbad, CA, USA
Geltrex Growth Factor Reduced Basement Membrane Matrix, LDEV-Free	Thermo Fisher Scientific, Waltham, MA, USA
Geneticin™ Selective Antibiotic (G418 sulphate), $C_{20}H_4ON_4O_{10} \cdot H_2SO_4$	Thermo Fisher Scientific, Waltham, MA, USA
Gentamicin (5 mg/ml)/Amphotericin (125 µg/ml)	Thermo Fisher Scientific, Waltham, MA, USA
Gentamycin (5 µg/ml)	Sigma-Aldrich, St. Louis, MO, USA
Insulin (27 USP-units/mg)	Thermo Fisher Scientific, Waltham, MA, USA
KnockOut DMEM Medium	(Gibco) Life Technologies, Carlsbad, CA, USA
KnockOut Serum Replacement (5% v/v)	(Gibco) Life Technologies, Carlsbad, CA, USA
L-Glutamine (200 mM)	Thermo Fisher Scientific, Waltham, MA, USA
Nicotinamide (10 mM)	Sigma-Aldrich, St. Louis, MO, USA
Non-essential amino acids solution (0.1 mM)	(Gibco) Life Technologies, Carlsbad, CA, USA
OptiMEM™ medium	Thermo Fisher Scientific, Waltham, MA, USA
Penicillin (10.000 Units/ml) / streptomycin (10 mg/ml)	Thermo Fisher Scientific, Waltham, MA, USA
Poly-L-Lysine Hydrobromide (0.1 mg/ml)	Sigma-Aldrich, St. Louis, MO, USA
RPMI medium	Thermo Fisher Scientific, Waltham, MA, USA
VEGF (50 ng/ml)	PeproTech, Hamburg, Germany
β-Mercaptoethanol (0.1 mM)	Sigma-Aldrich, St. Louis, MO, USA

2.14 Consumables

Table 13: Consumables and their commercial sources used in this work

Consumables	Source
0.2 ml Strep-Tactin Sepharose columns	Iba Life Sciences, Götting, Germany
1 ml Strep-Tactin Sepharose columns	Iba Life Sciences, Götting, Germany
12-well/ 24-well ThinCert® Cell Culture Inserts (Transwell filters), 0.4-µm pore size	Greiner Bio-One International, Kremsmünster, Austria
5 ml Strep-Tactin Sepharose column	Iba Life Sciences, Götting, Germany
6/12/24-well cell culture plates	Greiner Bio-One GmbH, Frickenhausen, Germany
Cell culture dishes 10 cm	Sarstedt AG & Co., Nümbrecht, Germany

Cell culture flasks T25	Sarstedt AG & Co., Nümbrecht, Germany
Cell scrapers (blade width 14 mm)	TPP Techno Plastic Products AG, Trasadingen, Switzerland
Cuvettes	Sarstedt AG & Co., Nümbrecht, Germany
Eppendorf tubes 0.5/1.5/2.0 ml	Sarstedt AG & Co., Nümbrecht, Germany
Falcon tubes 15/50 ml	Sarstedt AG & Co., Nümbrecht, Germany
Flat bottom 96-well assay plates	Greiner Bio-One GmbH, Frickenhausen, Germany
Mini cell scrapers (blade width 5 mm)	VWR International Germany GmbH, Darmstadt, Germany
NativePAGE™ 4-16% Bis-Tris Protein Gels, 1.0 mm, 10-well	Invitrogen, Thermo Fisher Scientific, Waltham, MA, USA
PCR cups	Biozym Scientific GmbH, Hessisch Oldendorf, Germany
Petri dishes 10 cm	Sarstedt AG & Co., Nümbrecht, Germany
Pipette tips 10/100/1000 µl	VWR International Germany GmbH, Darmstadt, Germany
Plastic pipettes 5/10/20 ml	Sarstedt AG & Co., Nümbrecht, Germany
Polyvinylidene difluoride (PVDF) membranes	Merck KGaA, Darmstadt, Germany
QIAshredder, disposable cell-lysate homogenizers	Qiagen, Hilden, Germany
Sterile filter pipette tips 10/100/1000 µl	Greiner Bio-One International, Kremsmünster, Austria
Whatman paper 3 mm	Carl Roth GmbH + Co. KG, Karlsruhe, Germany

2.15 Devices/Tools

Table 14: Name and source of devices/tools used in this work

Device/tool	Source
96-Well Wound maker	Essen BioScience, Ann Arbor, MI, USA
Accu-jet Pipette Controller	Brand, Wertheim, Germany
Autoclave "Autoklav V-150"	Systec GmbH, Wettenberg, Germany
BlueMarine™ 200 Horizontal Submarine Electrophoresis Unit	SERVA Electrophoresis GmbH, Heidelberg, Germany
Bunsen burner Gasprofi1	WLD Tec, Göttingen, Germany
CASY TT Cell Counter	Innovatis Roche AG, Bielefeld, Germany
Dark Hood DH-40	Biostep GmbH, Burkhardtsdorf, Germany
Duomax 1030 Rocking Platform Shaker	Heidolph Instruments GmbH & Co.KG, Schwabach, Germany
Epithelial Volt/Ohm Meter	World Precision Instruments GmbH, Berlin, Germany
Eppendorf 5415R (refrigerated centrifuge for Eppendorf cups)	Eppendorf AG, Hamburg, Germany
Fine scales "Feinwaage Explorer"	OHAUS, Nänikon, Switzerland
Ice Machine AF 100	Scotsman, VerNicht Hills, IL, USA
Incubator for bacteria 37°C	Memmert GmbH, Schwabach, Germany
Incubator Hera Cell 150	Thermo Fisher Scientific, Waltham, MA, USA
Incubator Hood TH 15 combined with the Bühler Compact Shaker KS 15	Edmund Bühler GmbH, Bodelshausen, Germany
Leica microscope Type 090-136.001	Leica Microsystems GmbH, Wetzlar, Germany
LI-COR Odyssey Imaging System	LI-COR Biosciences, Lincoln, NE, USA

Megafuge 1.0R (refrigerated centrifuge for Falcon tubes)	Heraeus Holding GmbH, Hanau, Germany
Microwave KOR-6D07	Daewoo, Seoul, Korea
Milli-Q-Synthesis Water Purification System	Merck KGaA, Darmstadt, Germany
Mini Trans-Blot® Cell	Bio-Rad Laboratories GmbH, Munich, Germany
Mini-PROTEAN Tetra Vertical Electrophoresis Cell	Bio-Rad Laboratories GmbH, Munich, Germany
Multifuge 3L-R (centrifuge for Falcon tubes)	Heraeus Holding GmbH, Hanau, Germany
NanoDrop® ND1000 spectrophotometer	NanoDrop, Wilmington, DE, USA
Nikon Eclipse microscope	TE-2000-U; Nikon, Tokyo, Japan
Odyssey FC Imager	LI-COR Biosciences, Lincoln, NE, USA
Olympus FV3000 confocal laser scanning microscope	Olympus Europa SE & Co. KG, Hamburg, Germany
pH Meter Lab 850	SI Analytics GmbH, Mainz, Germany
Power Pack Blue Power 500	SERVA Electrophoresis GmbH, Heidelberg, Germany
Power Pack Blue Power Plus	SERVA Electrophoresis GmbH, Heidelberg, Germany
QuantStudio™ 5 Real-Time PCR System	Thermo Fisher Scientific, Waltham, MA, USA
RM5 Roller	(Assistent®) Glaswarenfabrik Karl Hecht GmbH & Co KG, Sondheim/Rhön, Germany
Scales	SCALTEC Instruments GmbH, Heiligenstadt, Germany
Short Plates Mini PROTEAN®	Bio-Rad Laboratories GmbH, Munich, Germany
Sigma 2-5 (centrifuge for Falcon tubes)	Sigma-Aldrich, St. Louis, MO, USA
Spacer Plates Mini PROTEAN® 0.75 mm	Bio-Rad Laboratories GmbH, Munich, Germany
Spacer Plates Mini PROTEAN® 1.5 mm	Bio-Rad Laboratories GmbH, Munich, Germany
Spark multimode microplate reader	Tecan Group AG, Männedorf, Switzerland
Sterile Workbench Heraguard	Heraeus Holding GmbH, Hanau, Germany
Thermocycler Peqstar 2x gradient	VWR International Germany GmbH, Darmstadt, Germany
Thermomixer compact	Eppendorf AG, Hamburg, Germany
Trans-Blot® Turbo™ Transfer System	Bio-Rad Laboratories GmbH, München, Germany
Transfer pipette 10/100/1000 µl	Brand, Wertheim, Germany
Transilluminator UST-30_M-8R	BioView Ltd., Billerica, MA, USA
Ultrospec 2100 pro UV/Visible spectrophotometer	(Amersham Biosciences) GE Healthcare, Chicago, Illinois, USA
UVP GelStudio PLUS, 230V	Analytik Jena GmbH, Jena, Germany
Vibra Cell VCX400 Ultrasound device	Sonics & Materials, Newtown, CT, USA
Vortex Genie2	Scientific Industries, Bohemia, NY, USA
Waterbath W12	Labortechnik Medingen, Arnsdorf, Germany

2.16 Software

Table 15: Name and source of software used in this work

Software	Source
ApE-A Plasmid Editor	M.Wayne Davis, Department of Biology, University of Utah, Salt Lake City, UT, USA
CorelDRAW Graphic Suite 2021	Corel Corporation, Ottawa, Ontario, Kanada
FV3000 software	Olympus Europa SE & Co. KG, Hamburg, Germany
Image Studio	LI-COR Biosciences GmbH, Lincoln, NE, USA
ImageJ	Wayne Rasband, National Institutes of Health, USA
Microsoft Office	Microsoft Cooperation, Redmond, WA, USA
SnapGene	GSL Biotech LLC, Chicago, IL, USA
XLSTAT	Addinsoft Inc., NY, USA
ArgusX1 V4.0.81	Biostep GmbH, Burkhardtsdorf, Germany

3. Methods

3.1 Genomic DNA Isolation and Purification

Total genomic DNA was isolated from cultured cells using the NucleoSpin® Tissue Kit, according to the manufacturer's protocol. Genomic DNA was eluted in 50 µl of Milli-Q H_2O and the concentration was measured using the NanoDrop® ND1000 Spectrophotometer. Purified genomic DNA was kept at -20°C until further use.

3.2 RNA Isolation and Purification

Total RNA was isolated from cultured cells using the PureLink RNA Micro Kit (Invitrogen), according to the manufacturer's protocol with slight modifications: Wash Buffer I provided by PureLink RNA Micro kit was pre-incubated with RNase-Free DNase set (Qiagen) for 15 min at room temperature (RT) before use according to the manufacturer's protocol. QIAshredder cell-lysate homogeniser (Qiagen) were used in the cell lysing step. RNA was eluted in RNase-free H_2O and the concentration was measured using the NanoDrop® ND1000 Spectrophotometer. Purified RNA was kept at -80°C until further use.

3.3 cDNA Synthesis by Reverse Transcription of Total RNA

One microgram of purified RNA was mixed with 1 µl of Random Hexamer primers and the final reaction volume was adjusted to 12.5 µl using RNase-free H_2O. After an initial five-min incubation step at 65°C (Annealing, Table 16), the mixture was placed on ice and 7.5 µl of reaction mix containing reverse transcriptase was added (see Table 17). The reaction was completed in the thermocycler according to the program shown in Table 16.

Table 16: Thermocycler program used for cDNA synthesis

Reaction Step	Temperature	Duration
Annealing	65°C	5 min
cDNA synthesis and heat-inactivation	25°C	10 min
	42°C	60 min
	70°C	10 min

Table 17: Reaction mixture for synthesis of cDNA

Component	Volume
RNase-free H_2O	0.5 µl
5x Reaction buffer for RevertAid™ Reverse Transcriptase	4 µl
dNTPs (1.25 mM)	2 µl
RevertAid™ Reverse Transcriptase	1 µl

3.4 Targeted DNA Amplification by Polymerase Chain Reaction (PCR)

The DNA regions of interest were PCR amplified from cDNA, plasmid or genomic DNA using GoTaq® DNA-Polymerase. PCR reaction mixture and thermocycler program are indicated in Table 18 and Table 19. Annealing temperature and elongation time (1 min/1000 bp) were optimised according to the DNA sequence to be amplified and the primers used (see Table 2 for primer specification).

Table 18: Reaction mixture for PCR

Component	Volume
5x Green GoTaq® Reaction buffer	5 µl
Primer Forward (10 µM)	1 µl
Primer Reverse (10 µM)	1 µl
dNTPs (1.25 mM)	1 µl
DNA (25 µg/µl)	2 µl
GoTaq® DNA-Polymerase	0.25 µl
Milli-Q $H_2$0	14.75 µl

Table 19: Thermocycler program used for PCR

Reaction Step	Temperature	Duration	Cycles
Initial denaturation	95°C	3 min	
Denaturation	94°C	30 sec	
Annealing	X°C	30 sec	30
Elongation	72°C	X min	
Final Elongation	72°C	5 min	
Pause	4°C	-	

3.5 Agarose Gel Electrophoresis

PCR products were mixed with 5x DNA-Gel Loading buffer and separated by electrophoresis on 1-2% agarose gel (1% for fragments lager than 1000 bp, 1.5% for fragments between 1000 and 500 bp, 2% for fragments smaller than 1000 bp). The agarose was dissolved in TBE buffer by microwave heating. After cooling the solution to > 45°C, two drops of 0.07% ethidium bromide solution were added and the gels were poured. Electrophoretic separation was performed at 190 V for about 30 min. Amplification products were visualized with an UV transilluminator placed in a dark hood DH-40 (Biostep GmbH, Jahnsdorf, Germany). Gel runs were documented with the software ArgusX1 V4.0.81. For gel purification, DNA fragments of the correct size were excised from the gel (see section 3.6). The GeneRuler™ DNA Ladder Mix served as a size standard.

3.6 Purification of PCR Products

PCR products were excised from agarose gels and purified using the NucleoSpin® Gel and PCR Clean-up kit according to the manufacturer's instructions. DNA was eluted in 25 µl of Milli-Q H_2O and stored at -20°C until further use. DNA concentrations were determined using a NanoDrop® ND1000 Spectrophotometer.

3.7 Sanger Sequencing

DNA sequencing was performed using the BigDye® Terminator v1.1, v3.1 Cycle Sequencing Kit. The required reaction mixture components and the thermal cycler program used are depicted in Table 20 and Table 21.

Table 20: Reaction mixture for Sanger sequencing

Component	Volume
BigDye® Terminator Reaction Mix	0.8 µl
5x BigDye® Terminator Sequencing buffer	2 µl
Primer (10 µM)	1 µl
DNA (25 µg/µl)	2 µl
Milli-Q H$_2$0	4.2 µl

Table 21: Thermocycler program for Sanger sequencing

Reaction Step	Temperature	Duration	Cycles
Initial denaturation	94°C	3 min	
Denaturation	94°C	30 sec	
Annealing	55°C	30 sec	27
Elongation	60°C	3 min	
Final Elongation	60°C	5 min	
Pause	4°C	-	

Precipitation of the Sanger sequencing products was conducted by adding 2 µl of 3 M sodium acetate and 25 µl of 100% ethanol to each sample, which was then vortexed and centrifuged (30 min, 4000 rpm, 4°C; Centrifuge Megafuge 1.0R). The supernatant was discarded, and the pellet was washed in 100 µl of 70% ethanol followed by a second centrifugation step (20 min, 4000 rpm, 4°C; Centrifuge Megafuge 1.0R). After removal of the supernatant, the pellet was resuspended in 15 µl of HiDi™ formamide, transferred to a 96-well plate for analysis and subjected to analysis using the Abi3130x1 genetic analyser. ApE-A Plasmid Editor software was used to visualize and investigate the sequences obtained.

3.8 Quantitative Real-time PCR

The quantitative real-time PCR (qPCR) reaction was conducted with the Takyon™ Low Rox Probe MasterMix dTTP blue and the KiCqStart® Probe Assay (primers and probes used are given in Table 2), using cDNA as a template. Each reaction was performed in technical triplicates utilizing the QuantStudio™ 5 Real-Time PCR System. Details on reaction composition and PCR conditions are shown in Table 22 and Table 23. Data analysis implied the ΔΔCt method for relative quantification [245].

Table 22: Reaction mixture for qPCR

Component	Volume
Takyon™ Low Rox Probe MasterMix dTTP blue	5 µl
Primer Forward (50 µM)	1 µl
Primer Reverse (50 µM)	1 µl
KiCqStart®Probe	0.125 µl
cDNA (20 ng/µl)	2.5 µl
Milli-Q H_2O	0.375 µl

Table 23: QuantStudio5 PCR program for qPCR

Reaction Step	Temperature	Duration	Cycles
Polymerase activation	95°C	10 min	
Denaturation	95°C	15 sec	40
Annealing plus elongation	60°C	1 min	

3.9 Generation of Expression Vectors Encoding for PAI-1

The full-length coding sequence for PAI-1 (NM_000602.4) was PCR amplified with oligonucleotides primer pairs PAI-1-EcoRI-F and PAI-1-XhoI-R and cDNA obtained by reverse transcription from ARPE-19 total RNA (see sections 3.2 and 3.3). The primers PAI-1-EcoRI-F and PAI-1-XhoI_wostop-R were utilized for the amplification of the PAI-1 coding sequence without stop codon for insertion into the PEXPR-IBA103 vector allowing the expression of Strep-tagged PAI-1 (primer sequences given in Table 2). After electrophoresis on a 1% agarose gel, the amplified fragments were extracted from the gel and after purification (see section 3.6) were ligated into a cloning vector.

3.9.1 Ligation into pGEM®-T Vector

Amplified coding sequences for PAI-1 were ligated into the pGEM®-T vector using the ligation mixture shown in Table 24 (vector, ligase and buffer all included in the pGEM®-T vector kit). The ligation mixtures were incubated overnight at 4°C and then introduced into *E. coli* cells by heat-shock transformation.

Table 24: pGEM®-T vector ligation mix

Component	Volume
pGEM®-T vector	0.5 µl
PCR fragment	3 µl
2x Rapid Ligation buffer	5 µl
T4 DNA Ligase	1 µl

3.9.2 Heat-shock Transformation of *E. coli*

Hundred µl of chemically competent *E.coli* DH5α cell suspension was thawed on ice and mixed with 5 µl of ligation reaction product. After 30 min of incubation on ice, the cells were heat shocked for 45 sec at 42°C and placed back on ice for 10 min. After adding 400 µl of SOC medium, the cells were incubated on a thermomixer at 37°C for 45 min under gentle

agitation. Cells were then plated on pre-warmed LB-Agar plates containing 100 µg/ml ampicillin and incubated overnight at 37°C. Individual bacterial clones were picked from the plate with a pipette tip, resuspended in 5 ml LB-medium containing ampicillin (100 µg/ml), and again incubated overnight at 37°C. These cultures were later used for the purification of plasmid DNA from *E. coli* or further inoculations.

As the pGEM®-T vector is applicable for blue/white screening, cells transformed with this vector were cultured on LB-Agar plates (containing 100 µg/ml ampicillin) on which a mixture of 10 µl IPTG and 50 µl X-Gal solutions had been plated before. In this case, only white colonies (containing the DNA insert) were selected for further analysis.

3.9.3 Plasmid DNA Purification from *E. coli*

For small-scale isolation of plasmid DNA (e.g., applied for molecular cloning), one *E. coli* clone (picked from an LB-agar plate) or 10 µl of an *E. coli* cell culture were inoculated into 5 ml LB-medium supplemented with 100 µg/ml ampicillin and incubated overnight on a shaker at 37°C. The next day, small-scale isolation of plasmid DNA from the freshly grown *E. coli* cultures was performed using the NucleoSpin® Plasmid Mini kit according to the manufacturer's instructions. The plasmid DNA pellet was eluted in 25 µl of Milli-Q H_2O and stored at - 20°C until further use. DNA concentration was measured using the NanoDrop® ND1000 spectrophotometer.

For transfection-grade plasmid DNA purification, 50 µl of an *E. coli* cell culture were inoculated into 100 ml LB-medium supplemented with 100 µg/ml ampicillin and incubated overnight on a shaker at 37°C. The next day, the NucleoBond® Xtra Midi/Maxi Kit was used to purify plasmid DNA according to the manufacturer's instructions. The plasmid DNA pellet was dissolved in Milli-Q H_2O under constant gentle agitation for 60 min. To reach a final concentration of 1 µg/ml (measured by the NanoDrop® ND1000 spectrophotometer), the purified DNA was diluted with Milli-Q H_2O and stored at -20°C until further use.

3.9.4 Restriction Digestion and Cloning into Mammalian Expression Vectors

After confirmation of the correct sequence by Sanger sequencing (see 3.7), the PAI-1 coding sequences were transferred from the pGEM®-T cloning vector into the respective expression vectors. To this end, pGEM®-T containing the DNA insert were digested overnight at 37°C with EcoRI-HF and XhoI restriction enzymes in the digestion mixture shown in Table 25.

Table 25: Reaction mix for digestion of pGEM®-T cloning vector

Component	Volume
pGEM®-T	3 µg
EcoRI-HF	1 µl
XhoI	1 µl
Cutsmart buffer	1 or 2 µl
Milli-Q H_2O	ad. 10 or 20 µl

Using the same enzymes, 0.5 µg of target expression vectors (pcDNA3.1 or pEXPR-IBA103) was digested. After electrophoresis on 1% agarose gel, the digested DNA insert, and expression vectors were purified from the gel and ligated with a 3:1 molar ratio using T4 DNA ligase according to Table 26. Ligations were incubated at 4°C overnight and subsequently transformed into *E. coli* (see 3.9.2).

Table 26: Reaction mix for ligation of inserts into expression vectors

Component	Volume
pcDNA3.1 or pEXPR-IBA103	10-20 ng
Insert DNA	1 µl
10x T4 DNA Ligase buffer	1 µl
T4 DNA Ligase	1 µl
Milli-Q H_2O	ad. 10 µl

After overnight incubation of individual clones, plasmid DNA was isolated from *E. coli* cultures (see section 3.9.3) and expression constructs were verified by Sanger sequencing (3.7). The PAI-1-encoding expression vectors generated were named pcDNA3.1-PAI-1 and pEXPR-IBA103-PAI-1, respectively.

3.9.5 Bacterial Glycerol Stocks

The plasmid constructs generated were maintained in bacterial glycerol stocks. *E. coli* cells from 4 ml of fresh culture (cultured overnight as described in 3.9.3) were pelleted by centrifugation (5 min, 1000 rpm, 4°C; Centrifuge Megafuge 1.0R). The cell pellet was then resuspended in 500 µl of LB-medium (without antibiotics) and mixed with 600 µl of 80% sterile glycerol. The stocks were immediately frozen at -80°C. The data sheets of the plasmid constructs and their storage location were entered into the database of the Institute of Human Genetics (University of Regensburg, Germany).

3.10 Eukaryotic Cell Culture

Eukaryotic cell lines were maintained at a constant temperature of 37°C, in an atmosphere of 5% CO_2 and were passaged under sterile conditions. Cell status and confluency were checked microscopically each time they were passaged or before being used in the experiments. All cell culture media and supplies (listed in Table 12) were stored at 4°C unless otherwise indicated by the manufacturer and pre-warmed to 37°C before use.

3.10.1 Cultivation of HEK293-EBNA Cells

Human embryonic kidney cells HEK293-EBNA were maintained in 10 cm cell culture dishes in DMEM high-glucose medium containing 10% FCS, 1% penicillin/streptomycin and 1% G418 sulphate. Cells were sub-cultured at a ratio of 1:10 when they reached approximately 90% confluence.

3.10.2 Cultivation of HUVEC Cells

Human umbilical vein endothelial cells (HUVECs) were cultivated in T25 cell culture flasks in EGMPlus Endothelial cell growth medium containing EGMPlus SingleQuots kit supplements (but without gentamicin). After reaching approximately 90% confluence, cells were detached with a trypsin-EDTA solution (0.05%) and sub-cultured at a ratio of 1:3.

3.10.3 Cultivation of Y79 and WERI-Rb1 Cells

The human retinoblastoma cell lines Y79 and WERI-Rb1 were cultivated in suspension in T25 cell culture flasks in RPMI 1640 medium supplemented with 10% FCS and 1% penicillin/streptomycin. Cells were sub-cultured in a 1:3 ratio when they reached a concentration of 4-5 x 10^5 cells/ml (determined with CASY TT Cell Counter).

3.10.4 Cultivation of ARPE-19 Cells

Adult retinal pigment epithelium (ARPE-19) cells were maintained in 10 cm cell culture dishes in DMEM/F12 containing 10% FCS and 1% penicillin/streptomycin solution. After reaching approximately 90% confluence, cells were detached with a trypsin-EDTA solution (0.05%) and sub-cultured at a ratio of 1:3.

3.10.5 Cultivation of Human Induced Pluripotent Stem Cells-derived RPE (hiPSC-RPE) Cells

hiPSC-RPE cells were kindly provided by Dr. Karolina Plössl (Institute of Human Genetics, University of Regensburg, Germany). After thawing, cells were cultivated for 2 weeks on 6-well plates coated with Matrigel® GFR in KnockOut DMEM Medium supplied with 2 mM L-Glutamine, 5% (v/v) KnockOut Serum Replacement, 0.1 mM Gibco MEM non-essential amino acids, 5 µg/ml gentamycin, 0.1 mM β-Mercaptoethanol, and 10 mM nicotinamide. After 2 weeks, cells were detached with TrypLE, passaged in a 6-well plate at a 1:6 ratio, and cultivated for another 2 weeks before seeding onto 12-well Transwell filters (coated with Matrigel® GFR) in 1:12 ratio. Unless stated otherwise, cells were maintained on Transwell filters for 6 weeks to allow polarized growth, with a change of culture medium every two days. Cells were used in the experiments during weeks 6-8.

3.10.6 Investigations on the Differentiation State of hiPSC-RPE Cells

Characterization of hiPSC-RPE cells during sub-cultivation included monitoring the peculiar RPE cobblestone cell morphology, RPE specific gene expression, and correct localization of RPE-specific markers, as well as integrity and permeability of the cell monolayer.

3.10.6.1 Investigating RPE Specific Gene Expression

To investigate the degree of RPE differentiation, expression of the RPE markers *RPE65, BEST1, RLBP1,* and *ITGB8*, the melanogenesis marker *TYR*, and stem cell markers *OCT4*

and *SOX2* was analysed *via* reverse transcription and targeted PCR amplification of total RNA (as described in paragraph 3.3 and 3.4 with primers given in Table 2) derived from hiPSC-RPE cells in comparison to RNA from undifferentiated hiPSCs. PCR products were separated electrophoretically on 2% agarose gel and visualized with an UV transilluminator placed in a dark hood DH-40 (Biostep GmbH, Jahnsdorf, Germany). Analysis of *GUSB* expression served as housekeeper (**Figure 6A**).

3.10.6.2 Immunofluorescence Staining of RPE Cellular Markers

hiPSC-RPE cells on Transwell filters were fixed with 2% PFA solution (Table 11) for 10 min followed by three washing steps for 5 min with DPBS. Upon blocking in blocking solution (Table 11) for 30 min at RT, filters were incubated with primary antibodies (anti-BEST1, anti-ATP1A1, anti-ATP1B1, anti-ZO-1, for antibody solution see Table 11) at 4°C overnight. After three washing steps with DPBS, cells were incubated in fluorescently labelled secondary antibodies (for antibody solution see Table 11) for 1 h at RT. After three washing steps, filters were mounted onto microscope slides using Dako Fluorescence Mounting Medium. All filters were counterstained with DAPI for visualization of cell nuclei. Confocal microscopy (**Figure 6 B**) and vertical z-projection (**Figure 6 C, D, E**) verified the expression and correct (basolateral) localization of the RPE-specific marker Bestrophin-1 (BEST1), the apical polarity of sodium/potassium-transporting ATPase subunit α-1 (ATP1A1) and β-1 (ATP1B1), and the formation of *zonula occludens* (ZO).
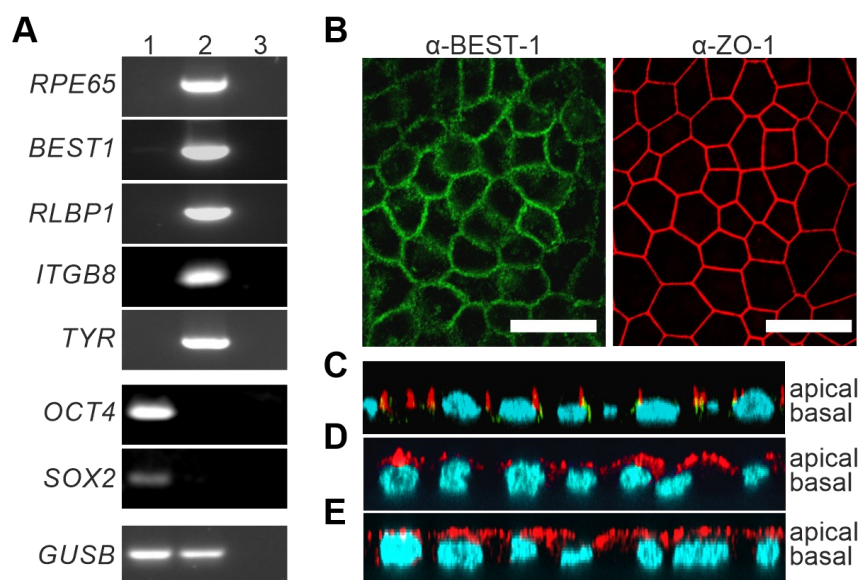
Figure 6: Profiling of hiPSC-RPE cells.
(**A**) Expression of mature RPE genes *RPE65*, *BEST1*, *RLBP1*, and *ITGB8*, the melanogenesis marker *TYR* and stem cell markers *OCT4* and *SOX2* in hiPSCs (lane 1) and hiPSC-RPE (lane 2). No RNA was added to the negative control (lane 3). The housekeeping gene *GUSB* was used to control for RNA integrity. (**B**) Immunofluorescence staining against basolateral/lateral markers BEST1 (green) and zonula occludens 1 (ZO-1, red). Scale bars 20 μm. (**C**) Vertical z-projection after immunofluorescence staining against BEST1 (green), ZO-1 (red), (**D**) apical markers ATP1A1 (red) and (**E**) ATP1B1 (red). Nuclei were visualized with DAPI (blue). (Figure modified from Biasella et al., 2020 [246]).

3.10.6.3 Measurements of Transepithelial Electrical Resistance

Transepithelial electrical resistance (TEER) of hiPSC-RPE monolayer was measured with an epithelial Volt/Ohm (Ω) Meter after 6 weeks of cultivation, according to the manufacturer's instructions. For measurements, the electrodes were sterilized in 70% ethanol for 15 min, rinsed in 150 mM NaCl solution and placed in the respective Transwell filter, with the longer voltage electrode positioned in the lower chamber while the shorter current electrode was placed in the upper chamber. Blank measurements were taken from Matrigel® coated Transwell filters which did not contain any cells. After subtracting the mean of the blank values from the cell monolayer-derived measurements, net values were multiplied with the surface area of the Transwell filter and reported as $\Omega \times cm^2$. A high stable transepithelial resistance of >150 $\Omega \times cm^2$ (233.3 ± 53.2 $\Omega \times cm^2$) for differentiated hiPSC-RPE cells confirmed the correct integrity and permeability of the hIPSC-RPE monolayer, consistent with the reported net TEER of human RPE *in vivo*, ranging from 150 to 200 $\Omega \times cm^2$ [247-249].

3.10.7 Cell transfection

3.10.7.1 Transfection of HEK293-EBNA with the Calcium Phosphate Method

For heterologous expression and purification of Strep-tagged vitronectin isoforms (VTN_rs704:C and VTN_rs704:T) and Strep-tagged PAI-1, pEXPR-IBA103 vectors containing the respective coding sequences were transfected into HEK293-EBNA cells using the calcium phosphate method [250]. The day before transfection, HEK293-EBNA cells from a confluent 10 cm dish were passaged at a ratio of 1:3 into 10 cm cell culture dish previously coated with poly-L-Lysine. On the day of transfection, cells were incubated with DMEM High Glucose Medium (4.5 g/l) containing 10% FCS, 1% penicillin/streptomycin and 25 µM chloroquine for 1 h at 37°C. Meanwhile, the transfection mixture was prepared according to Table 27 by first mixing the DNA with Milli-Q H_2O followed by the addition of $CaCl_2$. Subsequently, HBS was added to the tube by gently pipetting to the bottom. The two resulting phases were mixed by gently bubbling air droplets into the solution.

Table 27: Composition of the calcium-phosphate transfection mixture

Component	Volume/Amount
Plasmid DNA	40 µg/ml
Milli-Q H_2O	ad.438 µl
$CaCl_2$	62 µl
2x HBS	500 µl

Directly prior to transfection, the medium containing chloroquine was replaced with normal high-glucose DMEM culture medium (4.5 g/l) containing 10% FCS, 1% penicillin/streptomycin and 1% G418 sulphate, and the transfection mixture was added to the cells dropwise. Seven h after transfection, cells were washed once with DPBS and incubated

in FCS-free medium containing 1% penicillin/streptomycin and 1% G418 sulphate for 72 h. Subsequently, the medium containing secreted Strep-tagged proteins was collected, centrifuged to remove cell debris (5 min; 500 rpm; Centrifuge Multifuge 3L-R), and stored at -20°C until further use. Medium harvested from HEK293-EBNA transfected with an empty vector in a procedure identical to that described above served as a negative control.

3.10.7.2 Transfection of HEK293-EBNA with Mirus TransIT®-LTI Transfection Reagent

HEK293-EBNA cells were passaged from a 10 cm confluent dish at a ratio of 1:18 into a 6-well plate or at a ratio of 1:40 in a 12-well plate and incubated overnight in high glucose DMEM medium (4.5 g/l) containing 10% FCS, 1% penicillin/streptomycin and 1% G418 sulphate. The transfection was carried out using the TransIT®-LTI transfection reagent according to the manufacturer's instructions. For co-transfection experiments with two plasmids, half of the amount of DNA was used for each plasmid. The transfected cells were incubated in FCS-free medium for 48 or 72 h at 37°C.

3.10.7.3 Transfection of ARPE-19 Cells with Lipofectamine™ 3000 Transfection Reagent

ARPE-19 cells were passaged from a 10 cm confluent dish at a ratio of 1:6 into a 6-well plate or at a ratio of 1:12 into a 12-well plate and incubated overnight in DMEM/F12 containing 10% FCS and 1% penicillin/streptomycin. The transfection was carried out following the Lipofectamine™ 3000 Transfection Reagent protocol according to the manufacturer's instructions, with minor changes in the volumes used (see Table 28). The transfected cells were incubated in FCS-free medium for 48 or 72 h at 37°C.

Table 28: Composition of Lipofectamine™ 3000 transfection mixture

Component	Volume (per 6-well)	Volume (per 12-well)
Lipofectamine™ 3000	10 µl	5 µl
P3000™ reagent	10 µl	5 µl
DNA (1 µg/ml)	2.5 µl	1.25 µl
Medium	250 µl	125 µl

Unless otherwise indicated, half of the volume of the DNA was used for each plasmid in co-transfection experiments with two plasmids.

3.10.8 Isolation of Primary Porcine RPE Cells

Porcine RPE were isolated from fresh pig eyes obtained from a local slaughterhouse as described in [251], with only minor modifications. Briefly, porcine eyes were opened through an incision along the ora serrata and the vitreous was removed. After incubation in PBS-EDTA (Table 11), the retinas were discarded and the eye cups were incubated again in PBS-EDTA for 45 min, followed by a 35 min incubation in dissociation buffer containing papain (Table

11). Papain activity was stopped by adding 2% FCS in DPBS. RPE cells were dissociated by suction/pipetting up and down with cell culture medium (KnockOut DMEM Medium supplied with 2 mM L-Glutamine, 0.1 mM Gibco MEM Non-essential amino acids, 5 µg/ml gentamycin, 0.1 mM β-Mercaptoethanol, and 10 mM nicotinamide). The cell suspension was centrifuged (5 min, 1000 rpm, Sigma 2-5 centrifuge) and the cells were used in binding assays (see section 3.27) and adhesion experiments (see section 3.31).

3.11 Sodium Dodecyl Sulphate-Polyacrylamide Gel Electrophoresis (SDS-PAGE)

3.11.1 Reducing SDS-PAGE

Protein analysis by western blot or Coomassie staining was preceded by reducing SDS-PAGE for mass-based protein separation. Unless otherwise indicated, protein samples were run on gels consisting of a 12.5% acrylamide resolving layer and a 3% acrylamide stacking layer. Using Bio-Rad MiniPROTEAN® equipment, 1.5 mm thick gels were prepared for western blot analysis, and 0.75 mm thick gels were prepared for Coomassie staining, according to Table 29. Prior to gel loading, samples were sonicated (amplitude: 40%; time: 20 sec) and heated in 5x Laemmli buffer at 93°C for 5 min. As a size standard, 5 µl of PageRuler™ Prestained Protein Ladder was loaded onto the gel. The gels were run in SDS buffer at 50 V until the samples entered the resolving gel and then at 150 V for approximately 2 h depending on the size of the proteins to be analysed.

Table 29: Composition of gels used for reducing SDS-PAGE

Component	Resolving gel		Stacking gel
	10%	12.5%	3%
1 M Tris/HCl pH 8.8	3.83 ml	3.83 ml	-
1M Tris/HCl pH 6.8	-	-	2.75 ml
dH$_2$O	3.66 ml	3.03 ml	1.70 ml
Acrylamide (40%)	2.5 ml	3.13 ml	0.55 ml
SDS (20%)	100 µl	100 µl	50 µl
APS (10%)	100 µl	100 µl	50 µl
TEMED	10 µl	10 µl	10 µl

3.11.2 Non-Reducing SDS-PAGE

For protein separation under non-reducing conditions, samples were run on 1.5-mm thick acrylamide gels consisting of a 7% resolving layer and a 3% stacking layer (see Table 30 for gel composition). Prior to gel loading, samples were heated in 5x Laemmli buffer without β-Mercaptoethanol at 93°C for 5 min. For the analysis of vitronectin multimers (see section 3.22), Colour-coded Pre-stained Protein Marker, High Range was used as size standard (10 µl). Running conditions were identical to those described in 3.11.1.

Table 30: Composition of gels used for non-reducing SDS-PAGE

Component	Resolving gel (7%)	Stacking gel (3%)
1 M Tris/HCl pH 8.8	3.83 ml	-
1M Tris/HCl pH 6.8	-	2.75 ml
dH$_2$O	4.420 ml	1.70 ml
Acrylamide (40%)	1.75 ml	0.55 ml
SDS (20%)	100 µl	50 µl
APS (10%)	100 µl	50 µl
TEMED	10 µl	10 µl

3.12 Western Blot

Following SDS-PAGE, proteins were transferred onto PVDF membranes by semi-dry blotting using the Bio-Rad Transblot transfer system. The membranes were activated in methanol for 30 sec, and then equilibrated for at least 5 min in Towbin transfer buffer. Similarly, two 3 mm Whatman filter papers and the SDS gel were equilibrated in Towbin transfer buffer. The gel and blotting membranes were assembled in a sandwich along with the filter papers. Protein transfer from the gels onto the membranes was performed at 24 V for 40 min using the Trans-Blot® Turbo™ Transfer System.

After blotting, the membranes were immersed in blocking solution for 1 h at RT and then incubated with primary antibodies in primary antibody solution (see Table 11) overnight at 4°C. Prior to incubation with secondary antibodies, the membranes were washed three times for 5 min in TBS-T at RT. Incubation with the secondary antibodies in secondary antibody solutions (see Table 11) was performed at RT for 1 h, followed by washing of the membranes (3x 5 min in TBS-T). Proteins were visualised by chemiluminescence using Clarity™ ECL Western Blotting Substrate (Bio-Rad) according to the manufacturer's instructions using an Odyssey FC imager. For protein targets showing only weak signals, Clarity Max™ Western Blotting substrate was used to increase signal intensity.

3.13 Coomassie Blue Staining

Coomassie blue staining of proteins on SDS gels was applied directly after SDS-PAGE. The gels were immerged in Coomassie staining solution for 1 h and then in Coomassie de-staining solution until the distinct protein species were visible. De-staining solution was replaced by fresh de-staining solution after 1 and 3 h, respectively. The staining and de-staining procedures were carried out at RT under gentle agitation on a shaker.

3.14 Blue Native PAGE

For analysis of protein complexes stabilized by non-covalent bonds, samples were separated under native conditions by Blue Native PAGE. Samples were run on pre-cast 4-16% NativePAGE™ Bis-Tris gels at 4°C, according to the manufacturer's instructions. Proteins

were transferred onto PVDF membranes by wet electroblotting overnight using the Bio-Rad Mini Trans-Blot® cell. NuPAGE™ transfer buffer was used according to the manufacturer's instructions. Proteins transferred to PVDF membranes were subjected to western blot analysis.

3.15 Purification of Recombinant Proteins

Vitronectin (NP_000629.3) isoforms (VTN_rs704:C and VTN_rs704:T) and PAI-1 (NP_000593.1) were purified in their respective Strep-tagged forms from the culture medium of transiently transfected HEK293-EBNA cells by affinity chromatography. Purification was performed using the Twin-Strep Purification Kit at 4°C with pre-cooled buffers, according to the IBA Life Sciences short purification protocol. Column specifications and buffer volumes used for the purification of VTN_rs704:C, VTN_rs704:T, or PAI-1 are shown in Table 31. Ten µl of all six elution fractions was subjected to western blot analyses using antibodies against vitronectin or PAI-1. The three fractions with the highest content of the respective eluted proteins (E2+E3+E4 for VTN_rs704:C and VTN_rs704:T, E3+E4+E5 for PAI-1; **Figure 7A**) were combined. Protein purification was controlled in the combined fractions, using western blot analysis (**Figure 7B**) and Coomassie blue staining (**Figure 7C**). Strep-tagged PAI-1 was recognised as a major species of molecular weight slightly above 55 kDa (50-54 kDa for glycosylated PAI-1, as previously reported [252,253], plus 5.1 kDa for the Strep-tag), with an additional smaller molecular weight species occasionally appearing [254,255], labelled by white arrows in **Figure 7A, C**. Purified Strep-tagged VTN_rs704:C and VTN_rs704:T showed molecular weights of about 80 kDa (75 kDa for the uncleaved vitronectin isoform, plus 5.8 kDa for the Strep-tag) and 65 kDa for the cleaved vitronectin isoform (untagged after cleavage of the 10 kDa C-terminal vitronectin fragment which is fused to the Strep-tag and undetectable with the applied antibody). Aliquoted in 100 µl fractions, the purified proteins were stored at -20°C.

Table 31: Applied affinity chromatography columns and volumes of buffers used for purification of Strep-tagged proteins

	Gravity flow Strep Tactin Superflow® column capacity	**Culture medium applied**	**Strep-Tactin ®wash buffer**	**Strep-Tactin ®elution buffer**
Purification of vitronectin	1 ml	70-100 ml	5x 1 ml	6x 0.5 ml
Purification of PAI-1	5 ml	300-500 ml	5x 5 ml	6x 2.5 ml

The culture medium from HEK293-EBNA cells transfected with an empty vector (pEXPR-IBA103) was subjected to the identical purification procedure. The obtained eluates ("control eluate") served as negative control in experiments conducted with the purified proteins.
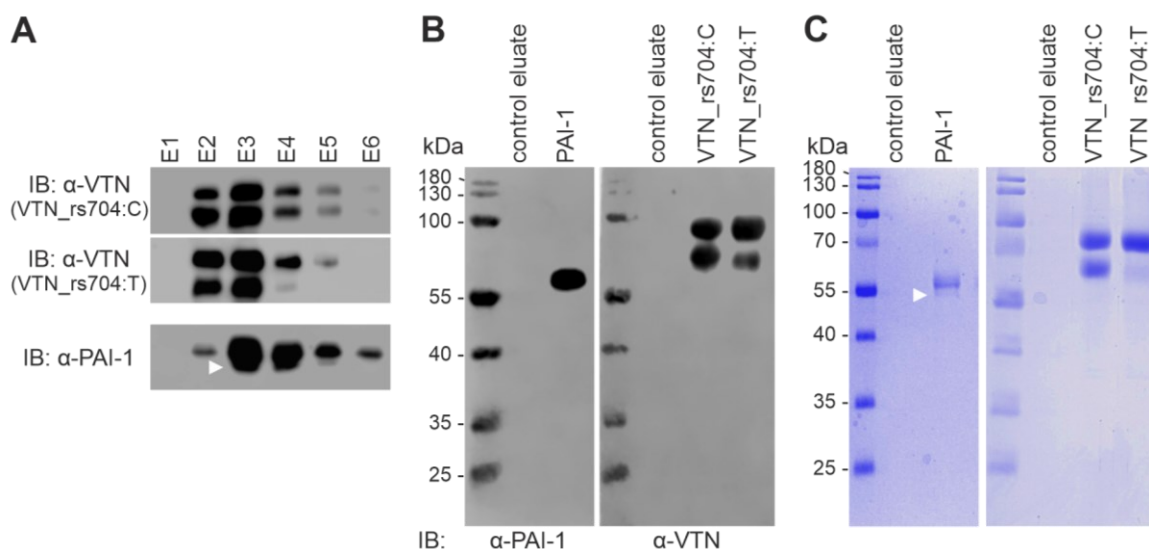
Figure 7: Purification of Strep-tagged VTN_rs704:C, VTN_rs704:T and PAI-1.
The six elution fractions (E1 to E6) collected during purification were subjected to SDS-PAGE and analysed *via* (**A**) immunoblot (IB) using antibodies against vitronectin (α-VTN) and PAI-1 (α-PAI-1). The most concentrated fractions were pooled and used in the experiments. (**B**) IB analysis and (**C**) Coomassie blue staining of pooled eluates. Eluates obtained from culture medium of HEK293-EBNA transfected with empty pEXPR-IBA103 vector and subjected to the same purification procedure served as a control (control eluate). White arrowheads indicate the additional smaller PAI-1 band, occasionally observed after expression/purification of PAI-1 (as also described in [254,255].

3.16 Measurement of Protein Concentration

Protein concentration was measured according to Bradford's method [256] using the Roti®-Quant reagent and bovine serum albumin (BSA) as a standard. Eight hundred µl of Milli-Q H_2O was mixed with 200 µl of Roti®-Quant, and 5-15 µl of the protein sample to be measured was added. After 20 min of incubation at RT, the absorbance at 595 nm was measured with the Ultrospec 2100 pro UV/Visible spectrophotometer. The protein concentration was determined with the help of a titration curve from known concentrations of BSA.

The concentration of vitronectin isoforms (VTN_rs704:C and VTN_rs704:T) were additionally investigated by semi-quantitative western blot analysis comparing signal intensities of the purified vitronectin isoforms to signal intensities of a commercially available recombinant vitronectin protein (10424-H08H; Sino Biological) loaded in different concentrations.

For dilution or adjustment of purified VTN_rs704:C, VTN_rs704:T and PAI-1 to the concentrations given in the respective experiments, the Strep-Tactin® elution buffer was used.

3.17 Partial Rapid Proteolysis Assay

Fifteen µl of 1.5 µg/ml purified recombinant vitronectin (isoforms) were pre-incubated at 37°C or 42°C or kept on ice without pre-incubation. After 10 min, 5 µl of 50 µg/ml TPCK-trypsin in Tris-buffered saline was added to the samples, and the mixtures were kept at 37°C for further 5 min. As a control, 15 µl of purified protein without or with the same pre-incubation

steps were mixed with 5 µl of only Tris-buffered saline and subjected to the 5 min incubation step at 37°C. The mixtures were finally boiled with 5 µl 5x Laemmli buffer for 5 min at 95°C, subjected to SDS-PAGE in 10% acrylamide gels, and analysed by western blot.

3.18 Analysis of Endogenous Vitronectin Expression in Different Cell Lines

Endogenous vitronectin expression was tested in ARPE-19, hiPSC-RPE, Y79, WERI-Rb1, HUVEC, and HEK293-EBNA cells.

3.18.1 Vitronectin mRNA Expression

For RNA isolation, half of the ARPE-19 cells grown to confluence in a 10 cm dish, a third of the HEK293-EBNA cells from a confluent 10 cm dish, hiPSC-RPE cells from 4 Transwell filters and Y79, WERI-Rb1, as well as HUVECs from a fully grown T25 flask were used. After reverse transcription of the isolated total RNA (see sections 3.2 and 3.3), the *VTN* coding sequence was amplified by PCR with the oligonucleotide primers given in Table 2. Amplification of the *GUSB* coding sequence served as control. The PCR products were electrophoresed on 1.7% agarose and visualised with an UV transilluminator placed in a dark hood DH-40 (Biostep GmbH, Jahnsdorf, Germany).

3.18.2 Vitronectin Protein Expression

The preparation of cell lysates from cultured ARPE-19, hiPSC-RPE, Y79, WERI-Rb1, HUVEC and HEK293-EBNA cells and the determination of the respective total protein concentrations *via* the Bradford method [256] was performed by medical doctoral student Martin Zankel. Forty µg of total protein was used for all cell lines. Samples were mixed with 5x Laemmli buffer and heated at 95°C for 5 min. Proteins were then separated by SDS-PAGE as outlined in section 3.11.1 and subjected to western blot analysis (see section 3.12).

3.19 Analysis of rs704 Allele-specific mRNA Expression in hiPSC-RPE and Human Neural Retinal Samples

Vitronectin mRNA expression was investigated *via* analysis of sequence electropherogram of allele-specific transcripts in hiPSC-RPE cells and human neural retina samples (Institute of Human Genetics, University of Regensburg, Germany), which were heterozygous for rs704. Genomic DNA and RNA were isolated from hiPSC-RPE cells and human neural retina samples, following the procedures described in sections 3.1 and 3.2. The RNA was then transcribed into cDNA (see 3.3). The cDNA sequence regions comprising rs704 were amplified by PCR (see section 3.4) with primers VTN_SeqInt2_F and hVTN_Ex7-R given in Table 2. Successful amplification was verified by electrophoresis of the PCR products on 1.5% agarose gels (see section 3.5). Excess primers and dNTPs were removed by treatment with exonuclease I and Antarctic phosphatase for 15 min at 37°C, followed by further 15 min at 80°C according to Table 32.

Table 32: Reaction mix for PCR products treatment with Exonuclease and Antarctic phosphatase

Component	Volume
Exonuclease	0.1 µl
Antarctic phosphatase	0.25 µl
PCR product	1 µl
Milli-Q H_2O	ad. 5 µl

Sanger sequencing was performed with sequencing primer hVTN_Ex7-R given in Table 2, according to the protocol described in section 3.7. Sequence electropherograms were visualised with the ApE-A Plasmid Editor software.

3.20 Analysis of rs704 Allele-specific Heterologous Vitronectin Protein Expression and Processing

HEK293-EBNA and ARPE-19 cells were co-transfected in 12-well plates with pcDNA3.1-GFP in combination with empty pcDNA3.1, pcDNA3.1-VTN_rs704:C, or pcDNA3.1-VTN_rs704:T, respectively, according to the transfection methods described in sections 3.10.7.2 and 3.10.7.3. After 48 and 72 h, the medium (1 ml) was collected and centrifuged to remove cellular debris (5 min, 800 rpm, 4°C; Centrifuge Eppendorf 5415R). Cells were scraped in 300 µl DPBS and pelleted by centrifugation (5 min, 4500 rpm, 4°C; Centrifuge Eppendorf 5415R). After a second wash with 300 µl DPBS, the cell pellet was resuspended in 100 µl of DPBS. Cells and supernatant were subjected to SDS-PAGE (see 3.11.1) and western blot analysis (see 3.12) with antibodies against vitronectin, GFP and ACTB.

3.21 Analysis of Endogenous Proteolytic Cleavage of Vitronectin

HEK293-EBNA cells were co-transfected in 6-well plates with pcDNA3.1-PAI-1 in combination with empty pcDNA3.1, pcDNA3.1-VTN_rs704:C, or pcDNA3.1-VTN_rs704:T, respectively, according to the transfection method described in section 3.10.7.2. Co-expression of PAI-1, a known plasmin inhibitor, was performed to prevent endogenous plasmin-mediated cleavage of vitronectin on the carboxy-terminal side of R380 [257,258] in order to better visualize the different accessibility of VTN_rs704:C and VTN_rs704:T towards the endogenous intracellular furin protease, which mediates cleavage on the carboxy-terminal side of R398 [204], susceptible to rs704 [237]. After 48 h, cells were resuspended in their medium and pelleted by centrifugation (5 min, 800 rpm, 4°C; Centrifuge Eppendorf 5415R). The supernatant (culture medium) was collected, and the cell pellets were washed in 300 µl DPBS, pelleted (5 min, 4500 rpm, 4°C; Centrifuge Eppendorf 5415R) and finally resuspended in 200 µl DPBS. Cells and supernatant were subjected to SDS-PAGE (see 3.11.) and western blot analysis (see 3.12) with antibodies against vitronectin, PAI-1 and ACTB.

3.22 Analysis of rs704-dependent Vitronectin Multimerization

Twenty µl of purified recombinant VTN_rs704:C and VTN_rs704:T were subjected to non-reducing SDS-PAGE (see section 3.11.2) at a concentration of 10 ng/ml, and to BN-PAGE (see section 3.14) at a concentration of 85 ng/µl. Subsequently, western blot analyses (see 3.12) with antibodies against vitronectin were performed.

3.23 Analysis of rs704-dependent Vitronectin Binding to Immobilized PAI-1

The binding of VTN_rs704:C and VTN_rs704:T to PAI-1 was investigated by affinity chromatography of vitronectin to immobilized PAI-1. Seventy-five µl of purified recombinant Strep-tagged PAI-1 (100 µg/ml) was loaded onto gravity flow columns (0.2 ml Strep-Tactin Sepharose columns) pre-equilibrated with 200 µl of Strep-Tactin® wash buffer (buffer W) and incubated for 15 min. After washing the columns five times with 200 µl buffer W, 2.0 ml of culture medium containing untagged VTN_rs704:C or VTN_rs704:T (FCS-free medium of HEK293-EBNA cells transfected with pcDNA3.1-VTN_rs704:C or pcDNA3.1-VTN_rs704:T, adjusted for vitronectin concentrations) was loaded onto the columns and incubated for 1 h. In the medium, the concentration of untagged recombinant vitronectin was estimated to be approximately 5 µg/ml by comparative western blot analysis with a commercially available recombinant vitronectin protein (10424-H08H; Sino Biological). After six washing steps with 200 µl buffer W, proteins were eluted five times with 100 µl of Strep-Tactin® elution buffer (buffer E). To investigate putative non-specific binding of vitronectin to the column material, the VTN_rs704:C- or VTN_rs704:T-containing medium was loaded onto PAI-1-free columns in otherwise identical affinity chromatography experimental procedures. The pooled elution fractions were analysed via SDS-PAGE (see 3.11.1) and western blot analysis (see 3.12) with antibodies against vitronectin and PAI-1.

3.24 Analysis of Endogenous PAI-1 Protein Expression in Cultured Endothelial and RPE cells

ARPE-19 and HUVEC cells were passaged from a 10 cm confluent dish and a T25 confluent flask, respectively, at a 1:6 ratio onto 6-well plates and incubated for 24 h. After 24 h incubation, the culture medium was replaced by FCS-free culture medium, upon washing the cells once with 1 ml DPBS. After further 72 h of incubation, the culture medium was collected and the cells were scraped in 300 µl DPBS, pelleted (5 min, 4500 rpm, 4°C; Eppendorf 5415R centrifuge) and finally resuspended in 200 µl DPBS. Cell pellet samples were sonicated (amplitude: 40%; time: 20 sec) and the total protein concentration of the obtained cell lysates was measured by the Bradford method [256], using Roti®-Quant reagent and BSA as a standard. Ten µg of total protein was used for each cell line and, together with the culture medium samples, subjected to SDS-PAGE (see section 3.11.1) and western blot analysis (see section 3.12). As a positive control, 2 µg/ml of recombinant PAI-1 purified from

the culture medium of HEK293-EBNA cells transfected with the expression vector for PAI-1 was loaded.

3.25 Analysis of Endothelial PAI-1 Expression and Deposition After Exposure to Recombinant VTN_rs704:C and VTN_rs704:T

Confluent HUVECs (passages 3-4) from a T-25 flask were passaged onto 24-well plates at a density of 5.0×10^5 cells/well for subsequent mRNA analysis and 3.75×10^5 cells/well for subsequent protein analysis (cell concentration determined with CASY TT Cell Counter). After seeding, 20 µg/ml of VTN_rs704:C or VTN_rs704:T, or an equal volume of control eluate was added to the cells, which were then incubated at 37°C in FCS-free HUVEC culture medium. After 24 h, mRNA expression of *PAI-1* and *HPRT* (housekeeping gene) was followed by qPCR with oligonucleotide primers and probes given in Table 2.

For protein analysis, the medium was removed after 24 h, and cells were gently scraped off with a mini cell scraper in 300 µl DPBS. After centrifugation (5 min, 4500 rpm, Sigma 2-5 centrifuge), the cell pellet was resuspended in 50 µl DPBS. To collect the ECM deposited by HUVECs, 200 µl of decellularization buffer (see Table 11) was added to the wells for 5 min at RT to lyse any remaining cells. After washing five times with DPBS, 40 µl of hot Laemmli buffer (95°C) mixed with 100mM dithiothreitol (DTT) was pipetted onto the wells and the ECM was scraped into this buffer. The collected cells and ECM samples were subjected to SDS-PAGE (see 3.11.1) followed by western blot analysis (see 3.12) with antibodies against vitronectin, PAI-1 and ACTB.

3.26 Analysis of ECM Deposition by ARPE-19 Cells Heterologously Expressing VTN_rs704:C and VTN_rs704:T

ARPE-19 cells grown on a 6-well plate were co-transfected with pcDNA3.1-GFP and pcDNA3.1, pcDNA3.1_VTN_rs704:C, or pcDNA3.1_VTN_rs704:T using Lipofectamine™ 3000 Transfection Reagent, as described in section 3.10.7.3. After 24 h, GFP fluorescence was assessed as a marker for transfection efficiency using Nikon Eclipse microscope. Transfected ARPE-19 cells were enzymatically dissociated from the cell culture plate with trypsin–EDTA and 4×10^5 cells (determined with CASY TT Cell Counter) were seeded onto 12-well Transwell filters (0.4-µm pore size) in DMEM/HamsF12 containing 10% FCS and 1 % penicillin/streptomycin. After 24 h, the medium was changed to FCS-free medium containing 1% penicillin/streptomycin and supplemented with 200 µg/ml dextran sulphate and 30 µg/ml ascorbic acid, according to [259]. Confluent ARPE-19 monolayers were cultured in this medium for 4 or 8 weeks with media changes three times per week. After the incubation period, cells were removed from the filter by decellularization for 5 min at 37°C with 500 µl (upper chamber) and 1.5 ml (lower chamber) decellularization buffer (see Table 11). After decellularization, filters were washed five times with DPBS (500 µl on the upper chamber and

1.5 ml on lower chamber) and the deposited ECM was fixed for subsequent immunofluorescence analyses, with the procedure described in paragraph 3.10.6.2. Immunostaining was performed with one quarter filter per staining experiment. Pictures were taken with a confocal laser scanning microscope. Signal intensity and average cluster size were measured using ImageJ.

3.27 Cell Membrane Binding assay

The binding of VTN_rs704:C and VTN_rs704:T to ARPE-19, hiPSC-RPE, porcine RPE, Y79, and HUVECs was tested by suspending cell pellets (Y79: cells from one or two fully grown T25 flasks, respectively; ARPE-19: cells from one fully grown 10 cm dish; hiPSC-RPE: cells from six 12-well filters; porcine RPE cells: RPE cells from one eye) in 600 μL of DPBS. The 600 μl suspensions were split into three 200 ul fractions which were centrifuged (5 min, 4500 rpm, 4°C; Eppendorf 5415R centrifuge). The three pellets were resuspended in 1 ml of vitronectin-containing medium from HEK293-EBNA cells previously transfected with pcDNA3.1-VTN_rs704:C or pcDNA3.1-VTN_rs704:T, or in 1 ml of medium from cells transfected with an empty vector. After 1 h incubation at 37°C under constant shaking (400 rpm), cells were washed three times with 1 ml DPBS (followed by centrifugation for 5 min, 4500 rpm, 4°C; Eppendorf 5415R centrifuge). The pellet resuspended in 200 μl PBS was subjected to SDS-PAGE (3.11.1) and western blot analysis (3.12) with antibodies against vitronectin and ACTB.

3.28 Endothelial Cell Migration ("Scratch-Wound") Assay

HUVEC migration was determined in the scratch-wound test, as described in [260], with slight modifications: HUVECs were passed from a confluent T25 flask at a ratio of 1:35 into a flat-bottom 96-well plate and incubated in HUVEC cultured medium with EGMPlus SingleQuots supplements. After 24 h, monolayers of confluent cells were scratched using a Wound Maker. Cell debris was removed by washing with DPBS, and injured monolayers were incubated in 100 μl EGMPlus Endothelial Cell Growth Media with EGMPlus SingleQuots supplements except FCS and gentamycin, 50 ng/ml VEGF and 20 μg/ml purified recombinant vitronectin (VTN_rs704:C or VTN_rs704:T) or equal volumes of control eluate. Minimum four pseudo replicates (individually treated wells) per treatment were performed for each independent replicate. After 0 and 14 h, images of each well were captured at 4x magnification with a Nikon Eclipse microscope. Scratch areas were determined using an ImageJ script for automatic quantification of HUVEC migration kindly provided by Dr. Christina Kiel (Institute of Human Genetics, University of Regensburg, Germany). Cell migration capacity was defined as the percentage area closed after 14 h of incubation.

3.29 Enzymatic PAI-1 Activity Assay

The effect of vitronectin isoforms on PAI-1 activity was followed by incubating 7.5 µg/ml of purified recombinant PAI-1 with 7.5 µg/ml of purified recombinant VTN_rs704:C, VTN_rs704:T, or control eluate for 7 h at 37°C. After 0, 1, 2, 3, 4, 5, and 7 h, or after 0 and 72 h, 10 µl of the assay mixture were removed and subjected to the CHEMICON PAI Activity Assay Kit (Sigma-Aldrich), according to the manufacturer's protocol. In this assay, the ability of PAI-1 to inhibit its physiological ligand uPA is assessed colorimetrically by quantifying a chromogenic substrate, which is cleaved by active uPA. Specifically, the vitronectin/control eluate and samples containing PAI-1 were first incubated with uPA for 30 min at 37°C, followed by the chromogenic enzymatic reaction for 2 h at 37°C. Subsequently, the absorbance of the chromogenic substrate was measured at 405 nm using a Spark multimode microplate reader.

3.30 Endothelial Tube Formation Assay

Endothelial tube formation in response to vitronectin exposure was examined in HUVECs as described in [261], with minor modifications. 8.5×10^3 HUVECs/well were seeded onto a flat-bottom 96-well plate coated with 37.5 µL Geltrex LDEV-Free Reduced Growth Factor Basement Membrane Matrix. Cells were then cultured in 100 µl HUVEC culture medium containing 1/3 EGMPlus SingleQuots supplements without gentamycin, 50 ng/ml VEGF, and 5 µg/ml purified recombinant VTN_rs704:C or VTN_rs704:T, or equal volumes of control eluate. Minimum three pseudo replicates (individually treated wells) per each treatment were included in one independent replicate. After 16 h, images from each well were captured at 4x magnification with a Nikon Eclipse microscope. Cumulative tube length was quantified using the Angiogenesis Analyzer in ImageJ as described [262].

3.31 Adhesion Assay

VTN_rs704:C and VTN_rs704:T were compared in their capacity to mediate adhesion of hiPSC-RPE, porcine RPE and HUVEC cells. Prior to the assay, cell suspensions were prepared as follows: hiPSC-RPE cells were dissociated from a 12-well Transwell filter using TrypLE for 40 min at 37°C and resuspended in 600 µl of serum-free culture medium. Porcine RPE cells were isolated from a pig eye (see section 3.10.8) and resuspended in 600 µl of serum-free medium. HUVECs from a T25 cell culture flask were resuspended in 1.2 ml of FCS-free culture medium.

3.31.1 Adhesion Assay with Purified Recombinant Vitronectin

Hundred µl of hiPSC-RPE, porcine RPE or HUVEC cell suspension was mixed with 1.5 µg/ml of purified recombinant VTN_rs704:C or VTN_rs704:T or equal volumes of control eluate and transferred to a flat-bottom 96-well plate. Cells were then incubated at 37°C for a period of 24

h for hiPSC-RPE, 18 h for porcine RPE cells and 20 min for HUVECs. After incubation, the medium was discarded, and hiPSC-RPE and HUVEC cells were incubated with Hoechst 33342 (1:1000 diluted in DPBS, 100 µl per well) for 10 min at RT. After staining, the cells were washed three times for 5 min each with 100 µl DPBS. Fluorescence images of adherent cells were taken with a Nikon Eclipse microscope. Cell attachment was quantified by measurement of fluorescence intensity (excitation/emission, 360/490 nm) using a Spark multimode microplate reader. Due to the strong pigmentation of porcine RPE, fluorescent staining with Hoechst 33342 was omitted in the test with this cell type. Instead, images from each 96-well plate were taken at 4× magnification with a Nikon Eclipse microscope, and RPE cells were counted using ImageJ.

3.31.2 Adhesion Assay on Vitronectin-containing ECM

Vitronectin-containing ECM was produced by ARPE-19 cells heterologously expressing VTN_rs704:C or VTN_rs704:T as described in 3.26, with one modification: After transfection, 2×10^5 cells (determined with CASY TT Cell Counter) were seeded onto 24-well Transwell filters. Cultivation for 4 weeks including medium changes and final decellularization was performed as described in 3.26.

After decellularization of Transwell filters with 250 µl (upper chamber) and 500 µl (lower chamber) decellularization buffer (see Table 11), filters were washed five times with DPBS (250 µl on the upper chamber and 500 µl on lower chamber). On the decellularized ECM-coated filters, 200 µl of hiPSC-RPE, 250 µl of porcine RPE, or 200 µl of HUVEC cell suspension were seeded. After 40 min (hiPSC-RPE or porcine RPE cells) or 5 min (HUVECs) incubation at 37°C, the culture medium was removed, and cells were incubated with Hoechst 33342 and subsequently washed as described in 3.31.1. Due to the strong pigmentation of porcine RPE, fluorescent staining with Hoechst 33342 was omitted in the test with this cell type. Instead, images from each Transwell filter were taken at 4× magnification with a Nikon Eclipse microscope and cells were counted using ImageJ.

3.32 MTT Assay

The effects of VTN_rs704:C and VTN_rs704:T on cell viability were explored in ARPE-19 and HUVECs subjected to oxidative stress by applying an MTT assay. ARPE-19 cells and HUVECs were passaged from a confluent 10 cm dish or a T25 flask, respectively, at a ratio of 1:24 into a 24-well plate and incubated in the respective culture medium. After 24 h, monolayers of confluent cells were washed once in 1 ml DPBS and incubated with 250 µl of FCS-free culture medium containing 10 µg/ml of purified recombinant VTN_rs704:C or VTN_rs704:T, or equal volumes of control eluate. The cells were then subjected to 0 mM, 1.5 mM, 3 mM, and 5 mM (ARPE-19) or 0 mM, 0.5 mM, 1 mM, and 3 mM (HUVECs) H_2O_2 for 2 h at 37°C. After 2 h, the medium was replaced by 250 µl fresh FCS-free culture medium

containing 10 µg/ml of purified recombinant VTN_rs704:C or VTN_rs704:T, or equal volumes of control eluate. Cells were allowed to recover from H_2O_2-induced stress for 18 h before they were subjected to the MTT assay, a colorimetric assay based on the reduction of the yellow tetrazolium salt MTT (3-(4,5-dimethylthiazol-2-yl)-2,5-diphenyl tetrazolium bromide), to purple formazan crystals by NAD(P)H-dependent oxidoreductase enzymes contained in viable cells [263]. The culture medium was removed, and 1 ml of MTT solution (diluted 1:10 in culture medium) was added to the cells, which were incubated for 30 min at 37°C, until dark blue formazan crystals were visible. After removing the MTT solution, cells were washed in 1 ml DPBS. Finally, 200 µl of 0.1 M HCl in isopropanol was added to each well to dissolve the formazan crystals. After 10 min of gentle agitation, 100 µl of the samples was transferred into flat-bottom 96-well plates and absorbance at 540 nm was measured using a Spark multimode microplate reader.

3.33 Autophagy Assay

The effects of VTN_rs704:C and VTN_rs704:T on cellular autophagy were explored in ARPE-19 and HUVECs by monitoring the expression of the autophagy marker LC3. After induction of autophagy by serum (FCS) depletion and H_2O_2 co-treatment [264,265], analysis of the content of LC3 protein isoforms (forms I and II, respectively cytosolic and autophagosome-bound isoforms) [266] and their ratio was performed by western blot as previously reported [267].

3.33.1 Autophagy Assay with ARPE-19 Cells

ARPE-19 cells were passaged from a 10 cm confluent dish at a ratio of 1:10 into a 12-well plate and incubated overnight in 1 ml culture medium. After washing once with 1 ml pre-warmed DPBS, cells were pre-incubated for 1 h with 1.0 µg/ml VTN_rs704:C, VTN_rs704:T or equal volumes of control eluate in 1 ml of FCS-free culture medium. Cells were then treated for 2 h with 1 mM H_2O_2 in 1 ml fresh FCS-free medium containing 1.0 µg/ml of purified recombinant VTN_rs704:C or VTN_rs704:T, or equal volumes of control eluate. After stress induction, cells were scraped into their medium and the cell suspension was centrifuged (5 min, 4500 rpm, 4°C; Eppendorf 5415R centrifuge). After removal of the supernatant, the cells were washed with 1 ml DPBS and centrifuged again as before. The cell pellet was finally resuspended in 120 µl DPBS for SDS-PAGE (3.11.1) and western blot analysis (see 3.12) with antibodies against LC3 and ACTB.

3.33.2 Autophagy Assay with HUVEC Cells

HUVECs were subjected to the autophagy assay following the procedure described above for ARPE-19 cells, with minor modifications. After being pre-incubated for 1 h with 1.5 µg/ml of purified recombinant VTN_rs704:C or VTN_rs704:T, or an equal volume of control eluate, cells were stressed with 1 mM H_2O_2 for 24 h. Cells were then harvested and washed as

described in the section above, and finally resuspended in 100 ul DPBS for SDS-PAGE (3.11.1) and western blot analysis (see 3.12) with antibodies against LC3 and ACTB.

3.34 Phospho-ERK Assay

The effect of VTN_rs704:C and VTN_rs704:T on the activation of extracellular signal-regulated kinase (ERK) signalling was studied in ARPE-19 cells and HUVECs by following ERK1/2 phosphorylation *via* western blot analysis.

3.34.1 Phospho-ERK Assay in ARPE-19 Cells

The phospho-ERK assay was performed with ARPE-19 cells passaged from a 10 cm confluent dish at a ratio of 1:10 into a 12-well plate and incubated overnight in 1 ml culture medium. After washing once with 1 ml pre-warmed DPBS, cells were incubated with 0.5 µg/ml of purified recombinant VTN_rs704:C, VTN_rs704:T, or equal volumes of control eluate in 1 ml of FCS-free culture medium. After 2 h of incubation, cells were scraped into their medium and the cell suspension was centrifuged (5 min, 4500 rpm, 4°C; Eppendorf 5415R centrifuge). After removal of the supernatant, the cells were washed with 300 µl DPBS and centrifuged again as before. The cell pellet was finally resuspended in 120 µl DPBS for SDS-PAGE (3.11.1) and western blot analysis (see 3.12) with antibodies against ERK1/2, phospho-ERK1/2 and ACTB.

3.34.2 Phospho-ERK Assay in HUVEC Cells

To follow vitronectin-dependent phosphorylation of ERK1/2 in HUVECs, cells were incubated for 24 h with 1.5 µg/ml of purified recombinant VTN_rs704:C, VTN_rs704:T, or equal volumes of control eluate. After 24 h of incubation, cells were scraped into their medium and the cell suspension was centrifuged (5 min, 4500 rpm, 4°C; Eppendorf 5415R centrifuge). After removal of the supernatant, the cells were washed with 300 µl DPBS and centrifuged again as before. The cell pellet was finally resuspended in 100 µl DPBS for SDS-PAGE (3.11.1) and western blot analysis (see 3.12) with antibodies against ERK1/2, phospho-ERK1/2 and ACTB.

4. Results

4.1 Endogenous Vitronectin Expression in Retinal and Non-retinal Cell Lines

The expression of endogenous vitronectin was analysed in retinal and non-retinal cell lines often used as cellular model systems in *in vitro* analyses of the molecular pathomechanisms of common retinal disorders such as AMD [268-270]. Cell lines included ARPE-19, hiPSC-RPE, Y79, WERI-Rb1, HUVECs, and HEK293-EBNA. Endogenous vitronectin mRNA expression was observed in the two retinoblastoma-derived cell lines Y79 and WERI-Rb1 and, to a weaker extent, in the RPE cell lines ARPE-19 and hiPSC-RPE. No mRNA expression was detected in HEK293-EBNA and HUVEC cells (**Figure 8A**). Western blot analysis failed to detect vitronectin protein in any of the cell lines tested, even after multiple attempts to increase sensitivity (**Figure 8B**).
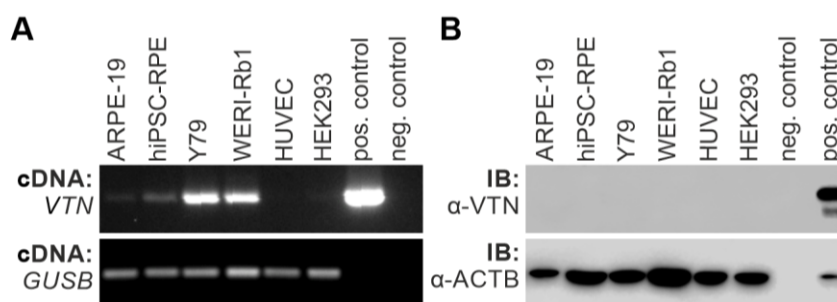
Figure 8: Endogenous *VTN* expression in retinal and non-retinal cell lines.
(**A**) RT-PCR analysis to investigate *VTN* mRNA expression in ARPE-19, hiPSC–RPE, Y79, WERI-Rb1, HUVEC, and HEK293-EBNA cells. Expression vectors containing cDNA for *VTN*_rs704:C served as positive control; no template was added to the negative control. *GUSB* gene expression was assessed as control for RNA integrity. (**B**) Immunoblot (IB) analysis addressing vitronectin protein expression in ARPE-19, hiPSC–RPE, Y79, WERI-Rb1, HUVEC, and HEK293-EBNA cells. HEK293-EBNA cells transfected with expression vectors for VTN_rs704:C served as positive control; no cells were added to the negative control. Cell lysates were subjected to IB analyses using antibodies against vitronectin and ACTB (loading control). (Figure modified from Biasella et al., 2020 [246]).

4.2 Influence of Genetic Variant rs704 on Vitronectin Expression

4.2.1 Comparison of mRNA Expression for *VTN* Variants

An effect of rs704 on *VTN* transcription was studied in hiPSC-RPE cells and neural retinal samples from different donors which were heterozygous for rs704 (**Figure 9A**). After RNA isolation and cDNA synthesis, a semi-quantitative sequencing approach was performed to study differences in the mRNA expression of *VTN*_rs704:C and *VTN*_rs704:T alleles. Prior to the analysis, the sensitivity of the method was determined. Specifically, a dilution series was performed with a mixture of different concentrations of recombinant *VTN* cDNA variants (pcDNA3.1_VTN_rs704:C and pcDNA3.1_VTN_rs704:T). Differences in *VTN*_rs704:C and *VTN*_rs704:T concentrations are reflected in the sequence chromatogram by differences in peak hight (**Figure 9B**). Electropherogram peaks were similar for heterozygous DNA samples of hiPSC-RPE cells and neural retinal tissues at the T and C allele position (**Figure

9A, **C**). This suggests similar levels of *VTN*_rs704:C and *VTN*_rs704:T transcripts in the heterozygous samples and thus no significant effect of rs704 on vitronectin mRNA expression.
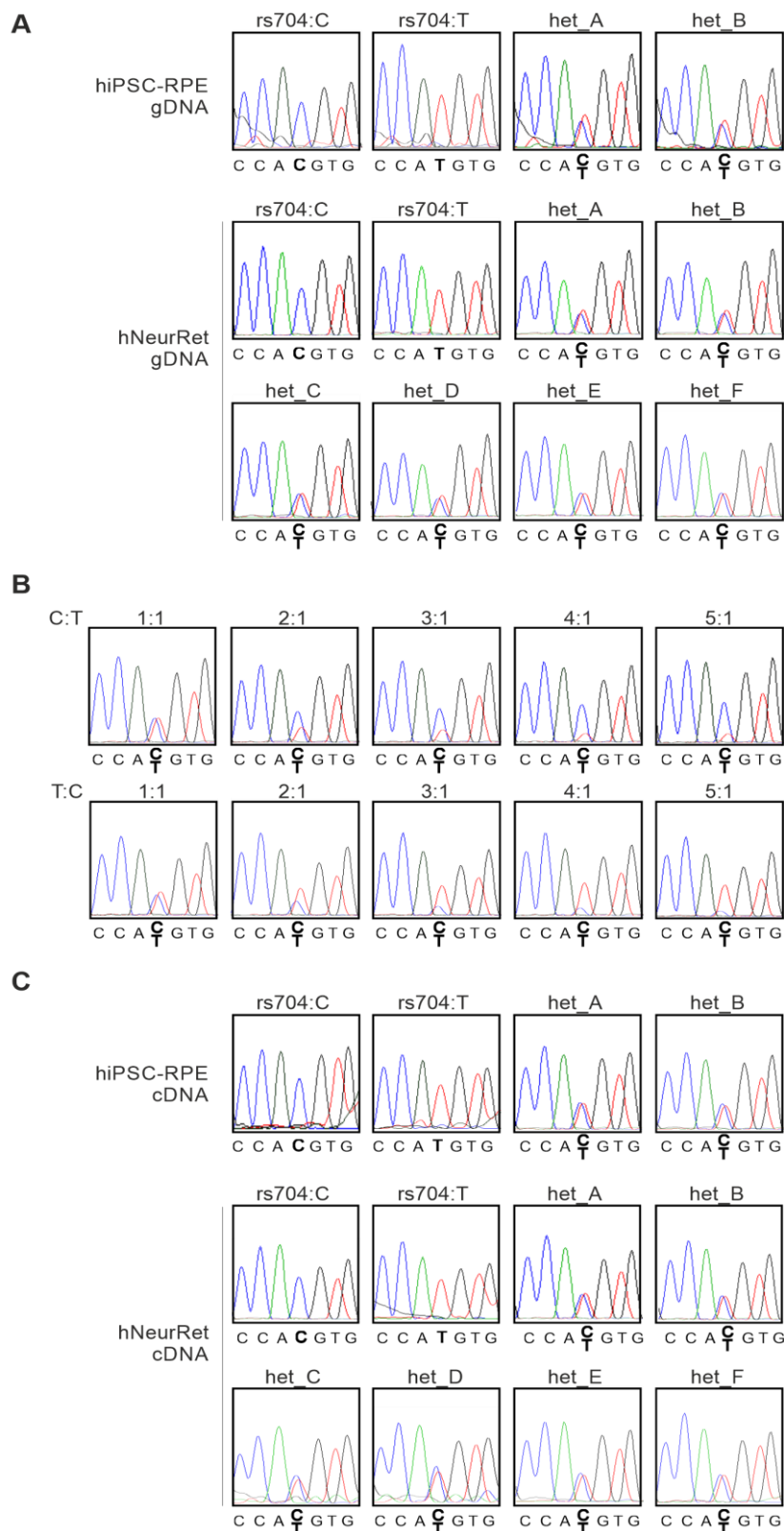
Figure 9: Effect of rs704 on *VTN* mRNA expression.
(**A**) DNA sequence chromatograms obtained from amplification of the *VTN* region harbouring rs704 from genomic DNA (gDNA) of hiPSC-RPE cells and human neural retinal samples (hNeurRet). (**B**) Titration series with recombinant *VTN* cDNA variants derived from the non-risk (rs704:C) or the risk (rs704:T) haplotype (ratio of C:T allele given in the figure). (**C**) Expression analysis of endogenous *VTN* cDNA variants VTN_rs704:C and VTN_rs704:T in hiPSC–RPE cells or human retinal tissues (hNeurRet) of different donors by semi-quantitative sequencing. (Figure modified from Biasella et al., 2020 [246]).

4.2.2 Comparison of Protein Expression and Processing for Vitronectin Isoforms

The impact of rs704 on vitronectin protein expression was analysed *via* heterologous expression of VTN_rs704:C and VTN_rs704:T. To that end, HEK293-EBNA and ARPE-19 cells were transfected with expression constructs for VTN_rs704:C and VTN_rs704:T, or with an empty control expression vector. As a control, co-transfection with the expression vector for GFP monitored comparable transfection efficiency for the different conditions tested. After 48 and 72 h, culture medium and cell lysates were collected and expression of the two heterologously expressed vitronectin isoforms was compared by western blot analysis. After densitometric quantification a significant increase in the amount of cellular VTN_rs704:T compared to VTN_rs704:C (48 h, 3.99 ± 2.88-fold increase; 72 h, 5.66 ± 1.91-fold increase; p < 0.05 for both time points) was observed. An increase in the amount of VTN_rs704:T compared to VTN_rs704:C was also observed in the culture medium of the cells (48 h, 3.03 ± 2.52-fold increase; 72 h, 3.47 ± 2.05-fold increase; p < 0.05 for both time points; **Figure 10A)**. Similarly, densitometric quantification also revealed a statistically significant increase in the amount of VTN_rs704:T compared to VTN_rs704:C in transfected ARPE-19 cells (48 h, 4.19 ± 2.20-increase; 72 h, 5.60 ± 3.83-increase; p < 0.05 for both time points), as well as increased secretion of VTN_rs704:T compared to VTN_rs704:C into the cultivation medium (48 h, 4.17 ± 2.16-increase, p < 0.05; 72 h, 1.55 ± 1.36-increase, p > 0.05) (**Figure 10B**). VTN_rs704:T secreted from both cell types appeared mainly as a single-chain form of 75 kDa (indicated by the black arrowhead in **Figure 10A, B**). In contrast, secreted VTN_rs704:C appeared as a mixture of the cleaved form (65 kDa, white arrowhead in **Figure 10A, B**) and the uncleaved single-chain form (75 kDa, black arrowhead in **Figure 10A, B**).
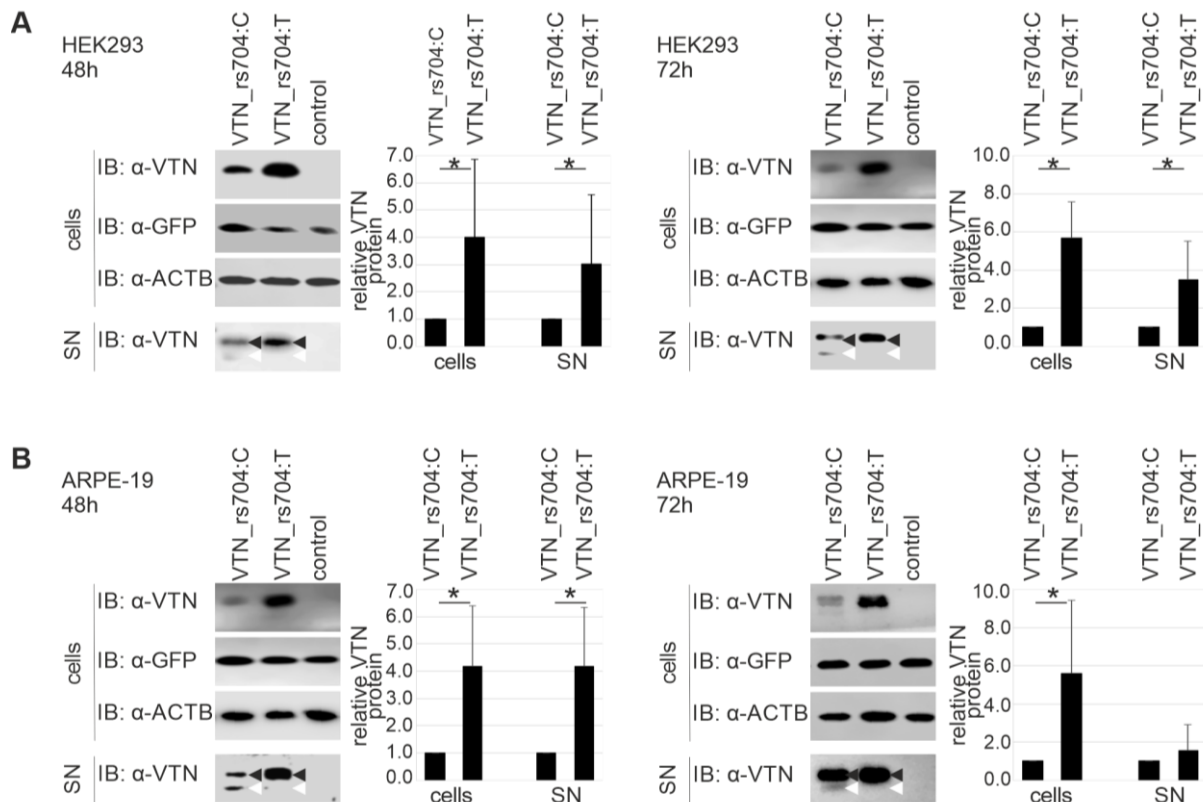
Figure 10: Effect of rs704 on vitronectin protein expression and processing.
(**A**) HEK293-EBNA and (**B**) ARPE-19 cells were transfected with expression vectors for VTN_rs704:C or VTN_rs704:T, or with an empty expression vector (control). Co-transfection with a GFP expression vector was performed as a transfection control. Forty-eight and 72 h after transfection, cell lysate and culture medium (supernatant, SN) of transfected cells were subjected to immunoblot (IB) analysis with antibodies against vitronectin (α-VTN) and GFP (α-GFP). The ACTB immunoblot served as loading control. The black and white arrowheads represent vitronectin in its full-chain (uncleaved) and cleaved form, respectively. After densitometric quantification, vitronectin signals were normalized against GFP. Data represent the mean ± SD of four biological replicates, calibrated against VTN_rs704:C. Asterisks (*) indicate statistically significant differences (p < 0.05, Mann-Whitney U test). (Figure modified from Biasella et al., 2020 [246]).

4.3   Effect of rs704 on the Endogenous Proteolytic Cleavage of Vitronectin

In vivo, vitronectin is mainly processed by two proteases cleaving at two closely adjacent cleavage sites, and thus both resulting in cleavage products of similar molecular weight (63 and 65 kDa, as well as 12 and 10 kDa). The furin protease cleaves at the carboxyl-terminal side of R398 and was already reported to be affected by the rs704-associated amino acid exchange in aa 400 [204,237]. The plasmin protease cleaves at the carboxyl-terminal side of R380 [257]. To assess the effect of furin and plasmin proteases on heterologously expressed VTN_rs704:C and VTN_rs704:T in HEK293-EBNA (**Figure 7**; **Figure 10**), the processing of heterologously expressed vitronectin was compared with and without inhibition of the plasmin protease. To inhibit plasmin cleavage, HEK293-EBNA cells were co-transfected with expression vectors for PAI-1, a known inhibitor of plasmin formation [257]. In western blot analyses of cell lysates and culture media from cells heterologously expressing VTN_rs704:C and VTN_rs704:T but not PAI-1, both vitronectin isoforms appeared as a mixture of the uncleaved, 75 kDa, species and the cleaved species (differentiation between

the 65 and 63 kDa vitronectin species not feasible in western blot) (**Figure 11A**). Again, VTN_rs704:T showed less susceptibility to endoproteolytic cleavage than VTN_rs704:C. In the presence of heterologously co-expressed PAI-1, no cleaved species were detected for VTN_rs704:T, whereas VTN_rs704:C was cleaved as usual. This suggests that the rs704-induced exchange of aa from T400 to M400 interferes with furin cleavage and that the clipped product relative to the VTN_rs704:T isoform observed in experiments in which plasmin was not inhibited (without co-transfection of PAI-1) results rather from plasmin cleavage on the carboxy-terminal side of R380 thus representing a 63 kDa isoform (**Figure 11A**).

4.4   Effect of rs704 on Vitronectin Multimerization

Purified isoforms VTN_rs704:C and VTN_rs704:T were subjected to non-reducing SDS-PAGE (**Figure 11B**) and Blue Native PAGE (**Figure 11C**) to follow vitronectin self-aggregation into higher-order multimers (reported up to 16-mer) [205], stabilized by disulphide bonds or non-covalent interactions, respectively. Non-reducing SDS-PAGE revealed species of approximately 75 kDa for both vitronectin isoforms corresponding to the respective monomeric forms, as well as higher molecular weights species from 150 kDa up to > 300 kDa, representing disulphide bond-stabilized vitronectin multimers (**Figure 11B,** representative of three independent experiments). Blue Native PAGE showed high molecular weight species in the range of 300-1050 kDa (**Figure 11C,** representative of three independent experiments). In both approaches, VTN_rs704:C and VTN_rs704:T showed comparable multimerization patterns and thus no effect of rs704 on vitronectin self-aggregation.
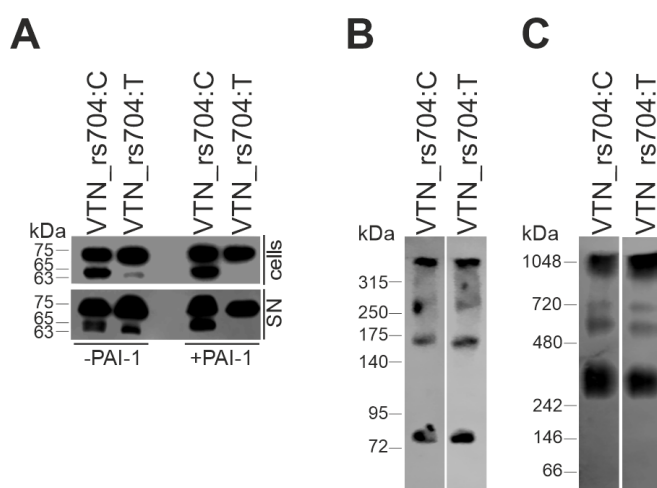
Figure 11: Effect of rs704 on proteolytic cleavage and multimerization of vitronectin.
(**A**) HEK293-EBNA cells were transfected with expression vectors for VTN_rs704:C or VTN_rs704:T in combination with an empty (control) expression vector (-PAI-1) or with a PAI-1 expression vector (+PAI-1). After 48 h, transfected cells, and their culture medium (supernatant, SN) were subjected to western blot analysis with antibodies against vitronectin. (**B**) Non-reducing SDS-PAGE and (**C**) BN-PAGE with recombinant vitronectin isoforms, followed by western blot analysis with antibodies against vitronectin. (Figures B and C were modified from Biasella et al., 2020 [246]).

4.5   Effect of rs704 on Vitronectin Stability

Differences between VTN_rs704:C and VTN_rs704:T in thermodynamic stability were assessed by the partial proteolysis assay, which monitors susceptibility of proteins to trypsin-mediated digestion after partial thermal denaturation. For thermal protein denaturation, the two purified vitronectin isoforms VTN_rs704:C and VTN_rs704:T were pre-incubated for 10 min at 37°C or 42°C. Proteolysis was performed by subsequent incubation with TPCK-trypsin for 5 min. Digestion was followed by western blot analysis with antibodies against vitronectin. Untreated purified vitronectin isoforms exhibited the characteristic migration pattern described in section 4.2.2 and 4.3, with a major molecular weight species of approximately 65 kDa for VTN_rs704:C (predominantly present in the cleaved form) and a 75 kDa for VTN_rs704:T (predominantly present in the uncleaved form) (**Figure 12A**). Incubation with TPCK-trypsin resulted in rapid digestion of both vitronectin isoforms, visible by the strong decrease of the 75 and 65 kDa species and an increase in cleavage products with molecular weights between 40 and 55 kDa (**Figure 12A**). Similar results were obtained when the proteins were first denatured at 37 or 42°C for 10 min and then incubated with TPCK-trypsin, hence the partial thermal denaturation did not seem to strongly influence the accessibility of both vitronectin isoforms to trypsin (**Figure 12**). This was also evident after densitometric quantification of three independent experiments (**Figure 12B, C**): The levels of undigested vitronectin species was reduced to about one fifth by trypsin treatment (**Figure 12B**), while the levels of digestion products with a molecular weight between 40 and 55 kDa, appearing only in trypsin-treated samples, was not affected by thermal pre-treatment (**Figure 12C**). Notably, the amount of 40-55 kDa digestion products from VTN_rs704:C appeared slightly higher than that of VTN_rs704:T in all three trypsin-mediated digestion assays (**Figure 12C**), however, this trend was not statistically significant.
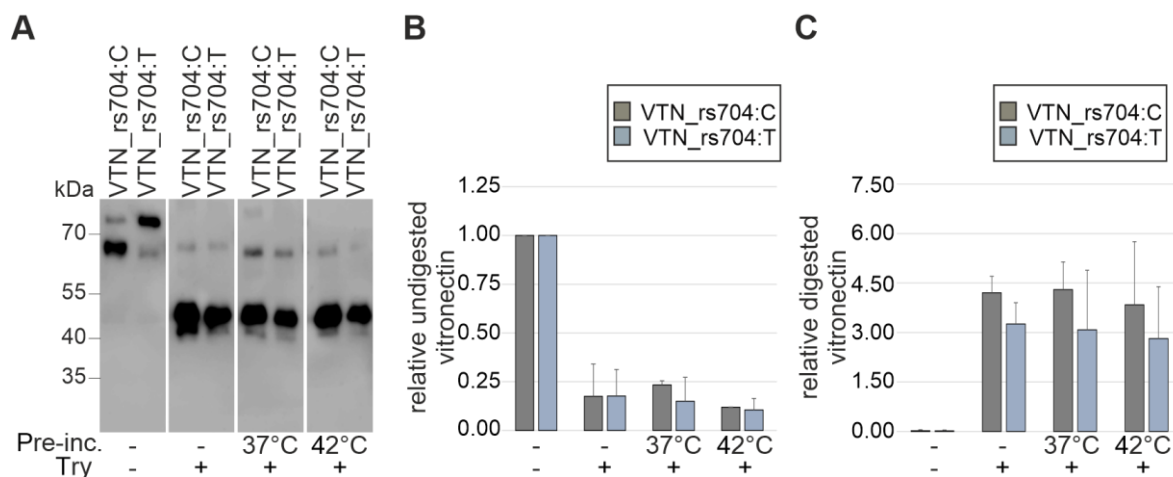
Figure 12: Effect of rs704 on vitronectin stability.
Purified recombinant VTN_rs704:C and VTN_rs704:T, untreated or previously pre-incubated at 37 and 42°C, were subjected to proteolysis with TPCK-trypsin (Try) at 37°C for 5 min. (**A**) Samples were subjected to immunoblot analysis with antibody against vitronectin. After densitometry, the signals from (**B**) relative levels of undigested vitronectin and (**C**) relative levels of digestions products (of size between 40 and 55 kDa) from vitronectin isoforms were calibrated against signals from the respective untreated vitronectin isoform (undigested, full-length). Data represent the mean ± SD of three biological replicates.

4.6 Effect of rs704 on the Capacity of Vitronectin to Bind Retinal and Endothelial Cell Lines

The two vitronectin isoforms VTN_rs704:C and VTN_rs704:T were compared in their ability to bind the retinal cell lines ARPE-19, hiPSC-RPE, porcine RPE, Y79 and the endothelial cell line HUVEC. Cells were incubated in medium containing the heterologously expressed vitronectin isoforms VTN_rs704:C and VTN_rs704:T, or in vitronectin-free control medium for 1 h at 37°C. After repeated washing steps, cells were lysed and subjected to western blot analysis with antibodies against vitronectin and ACTB (loading control). It was observed that VTN_rs704:C and VTN_rs704:T both bound to all cell lines tested. However, compared to VTN_rs704:C, VTN_rs704:T showed a statistically significantly decreased binding to all cell lines (densitometric quantification of four to six independent experiments revealed a reduction of VTN_rs704:T binding to 21. 3% ± 19.4% in ARPE-19, to 34.8% ± 37.0% in hiPSC-RPE, to 10.2% ± 6.7% in porcine RPE, to 27.9% ± 19.2% in HUVEC, and to 37.1% ± 30.3% for Y79 cells, compared to VTN_rs704:C (p < 0.05 for all cell lines; **Figure 13**).
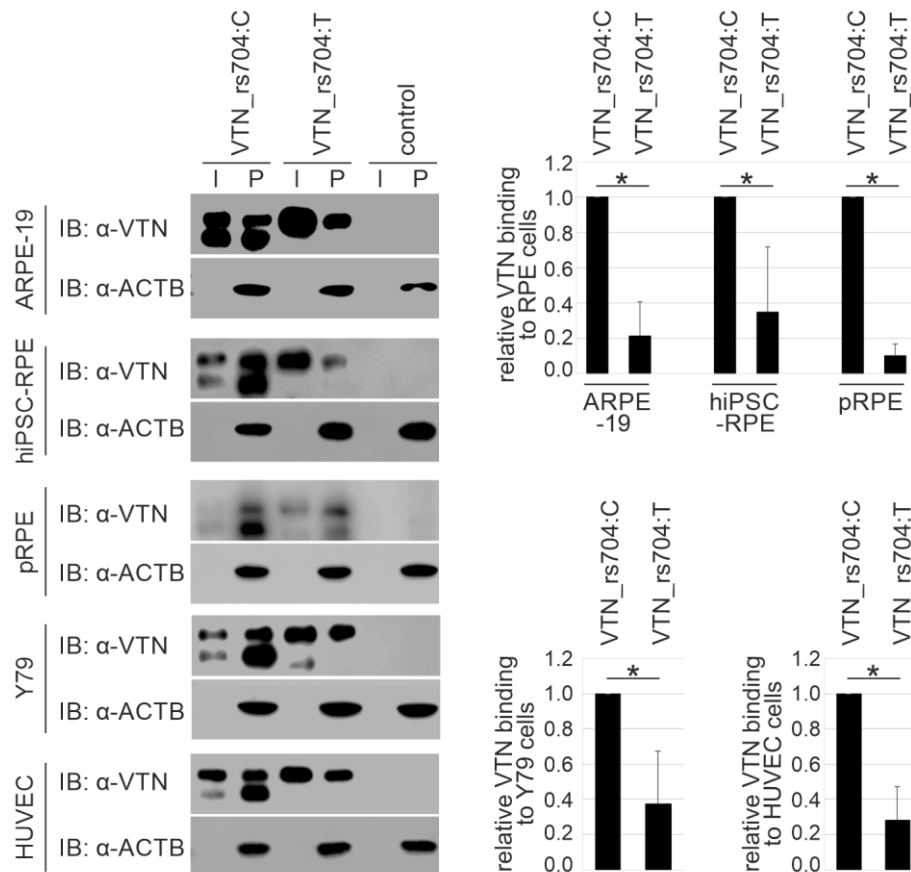
Figure 13: Effect of rs704 on vitronectin binding to retinal and endothelial cells.
ARPE-19, hiPSC-RPE, porcine RPE, Y79 and HUVECs were incubated with vitronectin-containing input (I, culture medium of HEK293-EBNA cells transfected with expression vectors for VTN_rs704:C and VTN_rs704:T, adjusted for vitronectin concentrations) or control input. After washing, cell pellets (P) were subjected to western blot analysis with antibodies against vitronectin (α-VTN) and ACTB (α-ACTB), as loading control. After densitometric quantification, vitronectin signals were normalized against ACTB and vitronectin in the input. Data represent the mean ± SD of four (hiPSC–RPE and pRPE), five (ARPE-19 and HUVECs), or six (Y79) biological replicates, calibrated against VTN_rs704:C. Asterisks (*) indicate statistically significant differences (p < 0.05, Mann-Whitney U test). (Figure modified from Biasella et al., 2020 [246]).

4.7 Role of VTN_rs704:C and VTN_rs704:T in AMD-associated RPE Cellular Processes

The following analyses aimed to compare the effect of the two vitronectin isoforms VTN_rs704:C and VTN_rs704:T on AMD-associated cellular processes, specifically cell adhesion, autophagy, viability, and activation of ERK signalling [209,234,271,272] in cultured RPE cells.

4.7.1 Influence of VTN_rs704:C and VTN_rs704:T on RPE Cell Adhesion

The role of VTN_rs704:C and VTN_rs704:T on RPE cell adhesion was assessed in hiPSC-RPE and porcine RPE cells.

First, adhesion of resuspended cells on the cell culture well in the presence of purified recombinant VTN_rs704:C, VTN_rs704:T or control eluate was compared. hiPSC-RPE cells were incubated for 24 h with recombinant vitronectin isoforms or control eluate, followed by

fluorescent labelling and intensive washing. Next, the fluorescence emitted by cells attached to the culture well was measured (**Figure 14A**). A quantification of seven independent experiments revealed an increase in the fluorescence signal to 4.24 ± 0.99 after treatment with VTN_rs704:C and to 3.78 ± 0.86 after treatment with VTN_rs704:T compared to control ($p < 0.05$ between vitronectin-treated samples and control, **Figure 14A**). The adhesion of porcine RPE cells was assessed after 18 h of treatment with recombinant vitronectin isoforms or control eluate. Due to the strong pigmentation of primary porcine RPE cells, fluorescence labelling of these cells was not feasible. Instead, cell adhesion was assessed by taking microscopic images and counting cells adhered to the culture plate after intensive washing steps. Again, the presence of the two recombinant vitronectin isoforms increased cell adhesion of porcine RPE cells compared to control treatment (a quantification of four independent replicates revealed an increase in the relative number of adherent cells to 1.92 ± 0.53 with VTN_rs704:C and to 1.96 ± 0.83 with VTN_rs704:T compared to control treatment; $p < 0.05$ between vitronectin-treated and control samples, **Figure 14B**).

The adhesion of hiPSC-RPE and porcine RPE cells was also assessed onto ECM containing recombinant VTN_rs704:C or VTN_rs704:T, as well as onto vitronectin-free control ECM (produced from ARPE-19 cells transfected with expression vectors for VTN_rs704:C or VTN_rs704:T or with an empty expression vector, respectively). Cell suspensions were added onto ECM-containing filters for 40 min at 37°C, followed by several washing steps. Adherent hiPSC-RPE cells (again fluorescently labelled) and porcine RPE cells were counted from microscopic photographs. Quantification of four or five independent experiments, respectively, showed that the presence of both vitronectin isoforms in the matrices facilitated cell adhesion in hiPSC-RPE cells (1.79 ± 0.41 with VTN_rs704:C and 1.84 ± 0.25 with VTN_rs704:T compared to control; $p < 0.05$ between control ECM and ECM containing vitronectin, **Figure 14C)** as well as in porcine RPE cells (2.92 ± 1.71 with VTN_rs704:C and 1.73 ± 0.42 with VTN_rs704:T compared to control; $p < 0.05$ between VTN_rs704:C-containing ECM and control, **Figure 14D**). However, the analyses showed no differences in the effect of VTN_rs704:C and VTN_rs704:T.
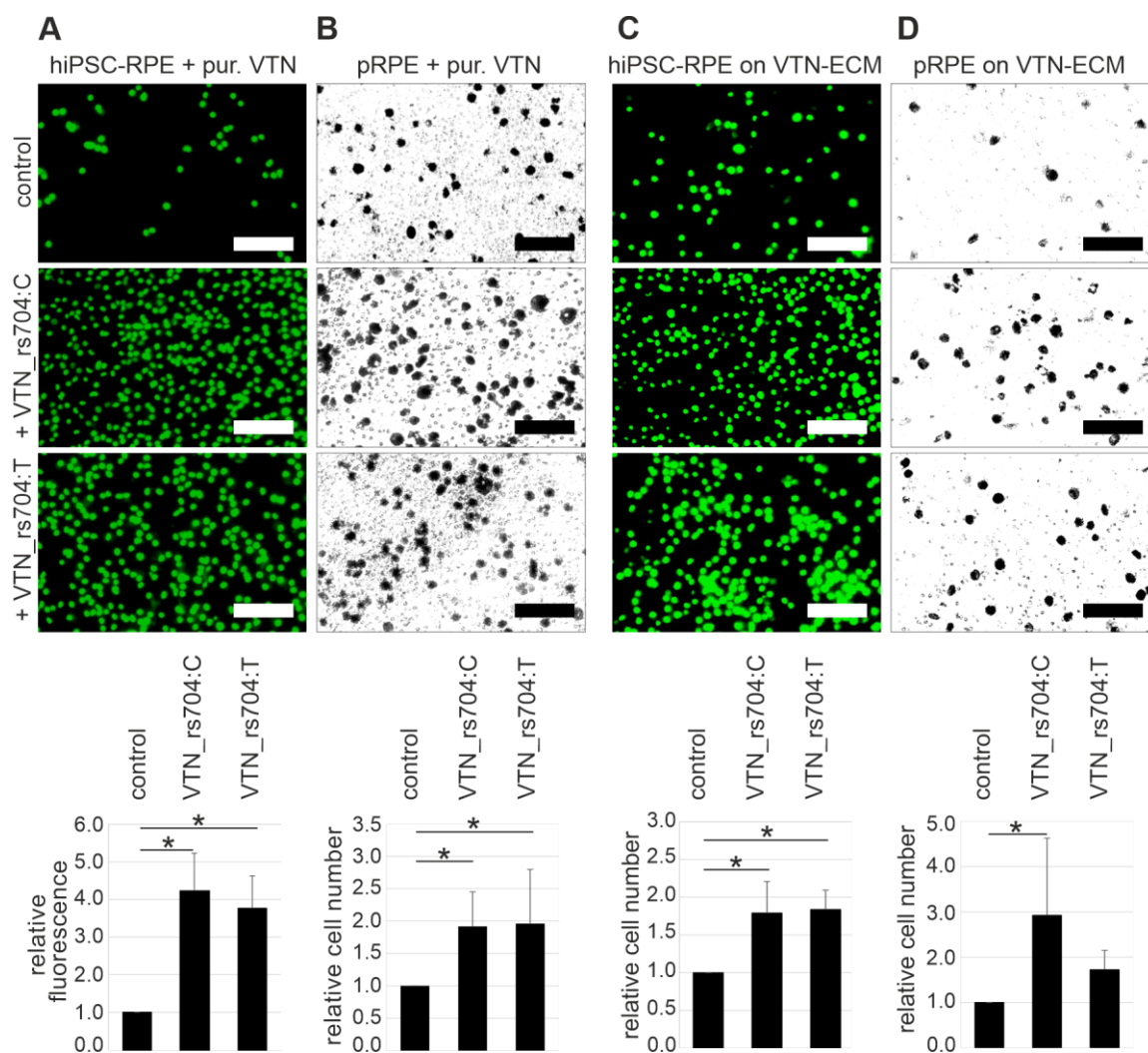
Figure 14: Effect of VTN_rs704:C and VTN_rs704:T on RPE cell adhesion.
(**A**) hiPSC-RPE and (**B**) freshly isolated porcine RPE (pRPE) cell suspension were incubated for 24 h and 18 h, respectively, in the presence of purified recombinant VTN_rs704:C, VTN_rs704:T, or control eluate. Subsequently, cell adhesion was determined measuring fluorescence of fluorescently labelled cells in a spectrophotometer (**A**) or counting cells from 4× micrographs (**B**) using ImageJ. (**C**) hiPSC–RPE cells and (**D**) freshly isolated pRPE were incubated for 40 min on VTN_rs704:C- or VTN_rs704:T-containing ECM or on control ECM. Subsequently, adherent cells were determined by counting cells from 4× micrographs with ImageJ. Data represent mean ± SD of seven (**A**), four (**B, D**), or five (**C**) independent replicates, calibrated against the control. Asterisks (*) indicate statistically significant differences ($p < 0.05$, Kruskal-Wallis test, followed by Dunn's multiple comparison test and Bonferroni correction). Micrographs shown in the figure were taken at 10× magnification (standard, 200 µm). (Figure modified from Biasella et al., 2020 [246]).

4.7.2 Influence of VTN_rs704:C and VTN_rs704:T on RPE Cell Autophagy

An effect of VTN_rs704:C and VTN_rs704:T on cell autophagy was examined in ARPE-19 cells. To induce cell autophagy, cells were treated with purified recombinant VTN_rs704:C, VTN_rs704:T or control eluate, with or without exposure to 1 mM H_2O_2 for 2 h. After 2 h, cells were lysed, and subjected to western blot analysis against autophagy marker LC3, following the ratio of its isoforms LC3-I (decreasing with autophagy induction) and LC3-II (increasing with autophagy induction) [266]. Densitometric quantification of four independent experiments revealed a significant decrease in the LC3-I/LC3-II ratio in cells subjected to H_2O_2 compared to cells without H_2O_2 treatment ($p < 0.05$ between H_2O_2-treated samples compared to

untreated samples), demonstrating successful induction of autophagy in H_2O_2 treated cells (**Figure 15**). However, the two vitronectin isoform revealed a similar LC3-I/LC3-II ratio, in H_2O_2-treated samples as well as in controls (H_2O_2-free) (**Figure 15**).
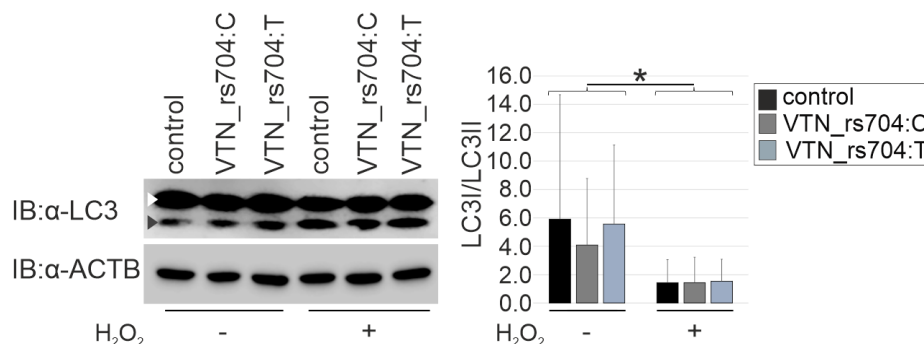
Figure 15: Effect of VTN_rs704:C and VTN_rs704:T on RPE autophagy.
ARPE-19 cells were pre-incubated for 1 h with purified recombinant VTN_rs704:C, VTN_rs704:T or control eluate. Subsequently, cells were exposed for 2 h to 1mM H_2O_2 (+H_2O_2) or treated under the same conditions but without H_2O_2 (-H_2O_2), in the presence of fresh purified recombinant proteins. Cells were subjected to western blot analysis with antibodies against LC3 (α-LC3) and ACTB (α-ACTB) as loading control. After densitometric quantification, LC3I signals (white arrowhead) were normalised against the respective LC3II signals (black arrowhead). Data represent the mean ± SD of four biological replicates. Asterisks (*) indicate statistically significant differences (p < 0.05, Mann-Whitney U test).

4.7.3   Influence of VTN_rs704:C and VTN_rs704:T on RPE Cell Viability

Cell death of RPE cells particularly in response to oxidative stress is a characteristic pathological sign in AMD [234,273,274]. A putative role for VTN_rs704:C and VTN_rs704:T in RPE cell viability was assessed in ARPE-19 cells subjected to different levels of oxidative stress. To induce oxidative stress, ARPE-19 were exposed to 0, 1.5, 3, and 5 mM of H_2O_2 for 2 h at 37°C, in the presence of purified VTN_rs704:C, VTN_rs704:T or control eluate. After a period of 18 h allowing the cells to recover in the presence of VTN_rs704:C, VTN_rs704:T or control eluate, cells were subjected to the MTT assay, measuring the activity of NAD(P)H-dependent oxidoreductase enzymes as a marker for cell viability. Quantification of six independent experiments showed a reduction in oxidoreductase activity and thus viability of ARPE-19 cells with increasing concentrations of H_2O_2 (**Figure 16**). No effect of VTN_rs704:C and VTN_rs704:T in comparison to control eluate treatment was observed for all oxidative stress conditions tested (**Figure 16**).

Figure 16: Effect of VTN_rs704:C and VTN_rs704:T on RPE cell viability.
ARPE-19 cells were exposed for 2 h to 0, 1.5, 3 and 5 mM H_2O_2 in the presence of purified recombinant VTN_rs704:C, VTN_rs704:T or control eluate. After a period of 18 h allowing the cells to recover in the presence of purified recombinant VTN_rs704:C, VTN_rs704:T or control eluate, cells were subjected to the MTT assay. Data represent the mean ± SD of six biological replicates calibrated against control at 0 mM H_2O_2.

4.7.4 Influence of VTN_rs704:C and VTN_rs704:T on ERK Signalling in RPE cells

To analyse effects of VTN_rs704:C and VTN_rs704:T on ERK signalling in RPE cells, ARPE-19 cells were incubated with VTN_rs704:C, VTN_rs704:T or control eluate for 2 h at 37 °C. Subsequently, cells were harvested, and subjected to western blot analysis following phosphorylation and thus activation of the ERK signalling marker ERK1/2 [275,276]. Compared to control, cells treated with the two vitronectin isoforms depicted a down-regulation of phosphorylated ERK1/2 (**Figure 17**), specifically, densitometric quantification of three independent experiments revealed a reduction to 27.0% ± 14.3% with VTN_rs704:C and to 52.3% ± 32.1% with VTN_rs704:T, compared to control eluate; $p < 0.05$ between VTN_rs704:C-treated cells and control; **Figure 17**).
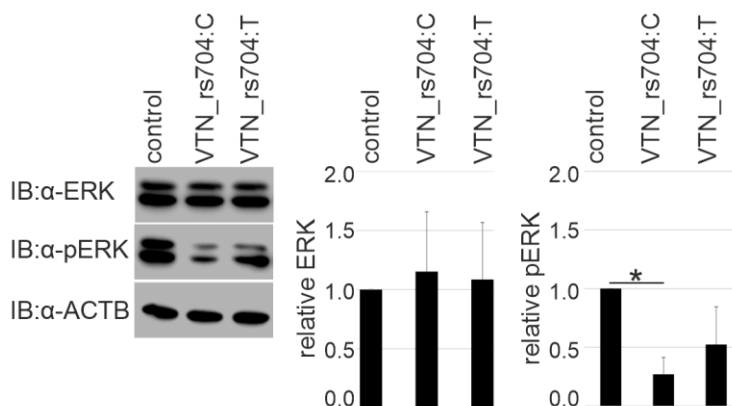
Figure 17: Effect of VTN_rs704:C and VTN_rs704:T on ERK1/2 activation in RPE cells.
ARPE-19 cells were treated with purified recombinant VTN_rs704:C, VTN_rs704:T or control eluate. After 2h, cells were subjected to western blot analysis with antibodies against ERK1/2 (α-ERK), phosphorylated ERK1/2 (α-pERK) and ACTB (α-ACTB), as loading control. After densitometric quantification, ERK1/2 and phosphorylated ERK1/2 (pERK) signals were normalised against ACTB. Data represent the mean ± SD of three biological replicates calibrated against the control. Asterisks (*) indicate statistically significant differences ($p < 0.05$, Kruskal-Wallis test, followed by Dunn's multiple comparison test and Bonferroni correction).

4.8 Influence of VTN_rs704:C and VTN_rs704:T in AMD-associated Endothelial Cellular Processes

Aberrant angiogenesis is a hallmark of NV, one of the two late-stage forms of AMD [211]. The following analyses aimed to investigate an effect of VTN_rs704:C and VTN_rs704:T on cellular processes closely related to angiogenesis, i.e. endothelial cell adhesion, autophagy, viability, ERK-signalling, migration and tubulogenesis [277-279].

4.8.1 Influence of VTN_rs704:C and VTN_rs704:T on Endothelial Cell Adhesion

The effect of VTN_rs704:C and VTN_rs704:T on endothelial cell adhesion was studied in HUVEC cells following their adherence to the culture flask after incubation with purified recombinant VTN_rs704:C, VTN_rs704:T, or control eluate for 20 min at 37 °C. After incubation, cells were fluorescently labelled, and repeatedly washed to remove non-adherent cells. Subsequently, the fluorescence emitted by cells attached to the culture vessel was measured photometrically (**Figure 18A**). A quantification of five independent experiments revealed that both vitronectin isoforms slightly decreased fluorescence (and thus cellular adhesion) to 0.90 ± 0.05 for VTN_rs704: C and 0.83 ± 0.09 for VTN_rs704: T ($p < 0.05$ between VTN_rs704: T and control, **Figure 18A**) with no statistical difference between the two isoforms.

In an alternative approach, HUVECs were seeded onto vitronectin-containing or vitronectin-free ECM produced by ARPE-19 cells (see 3.31.2) and incubated for 5 min at 37 °C. Cells were then fluorescently labelled and repeatedly washed. After taking microscopic photographs, cells adhering to the ECM were counted. Quantification of five independent experiments revealed that the number of adherent cells increased with the presence of vitronectin in the matrices (increase to 1.52 ± 0.36 with VTN_rs704:C and to 1.59 ± 0.56 with VTN_rs704:T compared to control; $p < 0.05$ between control and VTN_rs704:C- or VTN_rs704:T-containing ECM , **Figure 18B**), again with no statistical difference between the two isoforms.
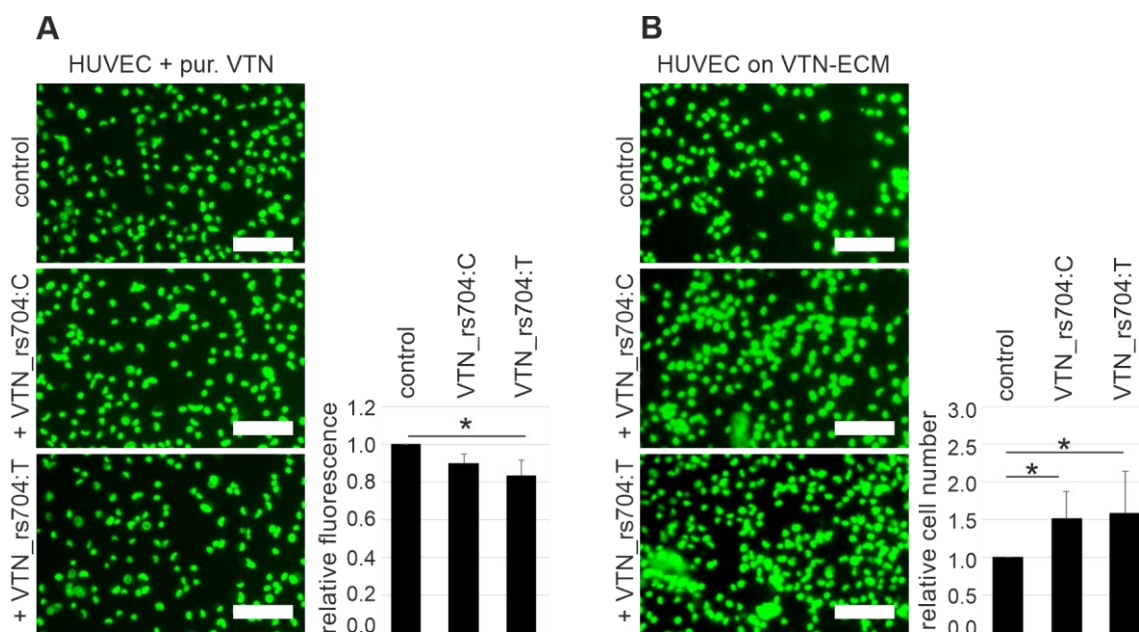
Figure 18: Effect of VTN_rs704:C and VTN_rs704:T on endothelial cell adhesion.
(**A**) HUVECs were incubated for 20 min with purified recombinant VTN_rs704:C, VTN_rs704:T, or control eluate. Subsequently, cell adhesion was determined measuring fluorescence of fluorescently labelled cells in a spectrophotometer. (**B**) HUVECs were incubated for 5 min on VTN_rs704:C- or VTN_rs704:T-containing ECM, or on control ECM. Subsequently, adherent cells were determined by counting cells from 4× micrographs with ImageJ. Data represent mean ± SD of five (**A**, **B**) independent replicates, calibrated against the control. Asterisks (*) indicate statistically significant differences ($p < 0.05$, Kruskal–Wallis test, followed by Dunn's multiple comparison test and Bonferroni correction). Micrographs shown in the figure were taken at 10× magnification (standard, 200 µm). (Figure modified from Biasella et al., 2020 [246]).

4.8.2   Influence of VTN_rs704:C and VTN_rs704:T on Endothelial Cell Autophagy

An effect of VTN_rs704:C and VTN_rs704:T on cell autophagy was examined in HUVEC cells subjected to oxidative stress (*via* H_2O_2 treatment) inducing autophagy [280]. Cells were treated for 24 h at 37°C with VTN_rs704:C, VTN_rs704:T or control eluate, and with 0 mM H_2O_2 or 1 mM H_2O_2. After 24 h, cells were harvested, and western blot analysis was conducted with cell lysates by using antibodies against autophagy marker LC3, comparing the ratio of its isoforms LC3-I (decreasing with autophagy induction) and LC3-II (increasing with autophagy induction) [266]. Densitometric quantification of six independent experiments revealed a decrease in the LC3-I/LC3-II ratio in HUVECs subjected to H_2O_2 compared to HUVECs incubated without H_2O_2 ($p < 0.05$ between H_2O_2-treated samples compared to H_2O_2-free samples; **Figure 19**), demonstrating the induction of autophagy in the oxidatively stressed cells. However, no statistical difference between VTN_rs704:C and VTN_rs704:T was observed (**Figure 19**).
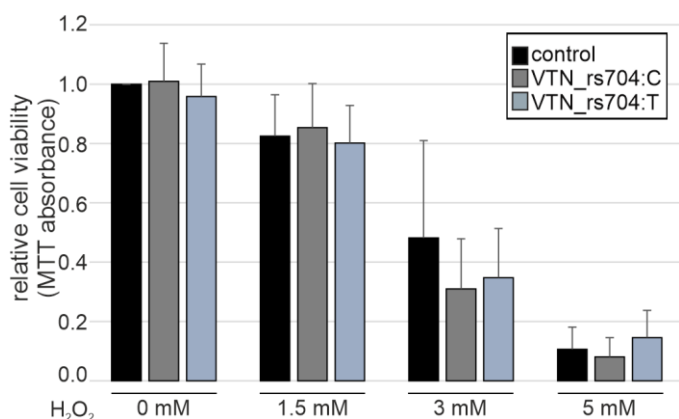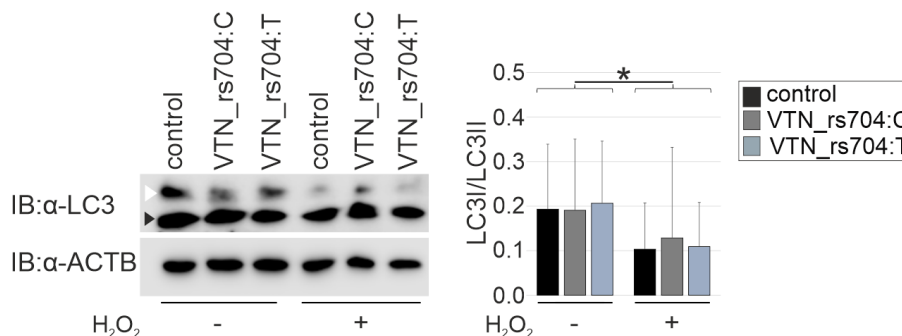
Figure 19: Effect of VTN_rs704:C and VTN_rs704:T on endothelial cell autophagy.
HUVECs were pre-incubated for 1 h with purified recombinant VTN_rs704:C, VTN_rs704:T or control eluate. Subsequently, cells were exposed for 24 h to 1mM H_2O_2 ($+H_2O_2$) or treated under the same conditions but without H_2O_2 ($-H_2O_2$), in the presence of fresh purified recombinant proteins. Cells were subjected to western blot analysis with antibodies against LC3 (α-LC3) and ACTB (α-ACTB) as loading control. After densitometric quantification, LC3I signals (white arrowhead) were normalised against the respective LC3II signals (black arrowhead). Data represent the mean ± SD of six biological replicates. Asterisks indicate statistically significant differences (*$p < 0.05$, Mann-Whitney U test).

4.8.3 Influence of VTN_rs704:C and VTN_rs704:T on Endothelial Cell Viability

The effect of VTN_rs704:C and VTN_rs704:T on endothelial cell viability was studied in HUVECs exposed to different levels of oxidative stress. To induce oxidative stress, HUVECs were exposed to 0, 0.5, 1 and 3 mM of H_2O_2 for 2 h at 37°C in the presence of VTN_rs704:C, VTN_rs704:T or control eluate. After a period of 18 h, allowing the cells to recover in the presence of VTN_rs704:C, VTN_rs704:T or control eluate, cells were subjected to the MTT assay. Quantification of six independent experiments showed a reduction in oxidoreductase activity and thus cell viability with increasing concentrations of H_2O_2 (**Figure 20**). No difference was observed between cells treated with VTN_rs704:C, VTN_rs704:T, or control eluate, under all oxidative stress conditions applied (**Figure 20**).
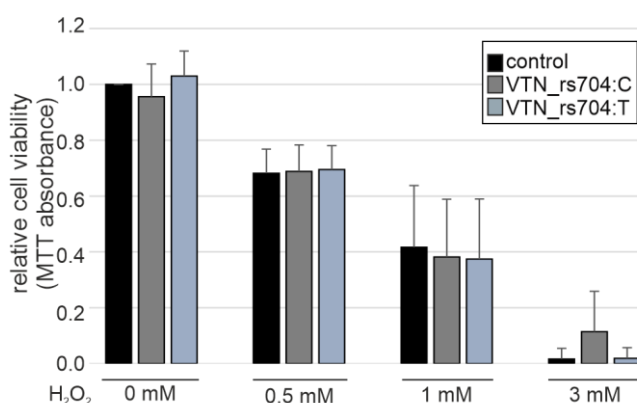
Figure 20: Effect of VTN_rs704:C and VTN_rs704:T on endothelial cell viability.
HUVEC cells were exposed to 0, 0.5, 1 and 3 mM H_2O_2 for 2h in the presence of purified recombinant VTN_rs704:C, VTN_rs704:T or control eluate. After a period of 18 h allowing the cells to recover in the presence of purified recombinant VTN_rs704:C, VTN_rs704:T or control eluate, cells were subjected to the MTT assay. Data represent the mean ± SD of six biological replicates calibrated against control at 0 mM H_2O_2.

4.8.4 Influence of VTN_rs704:C and VTN_rs704:T on Endothelial ERK Signalling

To investigate an effect of VTN_rs704:C and VTN_rs704:T on the regulation of ERK signalling in endothelial cells, HUVECs were incubated with purified recombinant VTN_rs704:C, VTN_rs704:T, or control eluate for 24 h at 37°C. After incubation, cells were

harvested, and subjected to western blot analysis following ERK1/2 phosphorylation as a marker of ERK signalling induction [275,276]. Quantification of six independent experiments revealed no differences in the cellular levels of phosphorylated ERK1/2 and thus in ERK signalling activation between vitronectin-treated cells and control-treated cells (**Figure 21**).
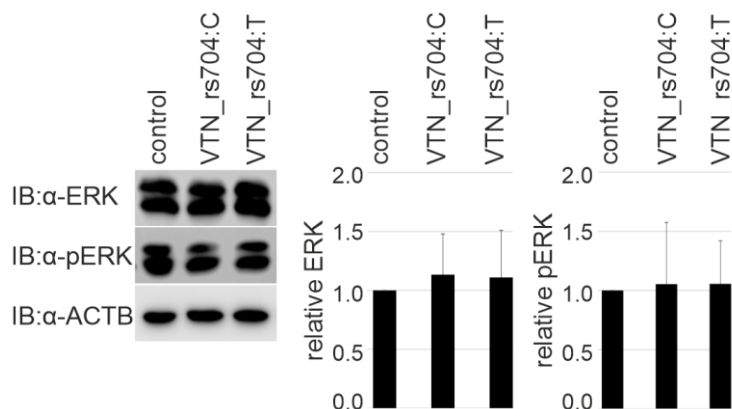
Figure 21: Effect of VTN_rs704:C and VTN_rs704:T on ERK1/2 activation in endothelial cells.
HUVEC cells were treated with purified recombinant VTN_rs704:C, VTN_rs704:T or control eluate. After 24 h, cells were subjected to western blot analysis with antibodies against ERK1/2 (α-ERK), phosphorylated ERK1/2 (α-pERK) and ACTB (α-ACTB), as loading control. After densitometric quantification, ERK1/2 and phosphorylated ERK1/2 (pERK) signals were normalised against ACTB. Data represent the mean ± SD of six biological replicates calibrated against the control.

4.8.5 Influence of VTN_rs704:C and VTN_rs704:T on Endothelial Cell Migration

To assess an effect of VTN_rs704:C and VTN_rs704:T on endothelial cell migration, a "scratch-wound assay" was performed in HUVECs. To this end, HUVECs were grown overnight to confluency. Subsequently, cell monolayers were subjected to a scratch-wound (**Figure 22A**) and incubated with purified recombinant VTN_rs704:C, VTN_rs704: T, or control eluate for 14 h at 37°C. Wound closure and thus cell migration was monitored under the microscope. Specifically, the scratch area was measured 0 h (**Figure 22A**) and 14 h (**Figure 22B**) after the scratch was introduced. Quantification of six independent experiments showed that the presence of recombinant purified VTN_rs704:C but not of VTN_rs704:T slightly reduced the relative HUVEC migration (VTN_rs704:C, 93.3% ± 5.0% compared to control; $p < 0.05$ between VTN_rs704:C and control, as well as between VTN_rs704:C and VTN_rs704:T).
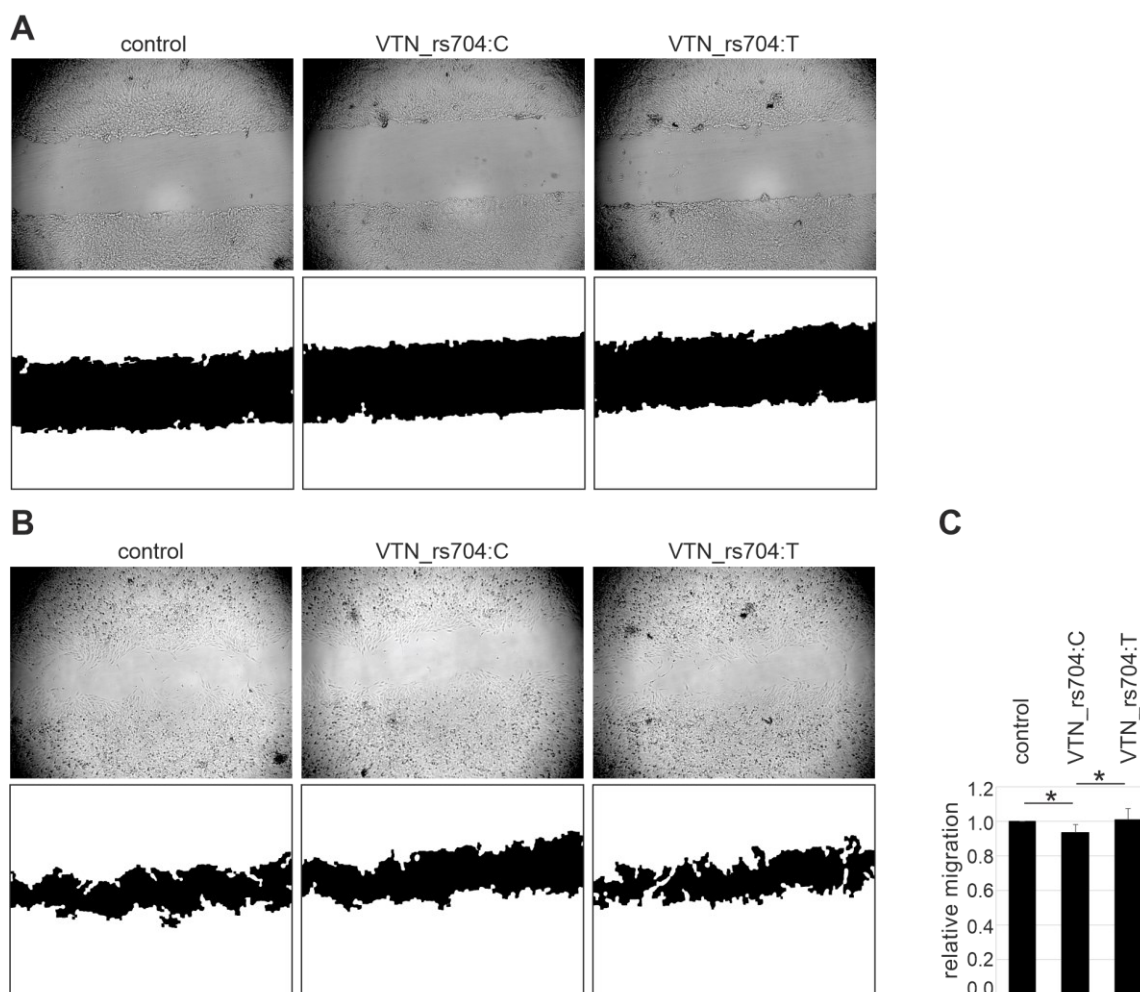
Figure 22: Effect of VTN_rs704:C and VTN_rs704:T on endothelial cell migration.
A scratch wound was introduced into HUVEC monolayers. After 14 h of incubation at 37°C in the presence of VTN_rs704:C, VTN_rs704:T, or control eluate, relative cell migration, defined as the percentage area closed after 14 h of incubation, was determined with ImageJ from the ratio of (**B**) the occupied area of the initially scratched surface to (**A**) the total area of the initial scratch. Data represent the mean ± SD of six independent replicates, calibrated against the control (**C**). (Figure modified from Biasella et al., 2020 [246]).

4.8.6 Effect of VTN_rs704:C and VTN_rs704:T on Endothelial Tubulogenesis

An influence of VTN_rs704:C and VTN_rs704:T on the capacity of endothelial cells to form three-dimensional capillary-like tubular structures was investigated in HUVEC cells. In "tube formation assays", HUVEC cells were seeded on Geltrex-coated plates, incubated with purified recombinant VTN_rs704:C, VTN_rs704: T, or control eluate, and cultured for 16 h at 37°C. The formation of capillary-like tubular structures was followed by bright-field microscopy. Both vitronectin isoforms decreased the length of tubes formed by HUVECs compared to the control (quantification of eleven independent experiments revealed a reduction to 78.8% ± 27.2% by VTN_rs704:C and to 85.2% ± 11.9% by VTN_rs704:T compared to control; $p < 0.05$ between control and both vitronectin isoforms; **Figure 23**).
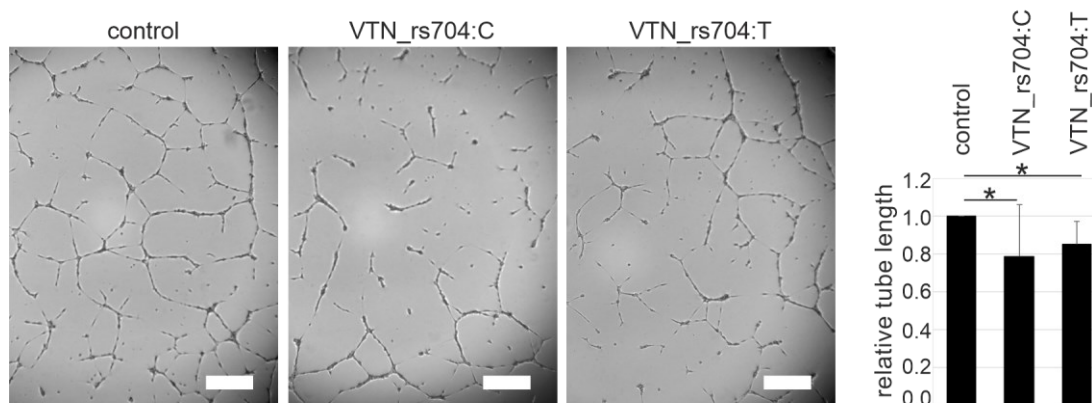
Figure 23: Effect of VTN_rs704:C and VTN_rs704:T on endothelial tubulogenesis.
HUVECs were cultivated in the presence of purified recombinant VTN_rs704:C, VTN_rs704:T, or control eluate. After 16 h, the formation of tubular-like structures was followed microscopically (standard, 400 μm). The length of tubular-like structures was measured using ImageJ. Data represent mean ± SD of eleven independent replicates calibrated against the control. Asterisks (*) indicate statistically significant differences ($p < 0.05$, Kruskal-Wallis test, followed by Dunn's multiple comparison test and Bonferroni correction). (Figure modified from Biasella et al., 2020 [246]).

4.9 Role of VTN_rs704:C and VTN_rs704:T on ECM Deposition and Composition

Changes in the five-layered ECM of Bruch's membrane are an early and characteristic pathological process in AMD development [210]. In the following analyses, an effect of VTN_rs704:C and VTN_rs704:T on ECM deposition by RPE cells was investigated in ARPE-19, a model system commonly used to study ECM alteration associated with AMD *in vitro* [101,259,281].

ARPE-19 cells were transfected with expression vectors for VTN_rs704:C, VTN_rs704:T, or with a control expression vector. After 24 h, transfected cells were transferred onto Transwell filters, where ARPE-19 monolayers were cultured for 4 weeks. After that, the cells were removed from the filters and the ECM composition was analysed by immunolabelling followed by confocal microscopy.

4.9.1 Influence of rs704 on Vitronectin Deposition in the ECM

First, an effect of rs704 on the deposition of vitronectin into the ECM was assessed. Immunolabeling of ARPE-19-derived ECM with antibodies against vitronectin showed an increased ECM deposition of VTN_rs704:T compared to VTN_rs704:C. Quantification of eight independent experiments revealed a 2.82 ± 1.89-fold increase in VTN_rs704:T signal intensity and a 1.99 ± 1.04-fold increase in VTN_rs704:T cluster size compared to VTN_rs704:C ($p < 0.05$). No vitronectin was detected in the control ECM derived from ARPE-19 cells transfected with the control expression vector (**Figure 24**).
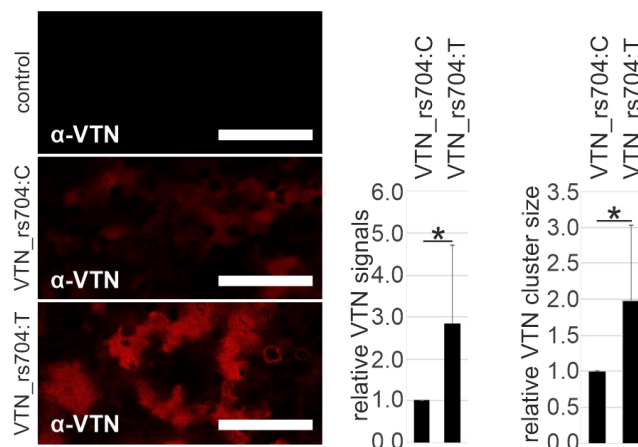
Figure 24: Effect of rs704 on vitronectin deposition into ARPE-19-deposited ECM
ARPE-19 cells transfected with expression vectors for VTN_rs704:C or VTN_rs704:T or with an empty control expression vector (pcDNA3.1) were incubated for 4 weeks on Transwell filters. After 4 weeks, the inserts were decellularized and subjected to immunostaining with antibodies against vitronectin (α-VTN). Confocal microscopy images were taken at 10× magnification. Scale bars: 100 µm. Fluorescence intensity and average cluster size were measured using ImageJ. Data represent the mean ± SD of eight biological replicates calibrated against the control. Asterisks (*) indicate statistically significant differences (*$p < 0.05$, Kruskal-Wallis test, followed by Dunn's multiple comparison test with Bonferroni correction). (Figure modified from Biasella et al., 2020 [246]).

4.9.2 Effect of VTN_rs704:C and VTN_rs704:T on Deposition of ECM Structural Components

Next, an effect of VTN_rs704:C and VTN_rs704:T on the deposition and clustering of characteristic ECM structural components laminin, fibronectin, elastin, and collagen type V and VI [282] was analysed.

Laminin staining reflected disorganized fibers and aggregates in all ECMs analysed. The amount of laminin and its assembly were not affected by heterologous expression of the two vitronectin isoforms. Quantification of five independent experiments revealed a laminin signal intensity of 1.11 ± 0.16 in VTN_rs704:C-containing ECM and of 1.00 ± 0.05 in VTN_rs704:T-containing ECM, compared to control ECM. The cluster size of laminin was 0.96 ± 0.20 in VTN_rs704:C-containing ECM and 0.93 ± 0.21 in VTN_rs704:T-containing ECM, compared to control (**Figure 25A**).

Fibronectin appeared as densely packed aggregates in ECMs of non-vitronectin expressing cells. In ECMs containing vitronectin, these aggregates extended and formed fibers, with an increase in total fibronectin signal intensity. Both processes (fiber formation and total fibronectin deposition) appeared more pronounced in VTN_rs704:T- than in VTN_rs704:C-containing ECMs. i. e. quantification of five independent experiments revealed an increased fibronectin signal intensity of 1.50 ± 0.64 in VTN_rs704:C-containing ECMs, and of 1.95 ± 1.15 in VTN_rs704:T-containing ECMs, compared to control ($p < 0.05$ between VTN_rs704:T and control; **Figure 25B**). In addition, the presence of vitronectin affected the size of fibronectin clusters, which increased to 1.44 ± 0.64 in VTN_rs704:C-containing ECMs and to

2.50 ± 1.12 for VTN_rs704:T-containing ECM (p < 0.05 between VTN_rs704:T and control; **Figure 25B**).

Elastin staining revealed a similar appearance than fibronectin staining: densely packed elastin aggregates were observed in ECMs of non-vitronectin expressing cells, while increased elastin deposition and fiber formation was observed in ECMs containing vitronectin. A quantification of five independent experiments revealed a slight increase in elastin signal intensity to 1.08 ± 0.05 in VTN_rs704:C-containing ECMs and to 1.12 ± 0.06 in VTN_rs704:T-containing ECMs, compared to control (p < 0.05 between VTN_rs704:T and control). Both vitronectin isoforms had a similar effect on elastin aggregation, leading to an increase in elastin cluster size to 1.62 ± 0.45 in VTN_rs704:C-containing ECMs and to 1.51 ± 0.34 in VTN_rs704:T-containing ECMs, compared to control (p < 0.05 between both vitronectin isoforms and control; **Figure 25C**).

Figure 25: Effect of VTN_rs704:C and VTN_rs704:T on deposition of laminin, fibronectin, and elastin into ARPE-19-deposited ECM.
ARPE-19 cells transfected with expression vectors for VTN_rs704:C or VTN_rs704:T or with an empty control expression vector (pcDNA3.1) were incubated for 4 weeks on Transwell filters. After 4 weeks, the inserts were decellularized and subjected to immunostaining with antibodies against (**A**) laminin (α-LAM), (**B**) fibronectin (α-FN), and (**C**) elastin (α-ELA). Confocal microscopy images were taken at 10× magnification. Scale bars: 100 µm. Fluorescence intensity and average cluster size were measured using ImageJ. Data represent the mean ± SD of five biological replicates calibrated against the control. Asterisks (*) indicate statistically significant differences (p < 0.05, Kruskal–Wallis test, followed by Dunn's multiple comparison test with Bonferroni correction). (Figure modified from Biasella et al., 2020 [246]).

Staining of collagen V revealed fibers in all ECMs analysed. Quantification of five independent experiments demonstrated a signal intensity for collagen V tendentially higher in ECMs containing vitronectin (VTN_rs704:C: 1.52 ± 0.92, VTN_rs704:T: 2.53 ± 2.18, compared to control, p > 0.05, **Figure 26A**). The analysis of cluster size also showed a slight effect of the presence of VTN_rs704:C and VTN_rs704:T, with both isoforms tendentially increasing collagen V clustering (VTN_rs704:C: 1.29 ± 0.38, VTN_rs704:T: 3.46 ± 4.84, compared to control, p > 0.05, **Figure 26A**).

Immunolabelling of collagen VI revealed an ECM deposition but without prominent cluster or fiber formation (**Figure 26B**). In vitronectin-containing ECM, a notable increase of collagen VI clustering was observed. Although quantification of six independent experiments failed to show a statistically significant increase in total collagen VI signal intensity, collagen VI cluster size was strongly affected. Again, VTN_rs704:T exerted a stronger effect than VTN_rs704:C (1.45 ± 0.42 for VTN_rs704:C-containing ECMs and 1.81 ± 0.35 for VTN_rs704:T-containing ECMs compared to control; $p < 0.05$ between VTN_rs704:T and control; **Figure 26B**). Interestingly, co-immunolabelling of collagen VI and vitronectin showed an almost identical distribution pattern, suggesting a possible interaction between both components (**Figure 26B**).

Figure 26: Effect of VTN_rs704:C and VTN_rs704:T on deposition of collagens into ARPE-19-deposited ECM. ARPE-19 cells transfected with expression vectors for VTN_rs704:C or VTN_rs704:T or with an empty control expression vector (pcDNA3.1) were incubated for 4 weeks on Transwell filters. After 4 weeks, the inserts were decellularized and subjected to immunostaining with antibodies against (**A**) collagen V (α-COL V) and (**B**) collagen VI (α-COL VI). Merged picture showed co-stained collagen VI and vitronectin (α-VTN) (**B**). Confocal microscopy images were taken at 10× magnification. Scale bars: 100 µm. Fluorescence intensity and average cluster size were measured using ImageJ. Data represent the mean ± SD of five (collagen V) and six (collagen VI) biological replicates calibrated against the control. Asterisks (*) indicate statistically significant differences ($p < 0.05$, Kruskal-Wallis test, followed by Dunn's multiple comparison test with Bonferroni correction). (Figure B modified from Biasella et al., 2020 [246]).

4.9.3 Effect of VTN_rs704:C and VTN_rs704:T on Deposition of ECM Functional Components
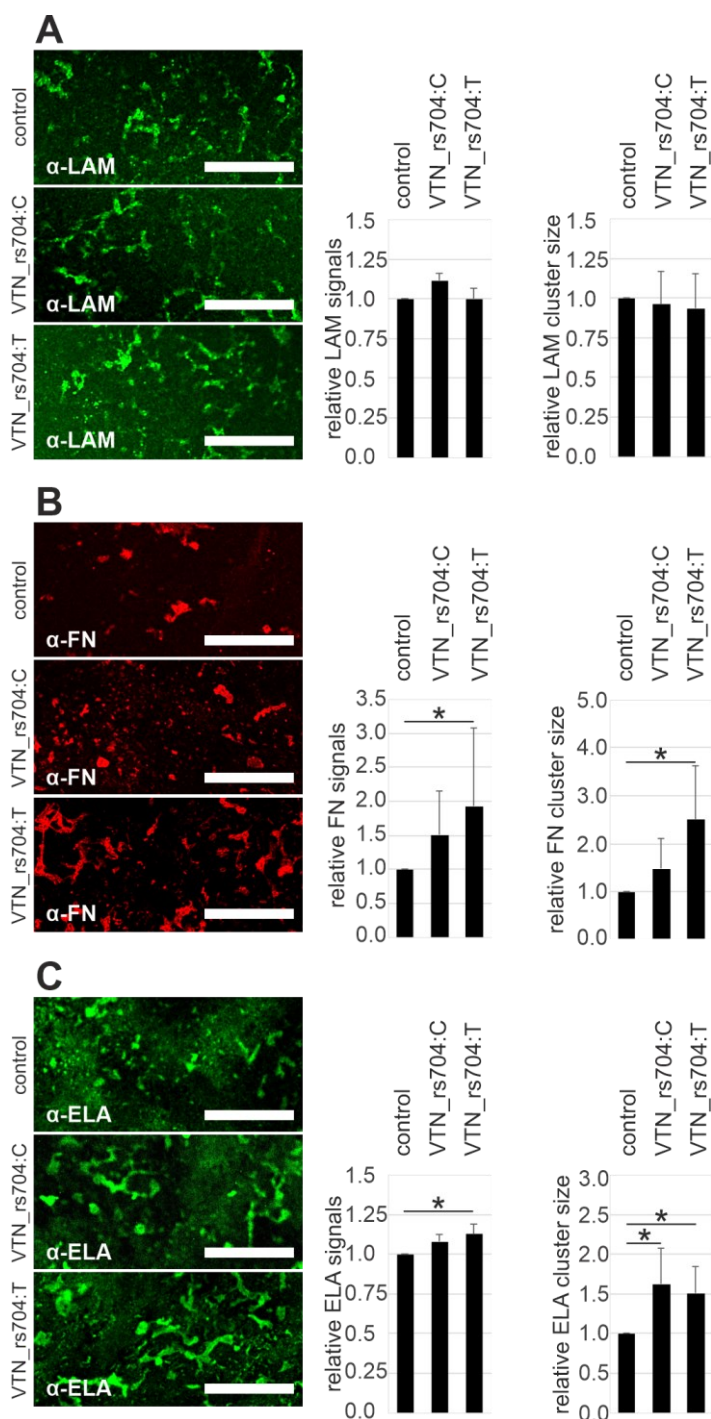
Next, the effect of VTN_rs704:C and VTN_rs704:T on the deposition of functional components known to be part of the ECM and shown to be associated with AMD aetiology, like complement factors C9 and CFH [283,284], TIMP3 [95,285], and VEGF [58,286] were analysed.

4.9.3.1 Effect of VTN_rs704:C and VTN_rs704:T on ECM Deposition of Complement Factors

C9 appeared as densely packed aggregates in the ECM. The analysis of five independent experiments showed that the presence of vitronectin in these matrices was correlated with increased C9 signal intensity (1.44 ± 0.46 for VTN_rs704:C and 1.76 ± 0.56 for VTN_rs704:T compared to control; $p < 0.05$ between VTN_rs704:T and control; **Figure 27A**). In addition, C9 aggregates showed a notable increase in size towards vitronectin with a more pronounced effect in the presence of VTN_rs704:T (1.38 ± 0.18 in VTN_rs704:C-containing ECMs, and 1.97 ± 0.36 in VTN_rs704:T-containing ECMs, compared to control; $p < 0.05$). between VTN_rs704:T and control; **Figure 27A**).

In contrast to C9, CFH was more evenly distributed along the ECM without prominent fiber formation. Again, the analysis of five independent experiments showed that vitronectin protein expression was associated with increased CFH signal intensity (2.08 ± 0.52 in VTN_rs704:C-containing ECMs and 2.35 ± 0.65 in VTN_rs704:T-containing ECMs, compared to control; $p < 0.05$ between VTN_rs704:T and control; **Figure 27B**). In vitronectin-containing matrices, CFH formed a meshwork with an observable increase in CFH aggregation (9.53 ± 10.48 -fold in VTN_rs704:C-containing ECMs and 8.35 ± 10.13-fold in VTN_rs704:T-containing ECMs, compared to control; $p < 0.05$ between VTN_rs704:C as well as between VTN_rs704:T and control; **Figure 27B**).
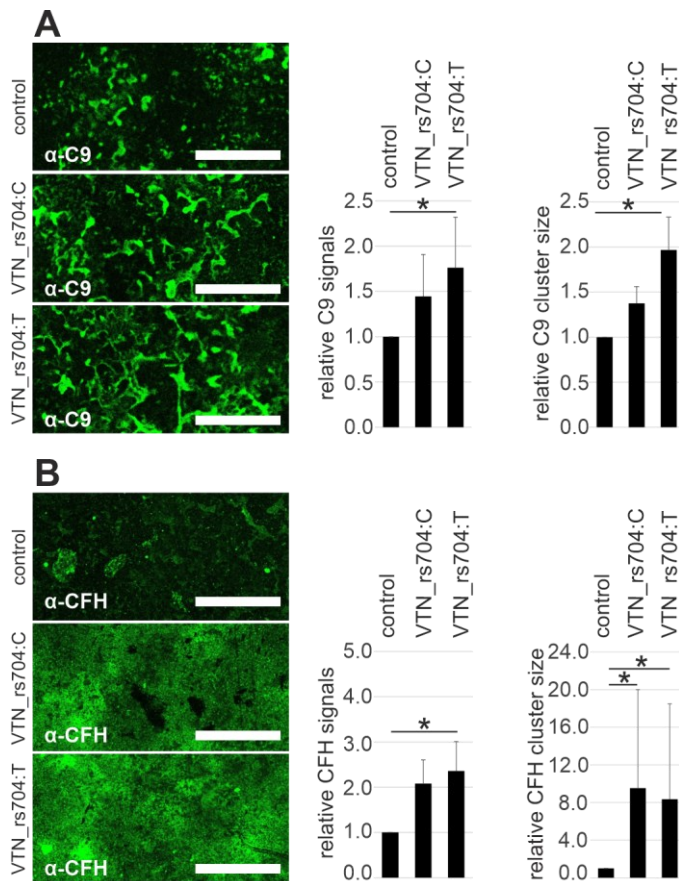
Figure 27: Effect of VTN_rs704:C and VTN_rs704:T on deposition of complement factors C9 and CFH into ARPE-19-deposited ECM.
ARPE-19 cells transfected with expression vectors for VTN_rs704:C or VTN_rs704:T or with an empty control expression vector (pcDNA3.1) were incubated for 4 weeks on Transwell filters. After 4 weeks, the inserts were decellularized and subjected to immunostaining with antibodies against (**A**) complement component 9 (α-C9) and (**B**) complement factor H (α-CFH). Confocal microscopy images were taken at 10× magnification. Scale bars: 100 μm. Fluorescence intensity and average cluster size were measured using ImageJ. Data represent the mean ± SD of five biological replicates calibrated against the control. Asterisks (*) indicate statistically significant differences ($p < 0.05$, Kruskal-Wallis test, followed by Dunn's multiple comparison test with Bonferroni correction).

4.9.3.2 Effect of VTN_rs704:C and VTN_rs704:T on ECM Deposition of TIMP3

Quantification of six independent experiments showed that the signal intensity and thus the total amount of deposited TIMP3 was unaffected by the presence of vitronectin (1.07 ± 0.17 in VTN_rs704:C-containing ECMs, and 1.15 ± 0.11 in VTN_rs704:T-containing ECMs, compared to control). In contrast, the size of TIMP3 aggregates was more prominent in the presence of VTN_rs704:T (1.81 ± 0.94 in VTN_rs704:C-containing ECMs and 4.46 ± 7.08 in VTN_rs704:T-containing ECMs, compared to control; $p < 0.05$ between VTN_rs704:T and control; **Figure 28**).
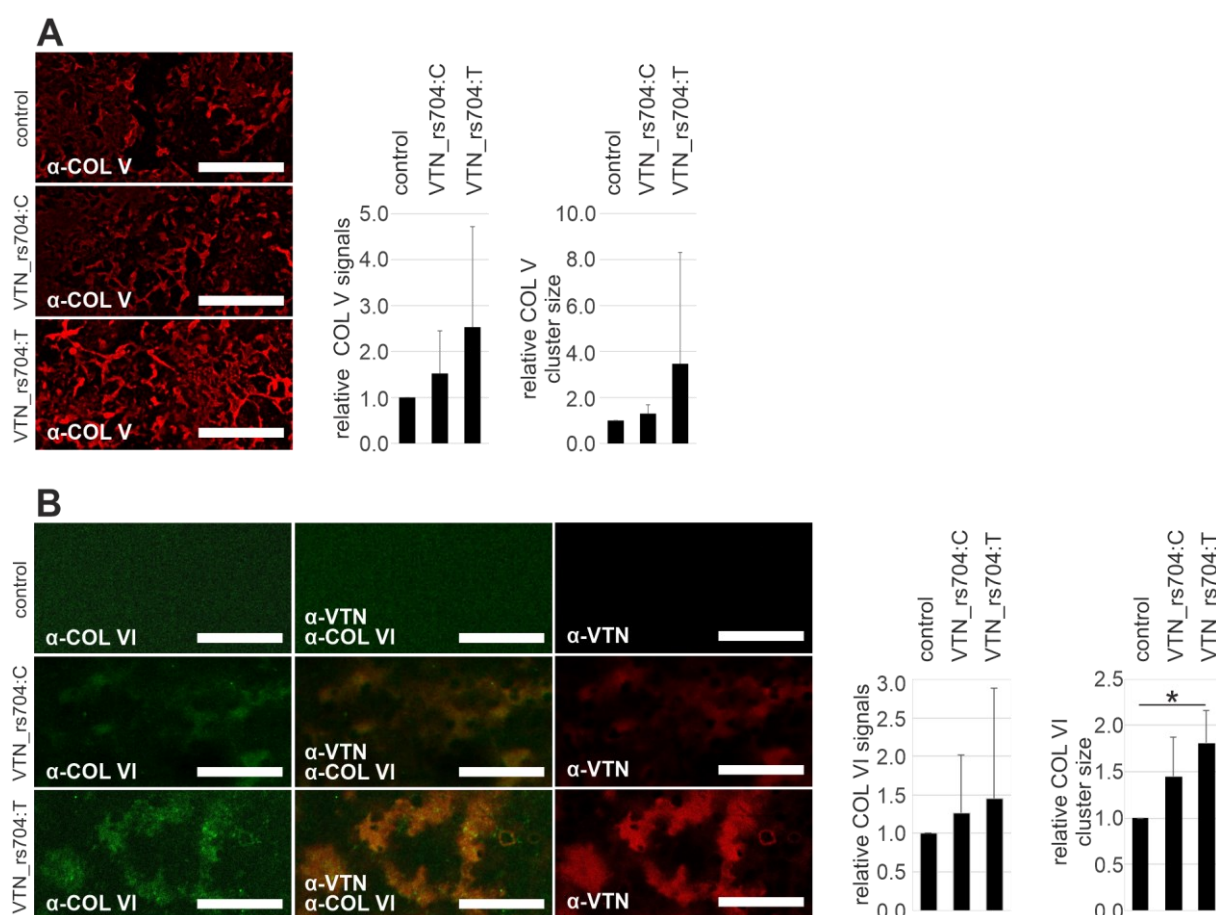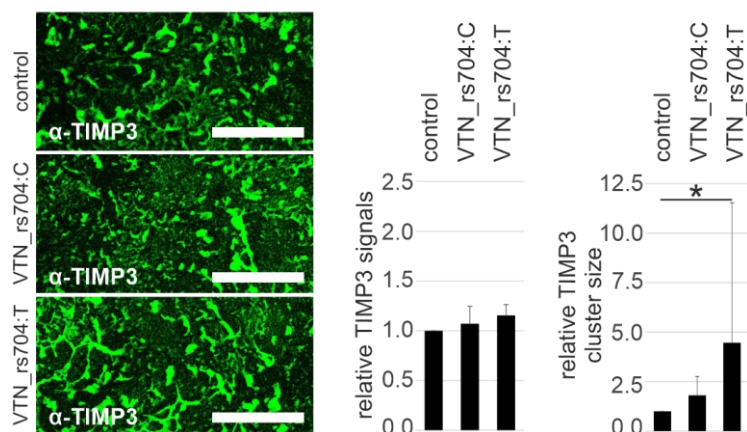
Figure 28: Effect of VTN_rs704:C and VTN_rs704:T on deposition of TIMP3 into ARPE-19-deposited ECM.
ARPE-19 cells transfected with expression vectors for VTN_rs704:C or VTN_rs704:T or with an empty control expression vector (pcDNA3.1) were incubated for 4 weeks on Transwell filters. After 4 weeks, the inserts were decellularized and subjected to immunostaining with antibodies against tissue inhibitor of metalloproteinase 3 (α-TIMP3). Confocal microscopy images were taken at 10× magnification. Scale bars: 100 μm. Fluorescence intensity and average cluster size were measured using ImageJ. Data represent the mean ± SD of six biological replicates calibrated against the control. Asterisks (*) indicate statistically significant differences (p < 0.05, Kruskal-Wallis test, followed by Dunn's multiple comparison test with Bonferroni correction).

4.9.3.3 Effect of VTN_rs704:C and VTN_rs704:T on ECM Deposition of VEGF

Finally, an effect of VTN_rs704:C and VTN_rs704:T on VEGF deposition was investigated in the ECMs produced by ARPE-19 cells heterologously expressing VTN_rs704:C or VTN_rs704:T. Quantification of six independent experiments showed a significant increase in VEGF signal intensity in vitronectin-containing ECMs compared to vitronectin-free ECMs (1.55 ± 0.73 with VTN_rs704:C and 1.73 ± 0.92 with VTN_rs704:T compared to control; p < 0.05 between VTN_rs704:C as well as between VTN_rs704:T and control; **Figure 29**). The presence of vitronectin also seemed to increase VEGF aggregation (1.91 ± 0.57 for VTN_rs704:C and 4.02 ± 4.62 for VTN_rs704:T compared to control; p > 0.05 between all replicates; **Figure 29**).
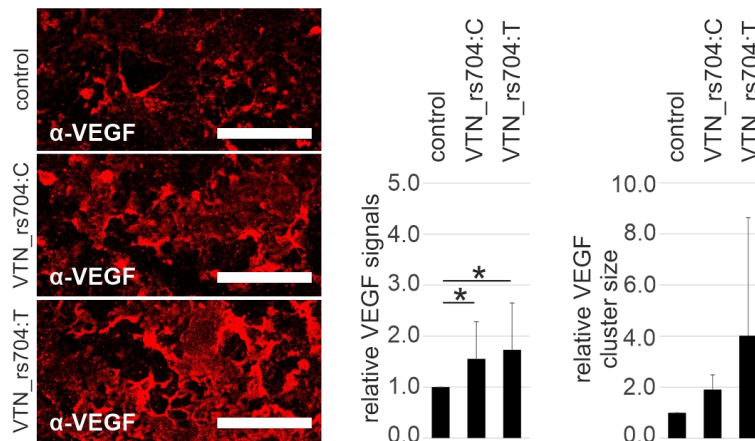
Figure 29: Effect of VTN_rs704:C and VTN_rs704:T on deposition of VEGF into ARPE-19-deposited ECM.
ARPE-19 cells transfected with expression vectors for VTN_rs704:C or VTN_rs704:T or with an empty control expression vector (pcDNA3.1) were incubated for 4 weeks on Transwell filters. After 4 weeks, the inserts were decellularized and subjected to immunostaining with antibodies against vascular endothelial growth factor (α-VEGF). Confocal microscopy images were taken at 10× magnification. Scale bars: 100 µm. Fluorescence intensity and average cluster size were measured using ImageJ. Data represent the mean ± SD of six biological replicates calibrated against the control. Asterisks (*) indicate statistically significant differences ($p < 0.05$, Kruskal-Wallis test, followed by Dunn's multiple comparison test with Bonferroni correction).

4.10 Interaction of VTN_rs704:C and VTN_rs704:T with PAI-1

The interaction of vitronectin with PAI-1 is well characterised [185,287,288]. Of interest, PAI-1 has been implicated in neovascular AMD [289-291].

4.10.1 Influence of rs704 on Vitronectin Capacity to Bind PAI-1

Differences between VTN_rs704:C and VTN_rs704:T in their respective ability to bind PAI-1 were investigated using affinity chromatography. After immobilization of Strep-tagged PAI-1 onto gravity flow columns, medium containing VTN_rs704:C and VTN_rs704:T heterologously expressed by HEK293-EBNA cells, or vitronectin-free control medium was loaded onto the columns. After intensive washing, elution of PAI-1 (and thus co-elution of PAI-1 bound proteins) was performed. Western blot analysis demonstrated the presence of both vitronectin isoforms in the elution fractions (**Figure 30A**, eluted fractions highlighted in black rectangle), and thus effective binding of both VTN_rs704:C and VTN_rs704:T to PAI-1. Interestingly, densitometric quantification of five independent experiments revealed higher levels of VTN_rs704:T in the eluted PAI-1 fraction compared to VTN_rs704:C (2.28 ± 0.81-fold increase, $p < 0.05$; **Figure 30A**), suggesting a potential influence of rs704 on the ability of vitronectin to bind PAI-1.

As a negative control, input without vitronectin was loaded onto columns coupled with PAI-1 and subjected to the identical experimental procedure described for vitronectin-containing input (**Figure 30B**). In this experiment, no vitronectin staining was observed in any of the fractions analysed. An additional control experiment without immobilised PAI-1 failed to detect vitronectin signals in the elution fraction. Instead, vitronectin was found predominantly

in the flow through and wash fractions (**Figure 30C**), excluding unspecific binding of vitronectin isoforms to the column material.
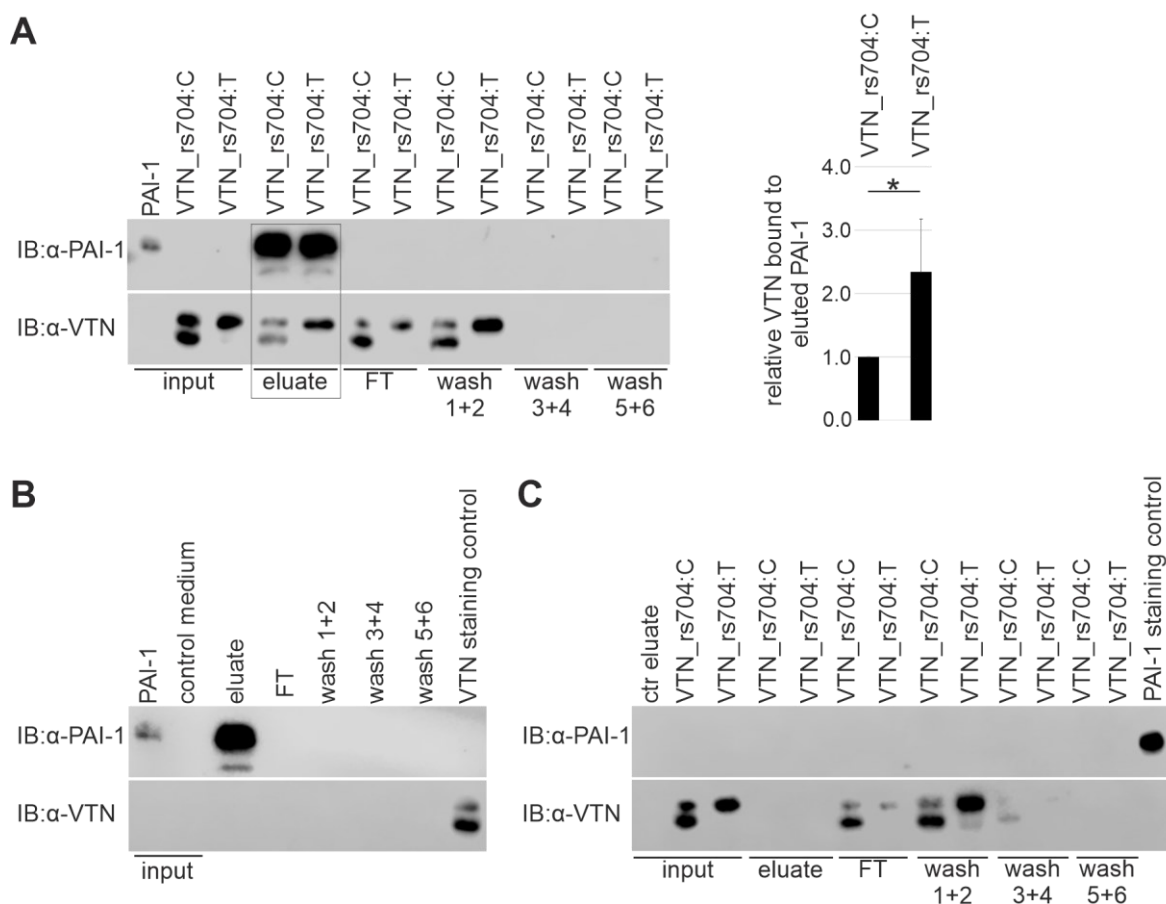
Figure 30: Effect of rs704 on the capacity of vitronectin to bind PAI-1.
(**A**) PAI-1-coupled affinity chromatography columns (input) were loaded with medium containing untagged VTN_rs704:C or VTN_rs704:T (input). After several washing steps, proteins were eluted (´eluate`) and subjected to immunoblot (IB) analysis with antibodies against vitronectin (α-VTN) and PAI-1 (α-PAI-1). Also shown are flow through (FT) and wash fractions (wash) obtained prior to PAI-1 elution. After densitometric quantification, vitronectin signals in the eluate were normalised for the respective inputs and eluted PAI-1. Data represent the mean ± SD of five replicates, calibrated against VTN_rs704:C. Asterisks (*) indicate statistically significant differences (p < 0.05, Mann-Whitney U test). (**B**) Control medium without vitronectin loaded onto PAI-1-coupled columns and subjected to the identical experimental procedure described in (**A**). (**C**) Non-specific binding of vitronectin to column material tested by loading medium containing untagged vitronectin (input) onto columns without PAI-1 (coupled with empty control eluate) and subjected to the identical experimental procedure as in (**A**). (Figure modified from Biasella et al., 2022 [292]).

4.10.2 Influence of VTN_rs704:C and VTN_rs704:T on Preserving PAI-1 Activity

Under physiological conditions, PAI-1 spontaneously converts from the enzymatically active state to an energetically more favourable but non-functional (latent) conformation with a half-life of ~2 h. The process involves the internal translocation of the reactive centre loop (**Figure 31A**), which is responsible for the initial interaction of PAI-1 with uPA [226]. Through allosteric regulation, vitronectin stabilises the active state of PAI-1 by hindering the insertion of its reactive centre loop [226] (**Figure 31B**).
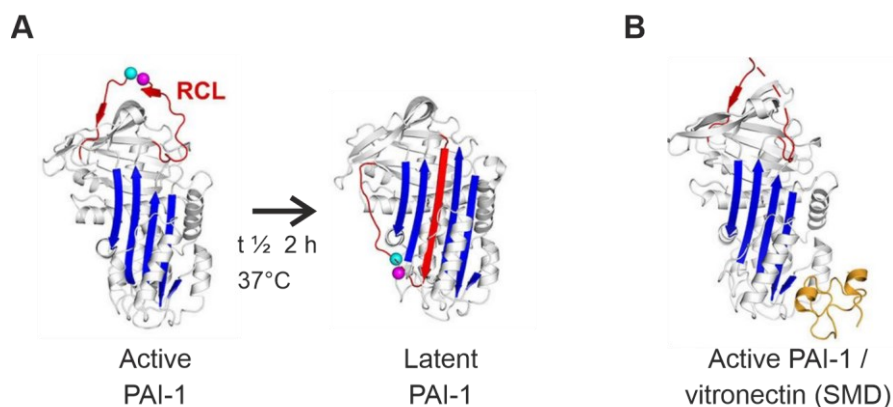
Figure 31: Schematic overview of PAI-1 functional states.
(**A**) PAI-1 spontaneously converts from the active to the latent form with a half-life ($t^{1/2}$) of ~2 h at 37°C. During this transition the reactive centre loop (RLC) of PAI-1 (shown in red) is translocated within the central β-sheet (in blue) of the PAI-1 molecule. (**B**) The somatomedin domain (SMD) of vitronectin (shown in orange) binds to PAI-1 and prevents the internalisation of its RCL by stabilising its active state. (Figure modified from Sillen and Declerck, 2020 [226]).

On this basis, the consequence of rs704 on the ability of vitronectin stabilise PAI-1 was examined *via* the cell-free PAI-1 activity assay. This assay assesses the inhibitory effect of PAI-1 on the proteolytic activity of its target protease uPA [226,293], which in turn cleaves a chromogenic substrate. To allow stabilization of active PAI-1 by the two vitronectin isoforms, PAI-1 was pre-incubated with VTN_rs704:C, VTN_rs704:T, or control eluate, for 0, 1, 2, 3, 4, 5, and 7 h. After pre-incubation, aliquots from the mixture of PAI-1 with vitronectin or with control eluate were subjected to the PAI-1 activity assay applying an incubation time of 2.5 h. Quantification of six independent experiments showed that both VTN_rs704:C and VTN_rs704:T similarly stabilised enzymatically active PAI-1, and thus increased PAI-1-induced uPA inhibition. A stabilizing effect was already observed after 0 h of pre-incubation (uPA inhibition by PAI-1 at 0 h: 83% ± 11% in the presence of VTN_rs704:C, 79% ± 14% in the presence of VTN_rs704:T, 58% ± 17% in the presence of control eluate, $p < 0.05$ between VTN_rs704:C and control, **Figure 32A**) likely due to a stabilising effect of the vitronectin during the 2.5 h of incubation required for the enzymatic reaction in the assay (see above). From 1 to 7 h of pre-incubation, both vitronectin isoforms showed a similar capacity to stabilize PAI-1. The stabilising effect of vitronectin on PAI-1 was still effective after 7 h of pre-incubation (uPA inhibition by PAI-1 at 7 h: 49% ± 11% in the presence of VTN_rs704:C and 47% ± 12% in the presence of VTN_rs704:T compared to 0% in the presence of control eluate; $p < 0.05$ between control and VTN_rs704:C or VTN_rs704:T; **Figure 32A**). In contrast, PAI-1 incubated with control eluate showed a strong and time-dependent decrease in its ability to inhibit uPA (uPA inhibition by PAI-1 decreasing from around 25 % at 1 h of pre-incubation to 0 % at 7 h of pre-incubation, **Figure 32A**). Similar results were obtained in an independent experiment to test the activity of PAI-1 isoforms upon long term pre-incubation with PAI-1: The stabilising effect on PAI-1 active state by vitronectin was still visible after 72 h, again without any differences between the two isoforms

(uPA inhibition by PAI-1 at 72 h: 40% ± 15% in the presence of VTN_rs704:C and 34% ± 18% in the presence of VTN_rs704:T compared to 0% in the presence of control eluate) (**Figure 32B**).
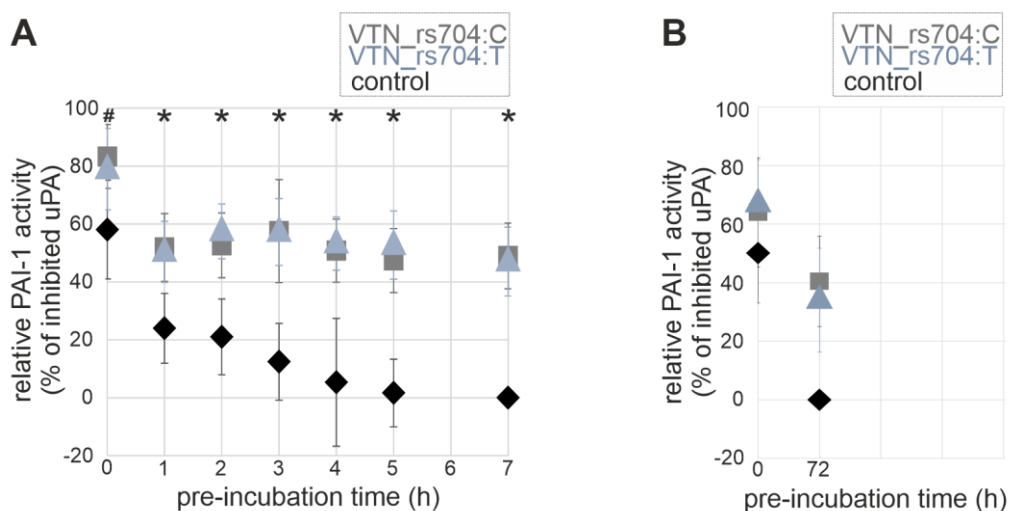
Figure 32: Effect of rs704 on the capacity of vitronectin to maintain PAI-1 active state.
VTN_rs704:C (grey squares), VTN_rs704:T (ice-blue triangles), or control eluate (control, black diamonds) were mixed with PAI-1 and incubated at 37°C. Aliquots of vitronectin/PAI-1 or control eluate/PAI-1 mixtures were subjected to the PAI-1 activity assay after 0, 1, 2, 3, 4, 5 and 7 h (**A**), or after 0 and 72 h (**B**) of pre-incubation. The PAI-1-dependent uPA activity was measured after 2.5 h of further incubation required for the enzymatic reaction. The data were calibrated against the values obtained for control measurements at 7 h (**A**) and at 72h (**B**) (uPA at its maximum activity in our experimental setting, 100%). To better visualize the extent of PAI-1 inhibition (and thus the inhibitory capacity of PAI-1), the calibrated uPA activity was subtracted from 100 % (maximal uPA activity). Data represent the mean ± SD of six replicates (**A**) and of three replicates (**B**). Asterisks (*) indicate statistically significant differences (p < 0.05, Kruskal-Wallis test, followed by Dunn's multiple comparison test with Bonferroni correction) between VTN_rs704:C as well as VTN_rs704:T and control. Hash character (#) indicates statistically significant difference (p < 0.05, Kruskal-Wallis test, followed by Dunn's multiple comparison test with Bonferroni correction) between VTN_rs704:C and control. (Figure modified from Biasella et al., 2022 [292]).

4.10.3 Effect of VTN_rs704:C and VTN_rs704:T on PAI-1 Expression

In this final project, the influence of rs704 on the capacity of vitronectin to affect PAI-1 expression and/or extracellular deposition was assessed in cultured endothelial and RPE cells.

Prior to these analyses, endogenous PAI-1 protein expression was determined in ARPE-19 cells and HUVECs. Western Blot analyses of ARPE-19 and HUVEC lysates revealed endogenous PAI-1 expression in both cell types. Specifically, PAI-1 was detected as a molecular weight species of approximately 50kDa corresponding to its glycosylated form [252,253]. In ARPE-19 cells, PAI-1 expression was weak compared to HUVECs: while no or only very faint signals were visible in the cell fraction of ARPE-19 cells, weak PAI-1 signals were visible in the culture medium of ARPE-19 cells. In contrast, a considerable amount of PAI-1 was detected in both cell lysates and culture medium of HUVECs (**Figure 33**).
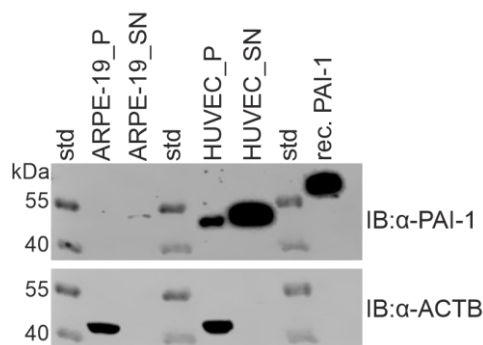
Figure 33: Endogenous PAI-1 protein expression in ARPE-19 cells and HUVECs.
Cells seeded on 6-well plates were cultured for 24 h. Endogenous PAI-1 (of about 50-54 kDa in its glycosylated form) was detected after western blot analysis of cell lysates (P) and culture medium (supernatant, SN) using antibodies against PAI-1. The ACTB immunoblot served as a loading control. Purified, Strep-tagged PAI-1 (50-54 kDa for glycosylated PAI-1 plus 5.1 kDa for Strep-tag) was loaded as a positive control.

4.10.3.1 PAI-1 Expression and Deposition into the ECM by HUVECs Exposed to Recombinant VTN_rs704:C and VTN_rs704:T

HUVECs were treated with purified recombinant VTN_rs704:C, VTN_rs704:T, or control eluate and incubated for 24 h at 37°C. After treatment, cells and ECM were harvested and subjected to western blot analysis with antibodies against PAI-1, vitronectin and ACTB (loading control). Quantification of nine independent experiments revealed an approximately 4-fold higher concentration of endogenous PAI-1 when cells were exposed to the two vitronectin isoforms in comparison to cells treated with control eluate (0.25 ± 0.26 with control eluate, 1.35 ± 0.72 with VTN_rs704:T, compared to VTN_rs704:C-treated cells, $p < 0.05$ between control and both vitronectin isoforms; **Figure 34A**). Concurrent with a precipitation of both VTN_rs704:C and VTN_rs704:T into the ECM (**Figure 34A**), an approximately 4-fold higher accumulation of PAI-1 was observed in the ECM of vitronectin-treated cells compared to cells treated with control eluate (0.26 ± 0.46 with control eluate, 1.34 ± 0.98 with VTN_rs704:T, compared to VTN_rs704:C-treated cells, $p < 0.05$ between control and both vitronectin isoforms; **Figure 34A**).

To investigate whether the enhancing effect of the two vitronectin isoforms on endogenous PAI-1 levels was a consequence of increased *PAI-1* gene expression, HUVECs were treated with VTN_rs704:C, VTN_rs704:T, or control eluate and incubated for 24 h at 37°C. After 24 h, RNA was isolated and *PAI-1* transcription was tested by qRT-PCR. Quantification of six independent experiments revealed no differences in *PAI-1* expression between cells treated with VTN_rs704:C, VTN_rs704:T, or control eluate (**Figure 34B**), and thus no effect of VTN_rs704:C and VTN_rs704:T on *PAI-1* mRNA expression.
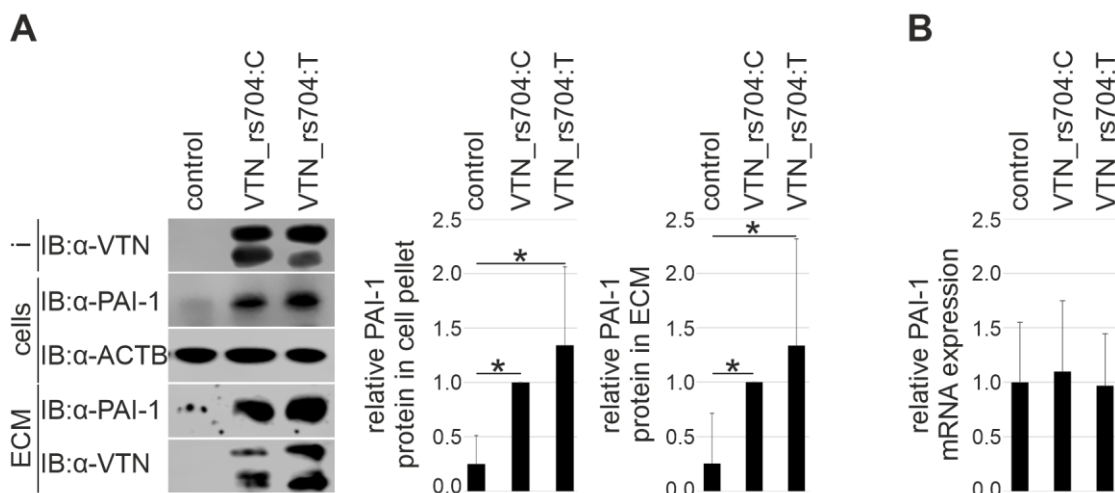
Figure 34: Effect of VTN_rs704:C and VTN_rs704:T on endogenous endothelial PAI-1 protein expression and ECM deposition.
HUVECs were incubated for 24 h with input (i) including purified VTN_rs704:C, VTN_rs704:T, or same volume of control eluate (control), respectively. (**A**) Input, cells and ECMs were subjected to immunoblot (IB) analysis with antibodies against vitronectin, PAI-1 and ACTB. PAI-1 signals were densitometrically quantified and normalized against ACTB. Data represent the mean ± SD of nine biological replicates, calibrated against the PAI-1 signals obtained after VTN_rs704:C addition. Asterisks (*) indicate statistically significant differences (p < 0.05, Kruskal-Wallis test, followed by Dunn's multiple comparison test with Bonferroni correction). (**B**) mRNA was isolated and PAI-1 expression determined by qRT-PCR. Data represent the mean ± SD of six biological replicates, calibrated against the control. (Figure modified from Biasella et al., 2022 [292]).

4.10.3.2 PAI-1 Deposition into the ECM by ARPE-19 Cells Heterologously Expressing VTN_rs704:C and VTN_rs704:T

ARPE-19 cells were transfected with expression vectors for VTN_rs704:C, VTN_rs704:T, or with a control expression vector. After 24 h, transfected cells were transferred onto Transwell filters and cultivated for 8 weeks. After 8 weeks, the cells were removed from the filters and the deposited ECM was analysed by immunolabelling of PAI-1 and vitronectin. Both VTN_rs704:C- and VTN_rs704:T-treated cells show an increasing effect on PAI-1 deposition in the ECM. Specifically, quantification of four independent experiments showed an approximately 3-fold increase in PAI-1 protein deposition in the vitronectin-containing ECMs compared to the vitronectin-free control matrixes (3.03 ± 1.73 with VTN_rs704:C, 2.59 ± 0.91 with VTN_rs704:T, compared to control; p < 0.05 between control and VTN_rs704:C or VTN_rs704:T; **Figure 35**). In addition, as observed in the ECM deposited by ARPE-19 cells after 4 weeks of cultivation (see section 4.9.1), a stronger deposition of VTN_rs704:T compared to VTN_rs704:C (1.99 ± 0.90-fold increased intensity of VTN_rs704:T compared to VTN_rs704:C; p < 0.05; **Figure 35**) was detected in the ECM deposited by transfected ARPE-19 after 8 weeks of cultivation.
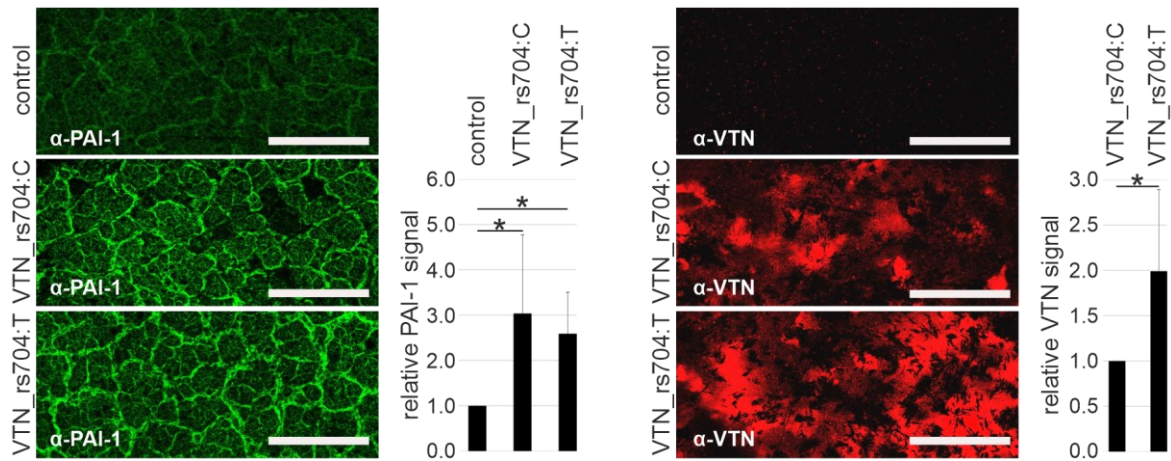
Figure 35: Effect of VTN_rs704:C and VTN_rs704:T on deposition of PAI-1 into ARPE-19-deposited ECM.
ARPE-19 cells transfected with expression vectors for VTN_rs704:C or VTN_rs704:T or with an empty control expression vector (pcDNA3.1) were incubated for 8 weeks on Transwell filters. After 8 weeks, the inserts were decellularized and subjected to immunostaining with antibodies against plasminogen activator inhibitor 1 (α-PAI-1) and vitronectin (α-VTN). Confocal microscopy images were taken at 10× magnification. Scale bars: 100 µm. Fluorescence intensities were measured using ImageJ. Data represent the mean ± SD of four independent replicates, calibrated against VTN_rs704:C (for vitronectin signals) or control (for PAI-1 signals). Asterisks (*) indicate statistically significant differences (*p < 0.05, Mann-Whitney U test for VTN; p < 0.05, Kruskal-Wallis test for PAI-1, followed by Dunn's multiple comparison test with Bonferroni correction). (Figure modified from Biasella et al., 2022 [292]).

5. Discussion

The incomplete understanding of the complex mechanisms causing AMD makes this common retinal disorder the leading cause of incurable blindness worldwide, along with social distress and negative impact on mental health due to its disabling effects on individual autonomy [294,295]. To contribute to a better understanding of the pathobiology of AMD, this doctoral thesis explored the functional significance of the statistical association of rs704 within the coding sequences of the *VTN* gene with AMD. The study presents evidence that this polymorphism significantly alters the expression of the encoded vitronectin protein, as well as vitronectin processing, secretion, and ability to bind retinal and endothelial cells. Functional investigations revealed a similar capacities of the non-AMD risk-associated VTN_rs704:C and AMD risk-associated VTN_rs704:T isoforms to regulate RPE cell adhesion and activation of the intracellular ERK signalling pathway. In endothelial cells, both isoforms decreased adhesion and tubulogenesis, while only the non-risk-associated isoform slightly reduced migration. Heterologous vitronectin expression in ARPE-19 cells increased ECM deposition and clustering of structural ECM constituents (e.g., fibronectin, elastin, collagen VI), as well as deposition of VEGF and complement factors (e.g., C9 and CFH), with the risk-associated isoform showing a greater effect on these parameters. Finally, exposure of RPE and endothelial cells to VTN_rs704:C and VTN_rs704:T enhanced expression and ECM deposition of PAI-1, a potent angiogenic regulator already implicated in AMD pathology [289-291]. While the risk-associated isoform exhibited a stronger binding to PAI-1, both isoforms equally maintained the active state of PAI-1. Taken together, this study suggests a close functional link between rs704 and vitronectin with functional consequences possibly for the pathogenesis of AMD.

5.1 AMD-associated rs704 Affects Vitronectin Expression

Polymorphisms in or around genes can affect transcription or mRNA stability, for example, by disrupting or generating binding sites for transcription factors, or altering mRNA stability [296,297]. Aberrant mRNA expression can be causal for disease development, as in cardiac laminopathy, where a missense mutation in the *LMNA* gene by altering the splicing process causes nonsense-mediated mRNA decay and reduced expression of lamin, an architectural protein of the cell nucleus, leading to arrhythmic disturbances and severe cardiomyopathy [298]. Here, semi-quantitative sequencing of vitronectin cDNA from hiPSC-RPE cells and human retinal tissues heterozygous for rs704 revealed no effect of this polymorphism on *VTN* transcriptional activity. These results are consistent with data from the Genotype-Tissue Expression (GTEx) project, which revealed no effect of rs704 on vitronectin mRNA expression in 49 different (non-retinal) healthy tissues (e.g., whole blood, arterial tissue, and brain tissue) from 838 post-mortem donors [299].

In contrast, heterologous vitronectin expression revealed a significant effect of rs704 on vitronectin protein expression and secretion, in specific a strong increase in protein levels of the AMD risk-associated VTN_rs704:T isoform compared to the non-AMD-associated VTN_rs704:C. In line with these experiments, an increase in vitronectin plasma levels was described to be associated with the rs704 risk variant in a large human plasma proteome analysis including 3,301 healthy participants [243]. Consequently, rs704 was classified as a pQTL [243]. The mechanism by which rs704 affects protein quantity of vitronectin were not investigated within this study but may be explained, for example, by codon usage bias (the preference for certain synonymous codons), which can influence translation kinetics [300,301]. The methionine encoding triplet codon AUG (adenine–uracil–guanine, found in the risk allele) has a higher frequency than the threonine encoding triplet codon ACG (adenine–cytosine–guanine, found in the non-risk allele), specifically 22.3 in 1000 compared to 6.2 in 1000 [302]. As frequent codons have a higher abundance of their corresponding tRNA [300,301], the higher availability of the AUG codon tRNA could therefore lead to an increased translation of VTN_rs704:T resulting in increased protein levels. Similarly, in a study on the expression of the small GTPase KRas protein, the progressive replacement of rare codons with common codons led to increases in KRas expression at both transcriptional and translational levels [303]. Furthermore, protein folding was shown to be affected by translation kinetics [304]. Moreover, rs704:C>T induces an exchange from a polar (threonine) to an unpolar amino acid (methionine) in vitronectin. Thus, alterations in translation velocity or amino acid composition could affect protein folding and translocation from the endoplasmic reticulum to the Golgi apparatus or protein retention in the Golgi [305,306]. For example, the rs704-dependent amino acid exchange may affect the ability of vitronectin to interact with lipids and phospholipids in the Golgi bilayer, resulting in an altered escape from the Golgi vesicles. A similar scenario has been reported as a consequence of missense mutations within the N-terminal transmembrane domain of the protein GlcNAc-1-phosphotransferase [307]. Alternatively, increased protein levels of VTN_rs704:T might be a consequence of changes in protein stability. The effect of rs704 on vitronectin folding and processing was described before [237,238] and could affect the susceptibility of the protein for degrading enzymes or stress-induced denaturation, as observed in the case of arrhythmogenic right ventricular cardiomyopathy (ARVC), where the C796R missense mutation dramatically affects the folding of the plakophilin-2 (PKP2) protein, a component of the cardiac desmosome, resulting in altered proteolytic degradation by calpain proteases and thus in the amount of PKP2 [308].

5.2   AMD-associated rs704 Affects Vitronectin Processing

After heterologous expression, the non-AMD risk-associated isoform VTN_rs704:C appeared as a mixture of single and cleaved forms, while the AMD risk-associated VTN_rs704:T isoform was less susceptible to proteolytic cleavage and was expressed predominantly in its

intact single-chain form. These results confirm previous findings reporting a correlation between plasma vitronectin processing and rs704-induced amino acid exchange T400M [237,238]. Further analysis of vitronectin processing revealed that the difference in the susceptibility to endoproteolytic cleavage of the two vitronectin isoforms is limited to furin-mediated proteolysis, while plasmin-mediated proteolysis at aa 380 was not affected. Although the amino acid change caused by rs704 in aa 400 does not disrupt the furin recognition sequence (RXXR, furin minimal consensus motif) [309] involving aa 395-398, it is localized only 2 amino acid residues apart. It might thus trigger conformational changes in its vicinity that mask the furin recognition sequence, which could result in the observed reduced cleavage of VTN_rs704:T by furin. In consistence with this assumption, Chain and colleagues observed that rs704 induces structural rearrangements in vitronectin. Specifically, they showed that protein kinase A phosphorylates the single-chain but not the two-chain form of vitronectin, due to burial and inaccessibility of the phosphorylation site in the cleaved, two-chain form of the protein [239,241]. In contrast, the plasmin cleavage site is located at aa 380 [257] and is obviously not affected by the rs704-mediated amino acid change and/or associated structural changes. In agreement with this, no effect of rs704 on the stability and multimerization of vitronectin was observed, which would indicate that the two vitronectin isoforms share similar biophysical properties. However, a detailed analysis of sequence variability by high-resolution techniques, such as nuclear magnetic resonance [310], or biophysical analyses such as circular dichroism [311] or differential scanning fluorimetry [312] could be helpful to compare the two isoforms of vitronectin and further verify the effect of rs704 on the protein structural conformation and stability.

5.3 AMD-associated rs704 Affects Vitronectin Binding to Cell Surfaces

Cell-binding experiments demonstrated that the AMD-associated VTN_rs704:T isoform has a reduced ability to bind cell surfaces compared to the non-AMD-associated VTN_rs704:C isoform. Again, these differences may be explained by local structural alterations initiated by rs704-related amino acid change at aa 400. Specifically, it has been reported that vitronectin interacts with cell surface glycosaminoglycans and proteoglycans through its heparin-binding site [200,313,314], which is located within the third variable region of vitronectin at the C-terminus. This region also hosts the rs704 polymorphism encompassing amino acid 400 [195]. The rs704-related amino acid change or the altered proteolytic cleavage of vitronectin, may induce different local conformational rearrangements of the protein within or near the heparin-binding domain, thereby affecting the ability of vitronectin to bind cell surfaces. Alternatively, vitronectin cell binding could be mediated by interaction with urokinase and integrin receptors *via* vitronectin-binding sites located at the N-terminal SMD and the RGD domains, respectively [187,191], as well as with sulphated lipids and phospholipid lipids *via* the hemopexin domains of the protein [174]. Although these binding domains are relatively distant from the

rs704 site, it cannot be excluded that they may be structurally influenced by distal conformational changes of the vitronectin protein.

Altered cellular binding could significantly disrupt both the vitronectin-mediated physical anchoring of cells to the ECM and the regulation of receptor activation, resulting in changes in cell morphology, migration and signal transduction underlying cellular processes such as, for example, angiogenesis [213,221,315]. An imbalance in these processes could potentially contribute to the pathobiology of AMD.

5.4 Vitronectin is Implicated in AMD-associated Processes

To investigate the functional differences of non-AMD risk-associated VTN_rs704:C and AMD risk-associated VTN_rs704:T and the putative contribution of vitronectin to AMD pathogenesis, the two isoforms of vitronectin were compared in their ability to regulate several cellular processes also implicated in AMD, in particular cell autophagy, viability, adhesion, migration and angiogenesis, as well as activation of ERK signalling [209,234,272,316]. These functional investigations involved cultured RPE and vascular endothelial cells, as dysfunction of these cell types *in vivo* has been observed in AMD [317,318]. Furthermore, in the retina, vitronectin protein was localised mainly within Bruch's membrane and the endothelium of chorioretinal vessels [165].

Despite previous studies suggesting regulation of autophagy or cell viability by vitronectin and/or vitronectin receptors [319-322], the functional experiments conducted in this thesis failed to show an effect of vitronectin on autophagy or cell viability. This might be attributed to the experimental approaches adopted in the present work, e.g., the time frames of exposure to vitronectin, the use of purified recombinant vitronectin in solution here instead of a uniformly distributed vitronectin coating on which the cells are seeded used in the literature cited, as well as the level and the type of cell stress induced (treatment with hydrogen peroxide here vs. ischaemic-reperfusion approaches or radiation exposure mainly used in the literature cited above). Moreover, these *in vitro* experiments do not exclude that vitronectin regulates these processes *in vivo*. Further experiments are required to elucidate the involvement of vitronectin in the regulation of these processes in the retina.

As part of the mitogen-activated protein kinase (MAPK) family, the ERK pathway mediates many aspects of RPE and endothelium homeostasis, including cell adhesion, proliferation, and production of angiogenic factors such as VEGF [323-327]. Furthermore, ERK dysregulation was implicated in the pathogenesis of AMD [271,316] Specifically, the ERK signalling pathway is activated during AMD development. A comparison of transcriptomes from samples of normal human RPE-choroid and AMD-affected RPE-choroid demonstrated the activation of several signalling pathways, including ERK in AMD cases [328]. Also, human eyes with GA-AMD have shown activation of ERK that promotes RPE cell death [271]. In this thesis, the non-AMD risk-associated vitronectin isoform (VTN_rs704:C) induced a statistically significant reduction in

ERK1/2 phosphorylation/activation in cultured RPE cells. A similar, though not statistically significant, effect was observed with the risk-associated VTN_rs704:T isoform. This would suggest a role for this protein as a negative regulator of ERK activation in RPE cells with implications for the pathogenesis of AMD. Alterations in the inhibitory effect of vitronectin due to the rs704 risk variant (e.g., through increased vitronectin expression or reduced ability to bind cell surfaces) could alter the regulation of vitronectin-mediated ERK activation, causing an imbalance in ERK-mediated processes. Since ERK activation regulates both cell survival and apoptosis [329,330], imbalances may favour cell death. Similarly, ERK-regulated cellular processes, such as cell adhesion, proliferation, and VEGF production [323-327] could be altered due to a potential rs704 risk variant-associated dysregulation of ERK signalling by vitronectin. In contrast, no effect of vitronectin isoforms on ERK regulation was observed in HUVECs, which is apparently in disagreement with previous findings [331,332]. Specifically, Jin and colleagues observed ERK activation after 5 and 10 min of HUVEC treatment with vitronectin. However, this activation gradually decreased over the subsequent 60 min. The authors hypothesised that such a stimulation may lead to the expression of the transcription factor AP-1 and of metalloproteinase MMP-9, which in turn play important roles in the later stages of angiogenesis [331]. In contrast, in HUVEC cells exposed to damaging radiation, vitronectin induced a suppression of ERK signalling with inhibition of radiation-induced p21 expression and subsequent protection of the cells from apoptosis [332]. It becomes evident that the effect of vitronectin *in vitro* is strongly influenced by the experimental conditions applied. Therefore, the concentration of recombinant vitronectin used in this study (1.5 µg/ml here vs. 10 or 50 µg/ml in the studies cited above) and the incubation time (24 h here vs. 5 to 60 min in the studies cited above) may have been unfavourable for the detection of a vitronectin-related effect. Together with the divergent literature available, the interpretation of the data obtained in this thesis remains difficult.

While the cell binding capacities of VTN_rs704:C and VTN_rs704:T showed significant differences, the two vitronectin isoforms exerted similar effects in cellular adhesion. Both vitronectin isoforms induced a strong binding of hiPSC-RPE and porcine RPE cells but did not affect adhesion to HUVECs. The apparent discrepancy between the effect on cell binding and adhesion could be explained by the fact that cell-binding assays reveal a physical interaction between vitronectin and cell membrane, which can be mediated by several cell surface molecules, such as lipids, various receptors, or heparin [174,178,187,191,213,313,314]. In contrast, adhesion is a cellular process involving the formation of specialized structures of multi-protein complexes built by cell adhesion molecules or receptors, ECM proteins and cytoplasmic plaques or peripheral membrane proteins [333,334]. Although stimulation of adhesion is a well-known property of vitronectin, which is consequently also frequently used as an adhesive for cells in culture [335,336], in adhesion experiments with purified recombinant

vitronectin, the two vitronectin isoforms only stimulated adhesion of RPE cells but not of HUVECs. This could be explained by the interaction of vitronectin with PAI-1, a known angiogenic regulator and vitronectin binding partner [287,337]. As shown in this thesis and other studies [338-340], HUVECs produce high amounts of PAI-1, to a much higher extent than ARPE-19 cells. Due to the proximity of the binding sites for PAI-1 and integrin/urokinase adhesion receptors on vitronectin, the binding of PAI-1 to vitronectin likely interferes with vitronectin-mediated cell adhesion through HUVEC cell surface receptors [188,227,228,341]. Conversely, ECMs containing VTN_rs704:C or VTN_rs704:T increased the adhesion of all cell lines tested including HUVECs. The increased attachment of HUVECs to the vitronectin-containing ECM could result from the compensation of the antagonistic effect of PAI-1 by other ECM components, such as collagen or fibronectin, which are alternative ECM cell-binding elements, and which, in this thesis, showed increased extracellular deposition by vitronectin-expressing cells (see following section 5.5).

Cell adhesion to vitronectin leads to the activation of integrin αvβ3 and enhances the activation of VEGFR-2 receptor by VEGF [342-345]. Furthermore, vitronectin increases the angiogenic activity of VEGF by direct binding [221]. This would allow vitronectin to positively regulate capillary formation and endothelial cell migration. However, migration and tube-formation assays performed within this thesis, showed that VTN_rs704:C slightly reduced HUVEC migration, and both isoforms decreased tubulogenesis by HUVECs. The antagonistic binding of PAI-1 to vitronectin could again explain this observed slight anti-angiogenic effect of vitronectin. As reported in several independent studies [228,346,347], pro-angiogenic activity of vitronectin can be impaired by PAI-1 which blocks vitronectin binding to the integrin receptor. Alternatively, the anti-angiogenic effect of vitronectin could be a consequence of its glycation profile [348]. Wang and colleagues demonstrated that advanced glycation of vitronectin (present after hyperglycaemia and in diabetes mellitus) inhibits VEGF-induced VEGFR-2 activation by uncoupling the VEGFR-2-αvβ3 integrin crosstalk, resulting in reduced endothelial cell migration and vessel growth [348]. Recombinant proteins produced in mammalian expression systems are often considered identical, or at least very similar, to the native protein. However, differences in the glycan structures of specific proteins expressed in various mammalian cell lines have been reported [349], which could, similarly to that described by Wang and colleagues, contribute to the anti-angiogenic effect of vitronectin. Finally, an indirect anti-angiogenic function attributed to vitronectin could be responsible for the observed anti-angiogenic effect. Yi and colleagues [350] reported that the presence of vitronectin supports the anti-angiogenic activity of substances such as osteonectin or angiostatin. This class of angiogenic inhibitors is derived from ECM and plasma proteins through proteolysis or other modifications and as such could potentially be a constituent of the matrices or media used during the experiments.

5.5   Vitronectin Induces Changes in ECM Resembling Those Associated with AMD

After heterologous expression in ARPE-19 cells for 4 weeks, vitronectin was deposited in the ECM in the form of large clusters, with a stronger extracellular accumulation of the AMD risk-associated VTN_rs704:T isoform compared to the non-AMD risk-associated VTN_rs704:C. This result is in line with the stronger expression of VTN_rs704:T than VTN_rs704:C observed in this and other studies [243].

Interestingly, the presence of the two vitronectin isoforms in the ECM increased deposition and clustering of main structural ECM constituents, such as fibronectin, collagens, and elastin, also with a stronger effect of VTN_rs704:T than VTN_rs704:C. Vitronectin is known to interact with many ECM components, e. g. heparin, glycosaminoglycans, and collagens [351-353]. Larger amounts of deposited vitronectin might therefore bind larger amounts of collagen, possibly leading to the observed collagen aggregation at the vitronectin deposition site. In line with this, it has recently been reported that vitronectin accelerates collagen fibril formation and morphological changes by binding to collagen under neutral conditions [354]. Interestingly, in this study, an alternative mechanism was uncovered by which vitronectin would increase collagen in the matrix, namely by binding to and inhibiting the activity of cathepsin K, which is responsible for collagen degradation [354]. Collagen, in turn, interacts with fibronectin and stimulates the formation of a stable fibronectin network [355-358]. Increased collagen deposition might thus explain the observed increase in fibronectin in matrices containing vitronectin. Alternatively, vitronectin can directly influence fibronectin deposition. As described by Pankov and colleagues [359], it may enhance fibronectin polymerisation into fibrillar structures through binding to the α5β1 integrin receptor. However, this hypothesis is less well established, as *in vitro* studies have also shown that vitronectin can inhibit fibronectin deposition in the ECM [360-363]. Fibronectin in turn is reported to bind elastin [364] and promote its deposition, which can explain the increase in elastin deposition in vitronectin-containing matrices as observed in this thesis. With ageing and particularly during AMD development, the structure of Bruch's membrane undergoes changes including calcification and increased stiffness [210]. The accumulation of structural elements, mainly collagen, and their cross-linking contribute to an increase in Bruch's membrane thickness and worsens diffusion of nutrients and waste to and from the retina, affecting RPE metabolism and drusogenesis [89,210,365]. The observed ability of vitronectin to increase the deposition and clustering of ECM structural constituents, may suggest a potential contribution of vitronectin and rs704 in AMD-associated ECM structural alterations. In line with this, recent evidence suggested that vitronectin is the coordinator of calcium mineralisation in AMD-associated extracellular sub-RPE deposits [202].

The ECM of ARPE-19 cells containing vitronectin isoforms also revealed an increase in complement components C9 and CFH. This appears of considerable biological interest since

dysregulation of the complement system is a significant driver of AMD pathogenesis [134], and AMD-associated deposits also contain components of the complement pathway, including C9 and CFH [40,41,47,366]. Vitronectin is a well-established binding partner of C9 [196,203,367,368] which could explain the increase of C9 in ECMs containing vitronectin isoforms. Alternatively, the expression of C9 and CFH may be altered by vitronectin-induced changes in the ECM. Indeed, it has previously been reported that structural changes in the ECM significantly affect gene expression and protein secretion profiles of the RPE, especially concerning components of complement or growth factors, including VEGF and PEDF [101,134,369]. Of note, CFH and its truncated isoforms are the main negative complement regulators that binds ECM, including Bruch's membrane, to prevent excessive complement activation and inflammation [370-372] Interestingly, analysis of the ECM deposited by ARPE-19 also showed a positive correlation between deposition of vitronectin isoforms and VEGF accumulation. In primary human RPE cells, CFH synthesis was shown to be stimulated by VEGF [373], thus increased VEGF may also be causative for the enhanced deposition of CFH observed in vitronectin-containing matrixes.

In addition to its expression being influenced by alterations in the ECM, localisation and function of the angiogenesis-stimulating factor VEGF are closely dependent on its binding to ECM components [106,374,375], including vitronectin, which in its multimeric form binds VEGF [221]. The direct binding of VEGF to vitronectin could explain VEGF increase in the vitronectin-containing matrices deposited by ARPE-19. Alternatively, the increase in matrix-bound VEGF can also be attributed to an increase in the deposition of other components of the ECM capable of binding VEGF in the vitronectin-containing matrices, such as fibronectin which was shown to directly interact with VEGF [376,377].

Taken together, the observed alterations in ECM composition could contribute to a disturbance of the pro- and anti-angiogenic balance that, in AMD, seems to be triggered by changes in Bruch's membrane, together with complement system hyperactivity and inflammatory responses [210]. This finding would support a novel role for vitronectin in the pathobiology of AMD beyond its acknowledged involvement in AMD-associated deposit formation [166,202].

5.6 Vitronectin and PAI-1 Interaction may Contribute to Vascular Complications in AMD

The interaction of vitronectin with angiogenic regulator PAI-1 is among the best-characterised physical interaction of vitronectin with extracellular proteins [185,287,288]. As a member of the serine protease inhibitor (serpin) superfamily with anti-protease activity, PAI-1 is the main physiological inhibitor of tissue-type (tPA) and urokinase-type (uPA) plasminogen activators. Besides being crucially involved in fibrinolysis and wound healing, PAI-1 plays a key role in various acute and chronic pathophysiological processes, including those involving

vascular complications in AMD [289-291,337]. Indeed, PAI-1 regulates a variety of angiogenesis-related processes, including pericellular proteolysis, cell migration, adhesion, and reattachment [378-380]. Its half-life is closely dependent on its binding to vitronectin, which through allosteric modulation stabilizes the active state of PAI-1 by slowing its conversion to an inactive state [226].

In this thesis, co-precipitation experiments showed that the AMD risk-associated VTN_rs704:T isoform bound stronger to PAI-1 than the non-AMD risk-associated VTN_rs704:C. This contrasts with findings of Gibson and colleagues, who suggest that rs704 has no impact on vitronectin binding to PAI-1 [208]. Their study, however, used a truncated version of VTN_rs704:C, lacking the short-chain peptide of the rs704-dependent protein cleavage product, which *in vivo* remains bound to the protein by disulphide bonds [381,382] and probably affects its folding or accessibility to PAI-1. Similarly, rs704-related amino acid change (T400M), which causes altered folding and processing of vitronectin [237,239] may affect the accessibility of the interaction site with PAI-1 and result in stronger binding of VTN_rs704:T to PAI-1. Alternatively, since the binding of vitronectin to PAI-1 results in the incorporation of vitronectin monomers into a higher-order complex [383,384], the differences between the two vitronectin isoforms in their binding to PAI-1 could also reflect a different promotion of self-association of the two vitronectin isoforms by PAI-1. This could result in a difference in the number of vitronectin monomers complexed and thus retained by immobilised PAI-1.

While the two isoforms differed in their ability to bind PAI-1, they showed no difference in their capacity to stabilize the active state of PAI-1. This apparent discrepancy could be attributable by the different experimental approaches. The co-precipitation assay measures the stable physical interaction between vitronectin and PAI-1. In contrast, the enzymatic assay measures the capacity of vitronectin to stabilize the active form of PAI-1. It was described before that a stable interaction between two biomolecules is not necessarily a requirement for enzymatic processes. For example, rhomboid proteases cleave their substrate very efficiently without showing apparent binding affinity [385]. Similarly, stable binding between vitronectin and PAI-1 may not be relevant for the stabilization of active PAI-1 and the enzymatic assay may thus also detect less stable, unstable, or perhaps even transient interactions. Alternatively, different sensitivities of the two experimental approaches or a saturation effect in the enzyme assay may explain the apparently conflicting results.

In this thesis, the addition of recombinant isoforms of vitronectin significantly increased the expression of PAI-1 protein in HUVECs and ARPE-19 cells and their ECM. Consistently, Preissner and colleagues showed that vitronectin from cultivation medium associates with HUVEC-deposited ECM, where it represents the main binding component for PAI-1 [386]. Furthermore, increased deposition of endothelial PAI-1 by human umbilical artery endothelial

cells (HUAECs) and HUVECs cultured on vitronectin-coated surfaces, compared to other ECM substrates, was reported [387,388]. In this thesis, there was a similar trend towards an increase in PAI-1 protein level in cells and ECM after exposure to VTN_rs704:T compared to VTN_rs704:C, although this was not statistically significant. Since PAI-1 transcription in HUVECs remained unchanged after vitronectin exposure, the increase in the amount of PAI-1 protein could be attributed to posttranslational processes rather than to increased expression. A mechanism by which vitronectin prevents PAI-1 degradation has been described in cultured blood monocytes [389]: When bound to vitronectin, active PAI-1 undergoes a conformational change that makes it less accessible to proteolytic enzymes. In addition, the observed increase of ECM-bound PAI-1 in the presence of vitronectin could also be explained by the ability of vitronectin to translocate PAI-1 into the ECM [390]. Furthermore, it has been reported that active PAI-1 is internalised when complexed with uPA *via* receptor-mediated endocytosis [389,391]. Since vitronectin stabilises the active PAI-1 conformation, this could explain the increase in the cellular amounts of PAI-1 after incubation of HUVECs with vitronectin. Finally, the increase in extracellular amounts of PAI-1 promoted by vitronectin-mediated proteolytic protection [389] could also lead to increased binding of PAI-1 to the cell surface of HUVECs, e.g., *via* the low-density lipoprotein receptor-related protein (LRP) [389,392], again explaining the increased amounts of PAI-1 in the cellular fractions of HUVECs in this study.

In various pathologies, including cellular necrosis and inflammation, fibrosis, and vascular atherosclerosis [393-397], PAI-1 and vitronectin localise and act together at the sites of injury. In the retina, vitronectin might concentrate and coordinate local PAI-1 in the vicinity of endothelial and RPE cells. In addition, vitronectin could potentially be a vehicle for PAI-1 from the bloodstream, given that PAI-1 in blood mainly circulates in a complex with plasma vitronectin [287,398]. Specifically, due to vitronectin transcytosis by vascular endothelial cells [399], vitronectin could direct complexed PAI-1 from the bloodstream into the subendothelial matrix as well as into the extracellular space adjacent to the RPE. The extent of the translocation of PAI-1 into the ECM by vitronectin may depend on the rs704 genotype: As a result of its high concentration and/or the increased ability to bind PAI-1 observed in this thesis, the AMD-associated isoform of vitronectin could further promote the amount of PAI-1 in the ECM and broaden the spectrum of its activity in AMD. Altered retinal concentrations of PAI-1 can simultaneously result in alterations of ECM proteolysis [224]. The prevention of ECM degradation, exerted through PAI-1 inhibition of uPA proteolytic activity, could be inappropriately sustained by increased levels of PAI-1 with an impairment of balance between ECM synthesis, degradation, and turnover. This could lead to stiffness of the ECM in both the perivascular microenvironment and Bruch's membrane and create a hypoxic stimulus that could initiate/worsen cellular and extracellular defects associated with AMD,

including abnormal neovascularisation [211,400,401]. Similar changes were reported in transgenic mice that overexpress human PAI-1 in retinal microvasculature [402]. In this context, hypoxia may also result from excessive inhibition of fibrinolysis associated with elevated PAI-1 levels [402], which by contributing to transient narrowing of the retinal capillary lumen [402] may induce microvascular dysfunction and ischemia potentially causing neovascularization in AMD [401,403,404]. Excessive inhibition of PAI-1-dependent ECM degradation and turnover could also explain the above-discussed general increase in ECM deposition observed in the presence of vitronectin. In addition to exacerbated PAI-1 anti-protease activity, a vitronectin-dependent increased concentration of PAI-1 may alter any of the cellular events controlled by this protein and involving cell surface receptors, such as cell attachment, migration, proliferation, angiogenesis as well as regulation of related intracellular signalling [213,405,406]. In line with this, it has been discussed that in excess of PAI-1, the vitronectin matrix remains saturated with PAI-1 resulting in an impasse of integrin-mediated vascular cell adhesion [407].

Together with previous reports on the mutual involvement of PAI-1 and vitronectin in angiogenesis [341,408] and neointima formation [397], the results of this thesis would support a role of this protein interaction in the vascular complications of AMD. PAI-1 per se has already been reported in the pathogenesis of neovascular AMD [289-291].

Interestingly, the refinement of the association analysis of rs704 with clinical subtypes of AMD in the IAMDGC dataset, performed in a collaboration with Dr. Christina Kiel (Institute of Human Genetics, University of Regensburg), revealed that the association of rs704 with advanced AMD only exist with the neovascular subtype [292]. This supports a new potential role for vitronectin in the pathogenesis of AMD, not only limited to the formation of drusen or subretinal drusenoid deposits.

Finally, the rs704 risk genotype-dependent increase in the concentration of vitronectin (and the associated PAI-1) can be aggravated by age-dependent alterations in gene expression. A large-scale gene expression analysis conducted in a collaboration with Dr. Tobias Strunz (Institute of Human Genetics, University of Regensburg) revealed a statistically significant increase in *VTN* and *PAI-1* mRNA expression in blood samples and retinal tissues from healthy donors aged 60 years and older [292]. Furthermore, this analysis showed a positive correlation between *VTN* and *PAI-1* gene expression, which suggests that the two genes are subject to similar mechanisms of transcriptional regulation, possibly influenced by ageing [292].

5.7 Conclusion: rs704-related AMD Disease Model and Its Clinical Implication

In conclusion, the results of this thesis further provide support for the involvement of vitronectin in the pathogenesis of AMD but also highlight possible new pathways through which this protein could contribute to AMD development and progression. The presented findings suggest a conceptual disease model for AMD (**Figure 36**), according to which the rs704 risk genotype, in combination with advanced age, leads to a significant increase in

protein expression of vitronectin in the retina (and in the systemic circulation [243]). This, in turn, could lead to an imbalance in the various cellular and extracellular processes regulated by vitronectin, e. g. a dysregulation in the organisation and turnover of the endothelial basement membrane/Bruch's membrane, in the storage and activity of angiogenic regulators such as VEGF and PAI-1 and, consequently, in cellular processes such as cell adhesion and migration. This altered homeostasis might promote or worsen AMD-associated pathological events, in particular neovascular complications.

In recent years, therapies targeting integrins (including vitronectin receptors) have shown positive results in the treatment of retinovascular disease, and several integrin inhibitors are currently in clinical trials [409,410]. For instance, JNJ-26076713 (Johnson & Johnson) is a potent, orally bioavailable inhibitor of αvβ3 and αvβ5 binding to vitronectin. Treatment with JNJ-26076713 reduced neovascularisation and retinal vascular permeability in an animal model of oxygen-induced retinopathy and is currently undergoing preclinical study. SF-0166 (SciFluor Life Sciences), a small molecule inhibitor of the vitronectin αvβ3 receptor, inhibited cell adhesion to vitronectin and reduce neovascularisation *in vitro* [411], and was already effective in clinical phase 1/2 in reducing retinal thickening and improving visual acuity (https://clinicaltrials.gov/ct2/show/NCT04746963). However, while these molecules appear highly effective, one of their limitations is their poor selectivity, as they often inhibit other non-target αv integrins to varying degrees with possible side effects [410].

Embracing the emerging literature suggesting vitronectin as a promising therapeutic target for the treatment of AMD [202,412], the results of this work would suggest an alternative therapeutic approach in which therapeutic modulation of vitronectin protein expression through genetic or pharmacological approaches could, for example, help restore vascular/retinal homeostasis and prevent its decline in AMD development. Furthermore, as a molecular marker, rs704 can be used to develop clinical prevention studies targeting unique subgroups of people at increased risk of developing AMD. Hence, additional research to fully understand the pathogenicity of vitronectin isoforms and their management could be valuable for the comprehension and treatment of AMD.
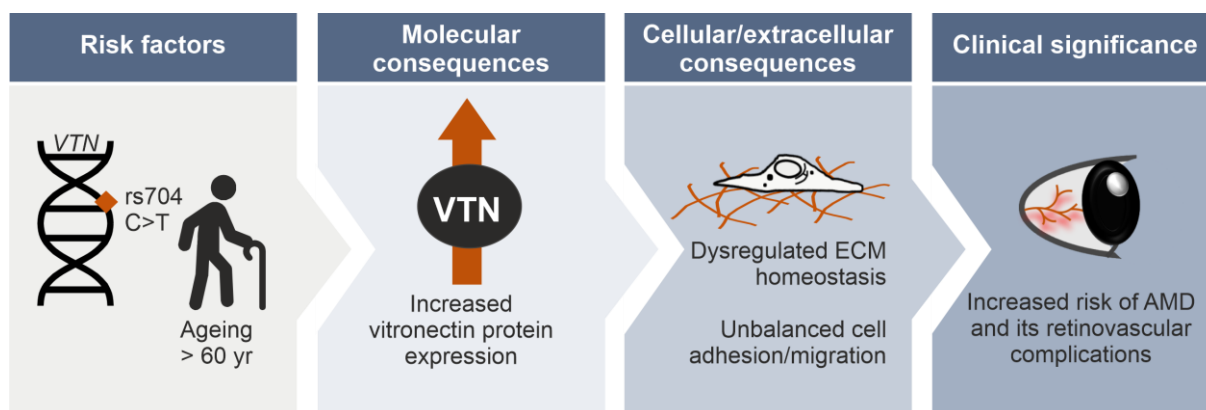
Figure 36: Conceptual disease model of rs704-associated pathobiology contributing to AMD.
(Figure modified from Biasella et al., 2022 [292]).

References

1. Fleckenstein, M. et al. Age-related macular degeneration. Nat Rev Dis Primers 7, 31 (2021).

2. Colijn, J.M. et al. Prevalence of Age-Related Macular Degeneration in Europe: The Past and the Future. Ophthalmology 124, 1753-1763 (2017).

3. Li, J.Q. et al. Prevalence and incidence of age-related macular degeneration in Europe: a systematic review and meta-analysis. Br J Ophthalmol 104, 1077-1084 (2020).

4. Chen, Y., Bedell, M. & Zhang, K. Age-related macular degeneration: genetic and environmental factors of disease. Mol Interv 10, 271-81 (2010).

5. Chew, E.Y. et al. The Age-Related Eye Disease Study 2 (AREDS2): study design and baseline characteristics (AREDS2 report number 1). Ophthalmology 119, 2282-9 (2012).

6. Fritsche, L.G. et al. Age-related macular degeneration: genetics and biology coming together. Annu Rev Genomics Hum Genet 15, 151-71 (2014).

7. Colijn, J.M. et al. Genetic Risk, Lifestyle, and Age-Related Macular Degeneration in Europe: The EYE-RISK Consortium. Ophthalmology 128, 1039-1049 (2021).

8. Effron, D., Forcier, B.C. & Wyszynski, R.E. Funduscopic findings. Knoop K.J., & Stack L.B., & Storrow A.B., & Thurman R(Eds.), The Atlas of Emergency Medicine, 4e. McGraw Hill. https://accessmedicine.mhmedical.com/content.aspx?bookid=1763&sectionid=125433189. (2016).

9. Gupta, M.P., Herzlich, A.A., Sauer, T. & Chan, C.C. Retinal Anatomy and Pathology. Dev Ophthalmol 55, 7-17 (2016).

10. Reichenbach, A. & Bringmann, A. Glia of the human retina. Glia 68, 768-796 (2020).

11. Mannu, G.S. Retinal phototransduction. Neurosciences (Riyadh) 19, 275-80 (2014).

12. Pokorny, J., Lutze, M., Cao, D. & Zele, A.J. The color of night: Surface color perception under dim illuminations. Vis Neurosci 23, 525-30 (2006).

13. Mahabadi, N. & Al Khalili, Y. Neuroanatomy, Retina. in StatPearls (StatPearls Publishing Copyright © 2022, StatPearls Publishing LLC., Treasure Island (FL), 2022).

14. Hubbard, R. & Kropf, A. The action of light on rhodopsin. Proc Natl Acad Sci U S A 44, 130-9 (1958).

15. Zhou, X.E., Melcher, K. & Xu, H.E. Structure and activation of rhodopsin. Acta Pharmacol Sin 33, 291-9 (2012).

16. Ishikawa, M., Sawada, Y. & Yoshitomi, T. Structure and function of the interphotoreceptor matrix surrounding retinal photoreceptor cells. Exp Eye Res 133, 3-18 (2015).

17. Bok, D. & Hall, M.O. The role of the pigment epithelium in the etiology of inherited retinal dystrophy in the rat. J Cell Biol 49, 664-82 (1971).

18. LaVail, M.M. Outer segment disc shedding and phagocytosis in the outer retina. Trans Ophthalmol Soc U K 103 (Pt 4), 397-404 (1983).

19. Yang, S., Zhou, J. & Li, D. Functions and Diseases of the Retinal Pigment Epithelium. Front Pharmacol 12, 727870 (2021).

20. Bok, D. Processing and transport of retinoids by the retinal pigment epithelium. Eye (Lond) 4 (Pt 2), 326-32 (1990).

21. Flannery, J.G., O'Day, W., Pfeffer, B.A., Horwitz, J. & Bok, D. Uptake, processing and release of retinoids by cultured human retinal pigment epithelium. Exp Eye Res 51, 717-28 (1990).

22. Seagle, B.L. et al. Melanin photoprotection in the human retinal pigment epithelium and its correlation with light-induced cell apoptosis. Proc Natl Acad Sci U S A 102, 8978-83 (2005).

23. Kim, I. et al. Constitutive expression of VEGF, VEGFR-1, and VEGFR-2 in normal eyes. Invest Ophthalmol Vis Sci 40, 2115-21 (1999).

24. Boulton, M. & Dayhaw-Barker, P. The role of the retinal pigment epithelium: topographical variation and ageing changes. Eye (Lond) 15, 384-9 (2001).

25. Ford, K.M., Saint-Geniez, M., Walshe, T., Zahr, A. & D'Amore, P.A. Expression and role of VEGF in the adult retinal pigment epithelium. Invest Ophthalmol Vis Sci 52, 9478-87 (2011).

26. Rizzolo, L.J. Development and role of tight junctions in the retinal pigment epithelium. Int Rev Cytol 258, 195-234 (2007).

27. Rizzolo, L.J. Polarity and the development of the outer blood-retinal barrier. Histol Histopathol 12, 1057-67 (1997).

28. Storm, T., Burgoyne, T. & Futter, C.E. Membrane trafficking in the retinal pigment epithelium at a glance. J Cell Sci 133(2020).

29. Curcio, C.A. & Johnson, M. Structure, Function, and Pathology of Bruch's Membrane. In Retina Fifth Edition (Vol. 1, pp. 465-481). Elsevier Inc. https://doi.org/10.1016/B978-1-4557-0737-9.00020-5 (2012).

30. Booij, J.C., Baas, D.C., Beisekeeva, J., Gorgels, T.G. & Bergen, A.A. The dynamic nature of Bruch's membrane. Prog Retin Eye Res 29, 1-18 (2010).

31. Nickla, D.L. & Wallman, J. The multifunctional choroid. Prog Retin Eye Res 29, 144-68 (2010).

32. Fields, M.A., Del Priore, L.V., Adelman, R.A. & Rizzolo, L.J. Interactions of the choroid, Bruch's membrane, retinal pigment epithelium, and neurosensory retina collaborate to form the outer blood-retinal-barrier. Prog Retin Eye Res 76, 100803 (2020).

33. Kur, J., Newman, E.A. & Chan-Ling, T. Cellular and physiological mechanisms underlying blood flow regulation in the retina and choroid in health and disease. Prog Retin Eye Res 31, 377-406 (2012).

34. Díaz-Coránguez, M., Ramos, C. & Antonetti, D.A. The inner blood-retinal barrier: Cellular basis and development. Vision Res 139, 123-137 (2017).

35. Provis, J.M., Penfold, P.L., Cornish, E.E., Sandercoe, T.M. & Madigan, M.C. Anatomy and development of the macula: specialisation and the vulnerability to macular degeneration. Clin Exp Optom 88, 269-81 (2005).

36. Rashid, A. et al. RPE Cell and Sheet Properties in Normal and Diseased Eyes. Adv Exp Med Biol 854, 757-63 (2016).

37. Starnes, A.C. et al. Multi-nucleate retinal pigment epithelium cells of the human macula exhibit a characteristic and highly specific distribution. Vis Neurosci 33, e001 (2016).

38. Jensen, E.G., Jakobsen, T.S., Thiel, S., Askou, A.L. & Corydon, T.J. Associations between the Complement System and Choroidal Neovascularization in Wet Age-Related Macular Degeneration. Int J Mol Sci 21(2020).

39. Ferris, F.L., 3rd et al. Clinical classification of age-related macular degeneration. Ophthalmology 120, 844-51 (2013).

40. Mullins, R.F., Russell, S.R., Anderson, D.H. & Hageman, G.S. Drusen associated with aging and age-related macular degeneration contain proteins common to extracellular deposits associated with atherosclerosis, elastosis, amyloidosis, and dense deposit disease. Faseb j 14, 835-46 (2000).

41. Crabb, J.W. et al. Drusen proteome analysis: an approach to the etiology of age-related macular degeneration. Proc Natl Acad Sci U S A 99, 14682-7 (2002).

42. Wang, L. et al. Abundant lipid and protein components of drusen. PLoS One 5, e10329 (2010).

43. Thompson, R.B. et al. Identification of hydroxyapatite spherules provides new insight into subretinal pigment epithelial deposit formation in the aging eye. Proc Natl Acad Sci U S A 112, 1565-70 (2015).

44. Marshall, G.E., Konstas, A.G., Reid, G.G., Edwards, J.G. & Lee, W.R. Type IV collagen and laminin in Bruch's membrane and basal linear deposit in the human macula. Br J Ophthalmol 76, 607-14 (1992).

45. Green, W.R. & Enger, C. Age-related macular degeneration histopathologic studies. The 1992 Lorenz E. Zimmerman Lecture. Ophthalmology 100, 1519-35 (1993).

46. Curcio, C.A. & Millican, C.L. Basal linear deposit and large drusen are specific for early age-related maculopathy. Arch Ophthalmol 117, 329-39 (1999).

47. Curcio, C.A. Soft Drusen in Age-Related Macular Degeneration: Biology and Targeting Via the Oil Spill Strategies. Invest Ophthalmol Vis Sci 59, Amd160-amd181 (2018).

48. Chen, L., Messinger, J.D., Kar, D., Duncan, J.L. & Curcio, C.A. Biometrics, Impact, and Significance of Basal Linear Deposit and Subretinal Drusenoid Deposit in Age-Related Macular Degeneration. Invest Ophthalmol Vis Sci 62, 33 (2021).

49. Zweifel, S.A., Imamura, Y., Spaide, T.C., Fujiwara, T. & Spaide, R.F. Prevalence and significance of subretinal drusenoid deposits (reticular pseudodrusen) in age-related macular degeneration. Ophthalmology 117, 1775-81 (2010).

50. Curcio, C.A. et al. Subretinal drusenoid deposits in non-neovascular age-related macular degeneration: morphology, prevalence, topography, and biogenesis model. Retina 33, 265-76 (2013).

51. Joachim, N., Mitchell, P., Rochtchina, E., Tan, A.G. & Wang, J.J. Incidence and progression of reticular drusen in age-related macular degeneration: findings from an older Australian cohort. Ophthalmology 121, 917-25 (2014).

52. Steinberg, J.S., Göbel, A.P., Fleckenstein, M., Holz, F.G. & Schmitz-Valckenberg, S. Reticular drusen in eyes with high-risk characteristics for progression to late-stage age-related macular degeneration. Br J Ophthalmol 99, 1289-94 (2015).

53. Bird, A.C., Phillips, R.L. & Hageman, G.S. Geographic atrophy: a histopathological assessment. JAMA Ophthalmol 132, 338-45 (2014).

54. Fleckenstein, M. et al. The Progression of Geographic Atrophy Secondary to Age-Related Macular Degeneration. Ophthalmology 125, 369-390 (2018).

55. Spaide, R.F. et al. Consensus Nomenclature for Reporting Neovascular Age-Related Macular Degeneration Data: Consensus on Neovascular Age-Related Macular Degeneration Nomenclature Study Group. Ophthalmology 127, 616-636 (2020).

56. Nakano, Y. et al. Vascular maturity of type 1 and type 2 choroidal neovascularization evaluated by optical coherence tomography angiography. PLoS One 14, e0216304 (2019).

57. Veritti, D., Sarao, V. & Lanzetta, P. Neovascular age-related macular degeneration. Ophthalmologica 227 Suppl 1, 11-20 (2012).

58. Ambati, J. & Fowler, B.J. Mechanisms of age-related macular degeneration. Neuron 75, 26-39 (2012).

59. Laiginhas, R., Yang, J., Rosenfeld, P.J. & Falcão, M. Nonexudative Macular Neovascularization - A Systematic Review of Prevalence, Natural History, and Recent Insights from OCT Angiography. Ophthalmol Retina 4, 651-661 (2020).

60. Klein, R. et al. Fifteen-year cumulative incidence of age-related macular degeneration: the Beaver Dam Eye Study. Ophthalmology 114, 253-62 (2007).

61. Tikellis, G. et al. Characteristics of progression of early age-related macular degeneration: the cardiovascular health and age-related maculopathy study. Eye (Lond) 21, 169-76 (2007).

62. Kaszubski, P., Ben Ami, T., Saade, C. & Smith, R.T. Geographic Atrophy and Choroidal Neovascularization in the Same Eye: A Review. Ophthalmic Res 55, 185-93 (2016).

63. Sunness, J.S., Gonzalez-Baron, J., Bressler, N.M., Hawkins, B. & Applegate, C.A. The development of choroidal neovascularization in eyes with the geographic atrophy form of age-related macular degeneration. Ophthalmology 106, 910-9 (1999).

64. Ehrlich, R. et al. Age-related macular degeneration and the aging eye. Clin Interv Aging 3, 473-82 (2008).

65. Ruan, Y., Jiang, S. & Gericke, A. Age-Related Macular Degeneration: Role of Oxidative Stress and Blood Vessels. Int J Mol Sci 22(2021).

66. Somasundaran, S., Constable, I.J., Mellough, C.B. & Carvalho, L.S. Retinal pigment epithelium and age-related macular degeneration: A review of major disease mechanisms. Clin Exp Ophthalmol 48, 1043-1056 (2020).

67. Cai, J., Wu, M., Nelson, K.C., Sternberg, P., Jr. & Jones, D.P. Oxidant-induced apoptosis in cultured human retinal pigment epithelial cells. Invest Ophthalmol Vis Sci 40, 959-66 (1999).

68. Panda-Jonas, S., Jonas, J.B. & Jakobczyk-Zmija, M. Retinal pigment epithelial cell count, distribution, and correlations in normal human eyes. Am J Ophthalmol 121, 181-9 (1996).

69. Krohne, T.U., Stratmann, N.K., Kopitz, J. & Holz, F.G. Effects of lipid peroxidation products on lipofuscinogenesis and autophagy in human retinal pigment epithelial cells. Exp Eye Res 90, 465-71 (2010).

70. Hyttinen, J.M.T. et al. DNA damage response and autophagy in the degeneration of retinal pigment epithelial cells-Implications for age-related macular degeneration (AMD). Ageing Res Rev 36, 64-77 (2017).

71. Keeling, E., Lotery, A.J., Tumbarello, D.A. & Ratnayaka, J.A. Impaired Cargo Clearance in the Retinal Pigment Epithelium (RPE) Underlies Irreversible Blinding Diseases. Cells 7(2018).

72. Feeney-Burns, L., Hilderbrand, E.S. & Eldridge, S. Aging human RPE: morphometric analysis of macular, equatorial, and peripheral cells. Invest Ophthalmol Vis Sci 25, 195-200 (1984).

73. Sundelin, S., Wihlmark, U., Nilsson, S.E. & Brunk, U.T. Lipofuscin accumulation in cultured retinal pigment epithelial cells reduces their phagocytic capacity. Curr Eye Res 17, 851-7 (1998).

74. Finnemann, S.C., Leung, L.W. & Rodriguez-Boulan, E. The lipofuscin component A2E selectively inhibits phagolysosomal degradation of photoreceptor phospholipid by the retinal pigment epithelium. Proc Natl Acad Sci U S A 99, 3842-7 (2002).

75. Boulton, M., Dontsov, A., Jarvis-Evans, J., Ostrovsky, M. & Svistunenko, D. Lipofuscin is a photoinducible free radical generator. J Photochem Photobiol B 19, 201-4 (1993).

76. Shamsi, F.A. & Boulton, M. Inhibition of RPE lysosomal and antioxidant activity by the age pigment lipofuscin. Invest Ophthalmol Vis Sci 42, 3041-6 (2001).

77. Yako, T., Otsu, W., Nakamura, S., Shimazawa, M. & Hara, H. Lipid Droplet Accumulation Promotes RPE Dysfunction. Int J Mol Sci 23(2022).

78. Liang, F.Q. & Godley, B.F. Oxidative stress-induced mitochondrial DNA damage in human retinal pigment epithelial cells: a possible mechanism for RPE aging and age-related macular degeneration. Exp Eye Res 76, 397-403 (2003).

79. Brown, E.E., DeWeerd, A.J., Ildefonso, C.J., Lewin, A.S. & Ash, J.D. Mitochondrial oxidative stress in the retinal pigment epithelium (RPE) led to metabolic dysfunction in both the RPE and retinal photoreceptors. Redox Biol 24, 101201 (2019).

80. Byeon, S.H. et al. Vascular endothelial growth factor as an autocrine survival factor for retinal pigment epithelial cells under oxidative stress via the VEGF-R2/PI3K/Akt. Invest Ophthalmol Vis Sci 51, 1190-7 (2010).

81. Klettner, A. Oxidative stress induced cellular signaling in RPE cells. Front Biosci (Schol Ed) 4, 392-411 (2012).

82. Farjood, F. & Vargis, E. Physical disruption of cell-cell contact induces VEGF expression in RPE cells. Mol Vis 23, 431-446 (2017).

83. Chae, J.B. et al. Targeting senescent retinal pigment epithelial cells facilitates retinal regeneration in mouse models of age-related macular degeneration. Geroscience 43, 2809-2833 (2021).

84. Feeney-Burns, L. & Ellersieck, M.R. Age-related changes in the ultrastructure of Bruch's membrane. Am J Ophthalmol 100, 686-97 (1985).

85. Zarbin, M.A. Current concepts in the pathogenesis of age-related macular degeneration. Arch Ophthalmol 122, 598-614 (2004).

86. Hewitt, A.T., Nakazawa, K. & Newsome, D.A. Analysis of newly synthesized Bruch's membrane proteoglycans. Invest Ophthalmol Vis Sci 30, 478-86 (1989).

87. Curcio, C.A., Millican, C.L., Bailey, T. & Kruth, H.S. Accumulation of cholesterol with age in human Bruch's membrane. Invest Ophthalmol Vis Sci 42, 265-74 (2001).

88. Ramrattan, R.S. et al. Morphometric analysis of Bruch's membrane, the choriocapillaris, and the choroid in aging. Invest Ophthalmol Vis Sci 35, 2857-64 (1994).

89. Karwatowski, W.S. et al. Preparation of Bruch's membrane and analysis of the age-related changes in the structural collagens. Br J Ophthalmol 79, 944-52 (1995).

90. Moore, D.J., Hussain, A.A. & Marshall, J. Age-related variation in the hydraulic conductivity of Bruch's membrane. Invest Ophthalmol Vis Sci 36, 1290-7 (1995).

91. Dallinger, S. et al. Age dependence of choroidal blood flow. J Am Geriatr Soc 46, 484-7 (1998).

92. Wakatsuki, Y., Shinojima, A., Kawamura, A. & Yuzawa, M. Correlation of Aging and Segmental Choroidal Thickness Measurement using Swept Source Optical Coherence Tomography in Healthy Eyes. PLoS One 10, e0144156 (2015).

93. Xu, H., Chen, M. & Forrester, J.V. Para-inflammation in the aging retina. Prog Retin Eye Res 28, 348-68 (2009).

94. Ardeljan, D. & Chan, C.C. Aging is not a disease: distinguishing age-related macular degeneration from aging. Prog Retin Eye Res 37, 68-89 (2013).

95. Kamei, M. & Hollyfield, J.G. TIMP-3 in Bruch's membrane: changes during aging and in age-related macular degeneration. Invest Ophthalmol Vis Sci 40, 2367-75 (1999).

96. Hussain, A.A., Lee, Y., Zhang, J.J. & Marshall, J. Disturbed matrix metalloproteinase activity of Bruch's membrane in age-related macular degeneration. Invest Ophthalmol Vis Sci 52, 4459-66 (2011).

97. Yu, Y. et al. Common variants near FRK/COL10A1 and VEGFA are associated with advanced age-related macular degeneration. Hum Mol Genet 20, 3699-709 (2011).

98. García-Onrubia, L. et al. Matrix Metalloproteinases in Age-Related Macular Degeneration (AMD). Int J Mol Sci 21(2020).

99. Totan, Y. et al. Oxidative macromolecular damage in age-related macular degeneration. Curr Eye Res 34, 1089-93 (2009).

100. Venza, I., Visalli, M., Cucinotta, M., Teti, D. & Venza, M. Association between oxidative stress and macromolecular damage in elderly patients with age-related macular degeneration. Aging Clin Exp Res 24, 21-7 (2012).

101. Fernandez-Godino, R. Alterations in Extracellular Matrix/Bruch's Membrane Can Cause the Activation of the Alternative Complement Pathway via Tick-Over. Adv Exp Med Biol 1074, 29-35 (2018).

102. Feher, J. et al. Mitochondrial alterations of retinal pigment epithelium in age-related macular degeneration. Neurobiol Aging 27, 983-93 (2006).

103. Blasiak, J. & Szaflik, J.P. DNA damage and repair in age-related macular degeneration. Front Biosci (Landmark Ed) 16, 1291-301 (2011).

104. Blasiak, J., Synowiec, E., Salminen, A. & Kaarniranta, K. Genetic variability in DNA repair proteins in age-related macular degeneration. Int J Mol Sci 13, 13378-97 (2012).

105. Golestaneh, N., Chu, Y., Xiao, Y.Y., Stoleru, G.L. & Theos, A.C. Dysfunctional autophagy in RPE, a contributing factor in age-related macular degeneration. Cell Death Dis 8, e2537 (2017).

106. Ferrara, N. Binding to the extracellular matrix and proteolytic processing: two key mechanisms regulating vascular endothelial growth factor action. Mol Biol Cell 21, 687-90 (2010).

107. Marneros, A.G. Increased VEGF-A promotes multiple distinct aging diseases of the eye through shared pathomechanisms. EMBO Mol Med 8, 208-31 (2016).

108. Aiello, L.P. et al. Vascular endothelial growth factor in ocular fluid of patients with diabetic retinopathy and other retinal disorders. N Engl J Med 331, 1480-7 (1994).

109. Shahidatul-Adha, M., Zunaina, E. & Aini-Amalina, M.N. Evaluation of vascular endothelial growth factor (VEGF) level in the tears and serum of age-related macular degeneration patients. Sci Rep 12, 4423 (2022).

110. Lutty, G., Grunwald, J., Majji, A.B., Uyama, M. & Yoneya, S. Changes in choriocapillaris and retinal pigment epithelium in age-related macular degeneration. Mol Vis 5, 35 (1999).

111. Xu, W. et al. Association of risk factors for choroidal neovascularization in age-related macular degeneration with decreased foveolar choroidal circulation. Am J Ophthalmol 150, 40-47.e2 (2010).

112. Boltz, A. et al. Choroidal blood flow and progression of age-related macular degeneration in the fellow eye in patients with unilateral choroidal neovascularization. Invest Ophthalmol Vis Sci 51, 4220-5 (2010).

113. Friedman, E. A hemodynamic model of the pathogenesis of age-related macular degeneration. Am J Ophthalmol 124, 677-82 (1997).

114. Gelfand, B.D. & Ambati, J. A Revised Hemodynamic Theory of Age-Related Macular Degeneration. Trends Mol Med 22, 656-670 (2016).

115. Patel, M. & Chan, C.C. Immunopathological aspects of age-related macular degeneration. Semin Immunopathol 30, 97-110 (2008).

116. Anderson, D.H. et al. The pivotal role of the complement system in aging and age-related macular degeneration: hypothesis re-visited. Prog Retin Eye Res 29, 95-112 (2010).

117. Mullins, R.F. et al. Is age-related macular degeneration a microvascular disease? Adv Exp Med Biol 801, 283-9 (2014).

118. Klein, R.J. et al. Complement factor H polymorphism in age-related macular degeneration. Science 308, 385-9 (2005).

119. Fritsche, L.G. et al. A large genome-wide association study of age-related macular degeneration highlights contributions of rare and common variants. Nat Genet 48, 134-43 (2016).

120. Bhutto, I. & Lutty, G. Understanding age-related macular degeneration (AMD): relationships between the photoreceptor/retinal pigment epithelium/Bruch's membrane/choriocapillaris complex. Mol Aspects Med 33, 295-317 (2012).

121. Liu, B. et al. Complement component C5a promotes expression of IL-22 and IL-17 from human T cells and its implication in age-related macular degeneration. J Transl Med 9, 1-12 (2011).

122. Wu, K.H., Madigan, M.C., Billson, F.A. & Penfold, P.L. Differential expression of GFAP in early v late AMD: a quantitative analysis. Br J Ophthalmol 87, 1159-66 (2003).

123. Mansour, H. et al. Aging-related changes in astrocytes in the rat retina: imbalance between cell proliferation and cell death reduces astrocyte availability. Aging Cell 7, 526-40 (2008).

124. Telegina, D.V., Kozhevnikova, O.S. & Kolosova, N.G. Changes in Retinal Glial Cells with Age and during Development of Age-Related Macular Degeneration. Biochemistry (Mosc) 83, 1009-1017 (2018).

125. Miller, J.W. VEGF: From Discovery to Therapy: The Champalimaud Award Lecture. Transl Vis Sci Technol 5, 9 (2016).

126. Argon laser photocoagulation for senile macular degeneration. Results of a randomized clinical trial. Arch Ophthalmol 100, 912-8 (Macular Photocoagulation Study Group, 1982).

127. Bressler, N.M. Photodynamic therapy of subfoveal choroidal neovascularization in age-related macular degeneration with verteporfin: two-year results of 2 randomized clinical trials-tap report 2. Arch Ophthalmol 119, 198-207 (2001).

128. Wormald, R., Evans, J., Smeeth, L. & Henshaw, K. Photodynamic therapy for neovascular age-related macular degeneration. Cochrane Database Syst Rev, Cd002030 (2003).

129. Ammar, M.J., Hsu, J., Chiang, A., Ho, A.C. & Regillo, C.D. Age-related macular degeneration therapy: a review. Curr Opin Ophthalmol 31, 215-221 (2020).

130. Guimaraes, T.A.C., Georgiou, M., Bainbridge, J.W.B. & Michaelides, M. Gene therapy for neovascular age-related macular degeneration: rationale, clinical trials and future directions. Br J Ophthalmol 105, 151-157 (2021).

131. Heier, J.S. et al. Intravitreous injection of AAV2-sFLT01 in patients with advanced neovascular age-related macular degeneration: a phase 1, open-label trial. Lancet 390, 50-61 (2017).

132. Rakoczy, E.P. et al. Three-Year Follow-Up of Phase 1 and 2a rAAV.sFLT-1 Subretinal Gene Therapy Trials for Exudative Age-Related Macular Degeneration. Am J Ophthalmol 204, 113-123 (2019).

133. Askou, A.L., Jakobsen, T.S. & Corydon, T.J. Retinal gene therapy: an eye-opener of the 21st century. Gene Ther 28, 209-216 (2021).

134. Armento, A., Ueffing, M. & Clark, S.J. The complement system in age-related macular degeneration. Cell Mol Life Sci 78, 4487-4505 (2021).

135. Liao, D.S. et al. Complement C3 Inhibitor Pegcetacoplan for Geographic Atrophy Secondary to Age-Related Macular Degeneration: A Randomized Phase 2 Trial. Ophthalmology 127, 186-195 (2020).

136. Jaffe, G.J. et al. C5 Inhibitor Avacincaptad Pegol for Geographic Atrophy Due to Age-Related Macular Degeneration: A Randomized Pivotal Phase 2/3 Trial. Ophthalmology 128, 576-586 (2021).

137. Dreismann, A.K. et al. Functional expression of complement factor I following AAV-mediated gene delivery in the retina of mice and human cells. Gene Ther 28, 265-276 (2021).

138. Klaver, C.C. et al. Genetic risk of age-related maculopathy. Population-based familial aggregation study. Arch Ophthalmol 116, 1646-51 (1998).

139. Seddon, J.M., Ajani, U.A. & Mitchell, B.D. Familial aggregation of age-related maculopathy. Am J Ophthalmol 123, 199-206 (1997).

140. Seddon, J.M., Cote, J., Page, W.F., Aggen, S.H. & Neale, M.C. The US twin study of age-related macular degeneration: relative roles of genetic and environmental influences. Arch Ophthalmol 123, 321-7 (2005).

141. Hammond, C.J. et al. Genetic influence on early age-related maculopathy: a twin study. Ophthalmology 109, 730-6 (2002).

142. Seddon, J.M., Santangelo, S.L., Book, K., Chong, S. & Cote, J. A genomewide scan for age-related macular degeneration provides evidence for linkage to several chromosomal regions. Am J Hum Genet 73, 780-90 (2003).

143. Fisher, S.A. et al. Meta-analysis of genome scans of age-related macular degeneration. Hum Mol Genet 14, 2257-64 (2005).

144. Uffelmann, E. et al. Genome-wide association studies. Nature Reviews Methods Primers 1, 59 (2021).

145. Buniello, A. et al. The NHGRI-EBI GWAS Catalog of published genome-wide association studies, targeted arrays and summary statistics 2019. Nucleic Acids Res 47, D1005-d1012 (2019).

146. Pritchard, J.K. & Przeworski, M. Linkage disequilibrium in humans: models and data. Am J Hum Genet 69, 1-14 (2001).

147. Reich, D.E. et al. Linkage disequilibrium in the human genome. Nature 411, 199-204 (2001).

148. Slatkin, M. Linkage disequilibrium--understanding the evolutionary past and mapping the medical future. Nat Rev Genet 9, 477-85 (2008).

149. Pearson, T.A. & Manolio, T.A. How to interpret a genome-wide association study. Jama 299, 1335-44 (2008).

150. Uffelmann, E. & Posthuma, D. Emerging Methods and Resources for Biological Interrogation of Neuropsychiatric Polygenic Signal. Biol Psychiatry 89, 41-53 (2021).

151. Gallagher, M.D. & Chen-Plotkin, A.S. The Post-GWAS Era: From Association to Function. Am J Hum Genet 102, 717-730 (2018).

152. Schaid, D.J., Chen, W. & Larson, N.B. From genome-wide associations to candidate causal variants by statistical fine-mapping. Nat Rev Genet 19, 491-504 (2018).

153. Yang, J. et al. Conditional and joint multiple-SNP analysis of GWAS summary statistics identifies additional variants influencing complex traits. Nat Genet 44, 369-75, s1-3 (2012).

154. Spain, S.L. & Barrett, J.C. Strategies for fine-mapping complex traits. Hum Mol Genet 24, R111-9 (2015).

155. Stephens, M. & Balding, D.J. Bayesian statistical methods for genetic association studies. Nat Rev Genet 10, 681-90 (2009).

156. Cannon, M.E. & Mohlke, K.L. Deciphering the Emerging Complexities of Molecular Mechanisms at GWAS Loci. Am J Hum Genet 103, 637-653 (2018).

157. Cano-Gamez, E. & Trynka, G. From GWAS to Function: Using Functional Genomics to Identify the Mechanisms Underlying Complex Diseases. Front Genet 11, 424 (2020).

158. Sun, B.B. et al. Genetic associations of protein-coding variants in human disease. Nature 603, 95-102 (2022).

159. Ward, L.D. & Kellis, M. Interpreting noncoding genetic variation in complex traits and human disease. Nat Biotechnol 30, 1095-106 (2012).

160. Maurano, M.T. et al. Systematic localization of common disease-associated variation in regulatory DNA. Science 337, 1190-5 (2012).

161. Zhu, Y., Tazearslan, C. & Suh, Y. Challenges and progress in interpretation of non-coding genetic variants associated with human disease. Exp Biol Med (Maywood) 242, 1325-1334 (2017).

162. Zhang, F. & Lupski, J.R. Non-coding genetic variants in human disease. Hum Mol Genet 24, R102-10 (2015).

163. Yaspan, B.L. et al. Genetic analysis of biological pathway data through genomic randomization. Hum Genet 129, 563-71 (2011).

164. Phan, L. et al. "ALFA: Allele Frequency Aggregator." National Center for Biotechnology Information, U.S. National Library of Medicine www.ncbi.nlm.nih.gov/snp/docs/gsr/alfa/. (2020).

165. Anderson, D.H. et al. Vitronectin gene expression in the adult human retina. Invest Ophthalmol Vis Sci 40, 3305-15 (1999).

166. Hageman, G.S., Mullins, R.F., Russell, S.R., Johnson, L.V. & Anderson, D.H. Vitronectin is a constituent of ocular drusen and the vitronectin gene is expressed in human retinal pigmented epithelial cells. Faseb j 13, 477-84 (1999).

167. Pruim, R.J. et al. LocusZoom: regional visualization of genome-wide association scan results. Bioinformatics 26, 2336-7 (2010).

168. Huang, J.S. et al. A vitronectin M381T polymorphism increases risk of hemangioblastoma in patients with VHL gene defect. J Mol Med (Berl) 87, 613-22 (2009).

169. Ripatti, P. et al. Polygenic Hyperlipidemias and Coronary Artery Disease Risk. Circ Genom Precis Med 13, e002725 (2020).

170. Richardson, T.G. et al. Evaluating the relationship between circulating lipoprotein lipids and apolipoproteins with risk of coronary heart disease: A multivariable Mendelian randomisation analysis. PLoS Med 17, e1003062 (2020).

171. Yu, J.H. et al. The Plasma Levels and Polymorphisms of Vitronectin Predict Radiation Pneumonitis in Patients With Lung Cancer Receiving Thoracic Radiation Therapy. Int J Radiat Oncol Biol Phys 110, 757-765 (2021).

172. Luciano, M. et al. Whole genome association scan for genetic polymorphisms influencing information processing speed. Biol Psychol 86, 193-202 (2011).

173. Surendran, P. et al. Discovery of rare variants associated with blood pressure regulation through meta-analysis of 1.3 million individuals. Nat Genet 52, 1314-1332 (2020).

174. Yoneda, A., Ogawa, H., Kojima, K. & Matsumoto, I. Characterization of the ligand binding activities of vitronectin: interaction of vitronectin with lipids and identification of the binding domains for various ligands using recombinant domains. Biochemistry 37, 6351-60 (1998).

175. Vaisar, T. et al. Shotgun proteomics implicates protease inhibition and complement activation in the antiinflammatory properties of HDL. J Clin Invest 117, 746-56 (2007).

176. Tomasini, B.R. & Mosher, D.F. Vitronectin. Prog Hemost Thromb 10, 269-305 (1991).

177. Preissner, K.T. & Reuning, U. Vitronectin in vascular context: facets of a multitalented matricellular protein. Semin Thromb Hemost 37, 408-24 (2011).

178. Preissner, K.T. Structure and biological role of vitronectin. Annu Rev Cell Biol 7, 275-310 (1991).

179. Seiffert, D., Keeton, M., Eguchi, Y., Sawdey, M. & Loskutoff, D.J. Detection of vitronectin mRNA in tissues and cells of the mouse. Proc Natl Acad Sci U S A 88, 9402-6 (1991).

180. Walker, D.G. & McGeer, P.L. Vitronectin expression in Purkinje cells in the human cerebellum. Neurosci Lett 251, 109-12 (1998).

181. Dufourcq, P. et al. Vitronectin expression and interaction with receptors in smooth muscle cells from human atheromatous plaque. Arterioscler Thromb Vasc Biol 18, 168-76 (1998).

182. Ozaki, S., Johnson, L.V., Mullins, R.F., Hageman, G.S. & Anderson, D.H. The human retina and retinal pigment epithelium are abundant sources of vitronectin mRNA. Biochem Biophys Res Commun 258, 524-9 (1999).

183. Xu, D., Baburaj, K., Peterson, C.B. & Xu, Y. Model for the three-dimensional structure of vitronectin: predictions for the multi-domain protein from threading and docking. Proteins 44, 312-20 (2001).

184. Mayasundari, A., Whittemore, N.A., Serpersu, E.H. & Peterson, C.B. The solution structure of the N-terminal domain of human vitronectin: proximal sites that regulate fibrinolysis and cell migration. J Biol Chem 279, 29359-66 (2004).

185. Seiffert, D., Ciambrone, G., Wagner, N.V., Binder, B.R. & Loskutoff, D.J. The somatomedin B domain of vitronectin. Structural requirements for the binding and stabilization of active type 1 plasminogen activator inhibitor. J Biol Chem 269, 2659-66 (1994).

186. Zhou, A., Huntington, J.A., Pannu, N.S., Carrell, R.W. & Read, R.J. How vitronectin binds PAI-1 to modulate fibrinolysis and cell migration. Nat Struct Biol 10, 541-4 (2003).

187. Wei, Y. et al. Identification of the urokinase receptor as an adhesion receptor for vitronectin. J Biol Chem 269, 32380-8 (1994).

188. Deng, G., Curriden, S.A., Hu, G., Czekay, R.P. & Loskutoff, D.J. Plasminogen activator inhibitor-1 regulates cell adhesion by binding to the somatomedin B domain of vitronectin. J Cell Physiol 189, 23-33 (2001).

189. Zhou, A. Functional structure of the somatomedin B domain of vitronectin. Protein Sci 16, 1502-8 (2007).

190. Pytela, R., Pierschbacher, M.D. & Ruoslahti, E. A 125/115-kDa cell surface receptor specific for vitronectin interacts with the arginine-glycine-aspartic acid adhesion sequence derived from fibronectin. Proc Natl Acad Sci U S A 82, 5766-70 (1985).

191. Felding-Habermann, B. & Cheresh, D.A. Vitronectin and its receptors. Curr Opin Cell Biol 5, 864-8 (1993).

192. Schvartz, I., Seger, D. & Shaltiel, S. Vitronectin. Int J Biochem Cell Biol 31, 539-44 (1999).

193. Meredith, J.E., Jr. et al. The regulation of growth and intracellular signaling by integrins. Endocr Rev 17, 207-20 (1996).

194. Savill, J., Dransfield, I., Hogg, N. & Haslett, C. Vitronectin receptor-mediated phagocytosis of cells undergoing apoptosis. Nature 343, 170-3 (1990).

195. Shin, K. et al. Structure of human Vitronectin C-terminal domain and interaction with Yersinia pestis outer membrane protein Ail. Sci Adv 5, eaax5068 (2019).

196. Singh, B., Su, Y.C. & Riesbeck, K. Vitronectin in bacterial pathogenesis: a host protein used in complement escape and cellular invasion. Mol Microbiol 78, 545-60 (2010).

197. Puster, L.O. et al. Characterization of an Extensive Interface on Vitronectin for Binding to Plasminogen Activator Inhibitor-1: Adoption of Structure in an Intrinsically Disordered Region. Biochemistry 58, 5117-5134 (2019).

198. Chu, Y., Bucci, J.C. & Peterson, C.B. Identification of a PAI-1-binding site within an intrinsically disordered region of vitronectin. Protein Sci 29, 494-508 (2020).

199. Kost, C., Stüber, W., Ehrlich, H.J., Pannekoek, H. & Preissner, K.T. Mapping of binding sites for heparin, plasminogen activator inhibitor-1, and plasminogen to vitronectin's heparin-binding region reveals a novel vitronectin-dependent feedback mechanism for the control of plasmin formation. J Biol Chem 267, 12098-105 (1992).

200. de Boer, H.C., Preissner, K.T., Bouma, B.N. & de Groot, P.G. Binding of vitronectin-thrombin-antithrombin III complex to human endothelial cells is mediated by the heparin binding site of vitronectin. J Biol Chem 267, 2264-8 (1992).

201. Milis, L., Morris, C.A., Sheehan, M.C., Charlesworth, J.A. & Pussell, B.A. Vitronectin-mediated inhibition of complement: evidence for different binding sites for C5b-7 and C9. Clin Exp Immunol 92, 114-9 (1993).

202. Shin, K. et al. Calcium and hydroxyapatite binding site of human vitronectin provides insights to abnormal deposit formation. Proc Natl Acad Sci U S A 117, 18504-18510 (2020).

203. Sheehan, M., Morris, C.A., Pussell, B.A. & Charlesworth, J.A. Complement inhibition by human vitronectin involves non-heparin binding domains. Clin Exp Immunol 101, 136-41 (1995).

204. Seger, D. & Shaltiel, S. Evidence showing that the two-chain form of vitronectin is produced in the liver by a selective furin cleavage. FEBS Lett 480, 169-74 (2000).

205. Stockmann, A., Hess, S., Declerck, P., Timpl, R. & Preissner, K.T. Multimeric vitronectin. Identification and characterization of conformation-dependent self-association of the adhesive protein. J Biol Chem 268, 22874-82 (1993).

206. Seiffert, D. & Schleef, R.R. Two functionally distinct pools of vitronectin (Vn) in the blood circulation: identification of a heparin-binding competent population of Vn within platelet alpha-granules. Blood 88, 552-60 (1996).

207. Seiffert, D. Constitutive and regulated expression of vitronectin. Histol Histopathol 12, 787-97 (1997).

208. Gibson, A.D. & Peterson, C.B. Full-length and truncated forms of vitronectin provide insight into effects of proteolytic processing on function. Biochim Biophys Acta 1545, 289-304 (2001).

209. Shirinifard, A. et al. Adhesion failures determine the pattern of choroidal neovascularization in the eye: a computer simulation study. PLoS Comput Biol 8, e1002440 (2012).

210. Nita, M., Strzałka-Mrozik, B., Grzybowski, A., Mazurek, U. & Romaniuk, W. Age-related macular degeneration and changes in the extracellular matrix. Med Sci Monit 20, 1003-16 (2014).

211. Yeo, N.J.Y., Chan, E.J.J. & Cheung, C. Choroidal Neovascularization: Mechanisms of Endothelial Dysfunction. Front Pharmacol 10, 1363 (2019).

212. Takada, Y., Ye, X. & Simon, S. The integrins. Genome Biol 8, 215 (2007).

213. Madsen, C.D., Ferraris, G.M., Andolfo, A., Cunningham, O. & Sidenius, N. uPAR-induced cell adhesion and migration: vitronectin provides the key. J Cell Biol 177, 927-39 (2007).

214. Ferraris, G.M. et al. The interaction between uPAR and vitronectin triggers ligand-independent adhesion signalling by integrins. Embo j 33, 2458-72 (2014).

215. Ayloo, S. et al. Pericyte-to-endothelial cell signaling via vitronectin-integrin regulates blood-CNS barrier. Neuron (2022).

216. Wu, M.H., Ustinova, E. & Granger, H.J. Integrin binding to fibronectin and vitronectin maintains the barrier function of isolated porcine coronary venules. J Physiol 532, 785-91 (2001).

217. Kanse, S.M., Matz, R.L., Preissner, K.T. & Peter, K. Promotion of leukocyte adhesion by a novel interaction between vitronectin and the beta2 integrin Mac-1 (alphaMbeta2, CD11b/CD18). Arterioscler Thromb Vasc Biol 24, 2251-6 (2004).

218. McNally, A.K., Jones, J.A., Macewan, S.R., Colton, E. & Anderson, J.M. Vitronectin is a critical protein adhesion substrate for IL-4-induced foreign body giant cell formation. J Biomed Mater Res A 86, 535-43 (2008).

219. Noh, H., Hong, S. & Huang, S. Role of urokinase receptor in tumor progression and development. Theranostics 3, 487-95 (2013).

220. Burgos-Panadero, R., Noguera, I., Cañete, A., Navarro, S. & Noguera, R. Vitronectin as a molecular player of the tumor microenvironment in neuroblastoma. BMC Cancer 19, 479 (2019).

221. Li, R. et al. Vitronectin regulation of vascular endothelial growth factor-mediated angiogenesis. J Vasc Res 51, 110-7 (2014).

222. Hammes, H.P., Brownlee, M., Jonczyk, A., Sutter, A. & Preissner, K.T. Subcutaneous injection of a cyclic peptide antagonist of vitronectin receptor-type integrins inhibits retinal neovascularization. Nat Med 2, 529-33 (1996).

223. Fox, C.R. & Parks, G.D. Complement Inhibitors Vitronectin and Clusterin Are Recruited from Human Serum to the Surface of Coronavirus OC43-Infected Lung Cells through Antibody-Dependent Mechanisms. Viruses 14(2021).

224. Mahmood, N., Mihalcioiu, C. & Rabbani, S.A. Multifaceted Role of the Urokinase-Type Plasminogen Activator (uPA) and Its Receptor (uPAR): Diagnostic, Prognostic, and Therapeutic Applications. Front Oncol 8, 24 (2018).

225. Mondino, A., Resnati, M. & Blasi, F. Structure and function of the urokinase receptor. Thromb Haemost 82 Suppl 1, 19-22 (1999).

226. Sillen, M. & Declerck, P.J. Targeting PAI-1 in Cardiovascular Disease: Structural Insights Into PAI-1 Functionality and Inhibition. Front Cardiovasc Med 7, 622473 (2020).

227. Deng, G., Royle, G., Wang, S., Crain, K. & Loskutoff, D.J. Structural and functional analysis of the plasminogen activator inhibitor-1 binding motif in the somatomedin B domain of vitronectin. J Biol Chem 271, 12716-23 (1996).

228. Kjøller, L. et al. Plasminogen activator inhibitor-1 represses integrin- and vitronectin-mediated cell migration independently of its function as an inhibitor of plasminogen activation. Exp Cell Res 232, 420-9 (1997).

229. Czekay, R.P., Aertgeerts, K., Curriden, S.A. & Loskutoff, D.J. Plasminogen activator inhibitor-1 detaches cells from extracellular matrices by inactivating integrins. J Cell Biol 160, 781-91 (2003).

230. Preissner, K.T. & Müller-Berghaus, G. Neutralization and binding of heparin by S protein/vitronectin in the inhibition of factor Xa by antithrombin III. Involvement of an inducible heparin-binding domain of S protein/vitronectin. J Biol Chem 262, 12247-53 (1987).

231. Li, M. et al. Comprehensive analysis of gene expression in human retina and supporting tissues. Hum Mol Genet 23, 4001-14 (2014).

232. Dejana, E., Conforti, G., Zanetti, A., Lampugnani, M.G., Marchisio, P.C. Receptors for Extracellular Matrix Proteins in Endothelial Cells. Catravas, J.D., Gillis, C.N., Ryan, U.S. (eds) Vascular Endothelium; Springer, Boston, MA. (1989).

233. Johnson, L.V., Leitner, W.P., Staples, M.K. & Anderson, D.H. Complement activation and inflammatory processes in Drusen formation and age related macular degeneration. Exp Eye Res 73, 887-96 (2001).

234. Gong, J. et al. Stem cell-derived retinal pigment epithelium from patients with age-related macular degeneration exhibit reduced metabolism and matrix interactions. Stem Cells Transl Med 9, 364-376 (2020).

235. Acar, I.E. et al. Semi-Quantitative Multiplex Profiling of the Complement System Identifies Associations of Complement Proteins with Genetic Variants and Metabolites in Age-Related Macular Degeneration. J Pers Med 11(2021).

236. Coronado, B.N.L. et al. Novel Possible Protein Targets in Neovascular Age-Related Macular Degeneration: A Pilot Study Experiment. Front Med (Lausanne) 8, 692272 (2021).

237. Tollefsen, D.M., Weigel, C.J. & Kabeer, M.H. The presence of methionine or threonine at position 381 in vitronectin is correlated with proteolytic cleavage at arginine 379. J Biol Chem 265, 9778-81 (1990).

238. Kubota, K., Hayashi, M., Oishi, N. & Sakaki, Y. Polymorphism of the human vitronectin gene causes vitronectin blood type. Biochem Biophys Res Commun 167, 1355-60 (1990).

239. Chain, D., Korc-Grodzicki, B., Kreizman, T. & Shaltiel, S. The phosphorylation of the two-chain form of vitronectin by protein kinase A is heparin dependent. FEBS Lett 269, 221-5 (1990).

240. Korc-Grodzicki, B., Tauber-Finkelstein, M. & Shaltiel, S. Platelet stimulation releases a cAMP-dependent protein kinase that specifically phosphorylates a plasma protein. Proc Natl Acad Sci U S A 85, 7541-5 (1988).

241. Chain, D., Korc-Grodzicki, B., Kreizman, T. & Shaltiel, S. Endogenous cleavage of the Arg-379-Ala-380 bond in vitronectin results in a distinct conformational change which 'buries' Ser-378, its site of phosphorylation by protein kinase A. Biochem J 274 (Pt 2), 387-94 (1991).

242. Sane, D.C. et al. Highly sulfated glycosaminoglycans augment the cross-linking of vitronectin by guinea pig liver transglutaminase. Functional studies of the cross-linked vitronectin multimers. J Biol Chem 265, 3543-8 (1990).

243. Sun, B.B. et al. Genomic atlas of the human plasma proteome. Nature 558, 73-79 (2018).

244. Strunz, T., Kiel, C., Sauerbeck, B.L. & Weber, B.H.F. Learning from Fifteen Years of Genome-Wide Association Studies in Age-Related Macular Degeneration. Cells 9(2020).

245. Livak, K.J. & Schmittgen, T.D. Analysis of relative gene expression data using real-time quantitative PCR and the 2(-Delta Delta C(T)) Method. Methods 25, 402-8 (2001).

246. Biasella, F., Plössl, K., Karl, C., Weber, B.H.F. & Friedrich, U. Altered Protein Function Caused by AMD-associated Variant rs704 Links Vitronectin to Disease Pathology. Invest Ophthalmol Vis Sci 61, 2 (2020).

247. Quinn, R.H. & Miller, S.S. Ion transport mechanisms in native human retinal pigment epithelium. Invest Ophthalmol Vis Sci 33, 3513-27 (1992).

248. Sonoda, S. et al. A protocol for the culture and differentiation of highly polarized human retinal pigment epithelial cells. Nat Protoc 4, 662-73 (2009).

249. Ferrer, M. et al. A multiplex high-throughput gene expression assay to simultaneously detect disease and functional markers in induced pluripotent stem cell-derived retinal pigment epithelium. Stem Cells Transl Med 3, 911-22 (2014).

250. Kingston, R.E., Chen, C.A. & Okayama, H. Calcium phosphate transfection. Curr Protoc Immunol Chapter 10, Unit 10.13 (2001).

251. Gómez, N.M., Tamm, E.R. & Strauβ, O. Role of bestrophin-1 in store-operated calcium entry in retinal pigment epithelium. Pflugers Arch 465, 481-95 (2013).

252. van Mourik, J.A., Lawrence, D.A. & Loskutoff, D.J. Purification of an inhibitor of plasminogen activator (antiactivator) synthesized by endothelial cells. J Biol Chem 259, 14914-21 (1984).

253. Andreasen, P.A. et al. Plasminogen activator inhibitor from human fibrosarcoma cells binds urokinase-type plasminogen activator, but not its proenzyme. J Biol Chem 261, 7644-51 (1986).

254. Zeheb, R., Rafferty, U.M., Rodriguez, M.A., Andreasen, P. & Gelehrter, T.D. Immunoaffinity purification of HTC rat hepatoma cell plasminogen activator-inhibitor-1. Thromb Haemost 58, 1017-23 (1987).

255. Le Magueresse-Battistoni, B., Pernod, G., Sigillo, F., Kolodié, L. & Benahmed, M. Plasminogen activator inhibitor-1 is expressed in cultured rat Sertoli cells. Biol Reprod 59, 591-8 (1998).

256. Bradford, M.M. A rapid and sensitive method for the quantitation of microgram quantities of protein utilizing the principle of protein-dye binding. Anal Biochem 72, 248-54 (1976).

257. Chain, D., Kreizman, T., Shapira, H. & Shaltiel, S. Plasmin cleavage of vitronectin. Identification of the site and consequent attenuation in binding plasminogen activator inhibitor-1. FEBS Lett 285, 251-6 (1991).

258. Kost, C., Benner, K., Stockmann, A., Linder, D. & Preissner, K.T. Limited plasmin proteolysis of vitronectin. Characterization of the adhesion protein as morpho-regulatory and angiostatin-binding factor. Eur J Biochem 236, 682-8 (1996).

259. McLenachan, S. et al. Bioengineered Bruch's-like extracellular matrix promotes retinal pigment epithelial differentiation. Biochem Biophys Rep 10, 178-185 (2017).

260. Liang, C.C., Park, A.Y. & Guan, J.L. In vitro scratch assay: a convenient and inexpensive method for analysis of cell migration in vitro. Nat Protoc 2, 329-33 (2007).

261. Ponce, M.L. Tube formation: an in vitro matrigel angiogenesis assay. Methods Mol Biol 467, 183-8 (2009).

262. Carpentier, G. Angiogenesis Analyzer for ImageJ. ImageJ News. Available at: http://image.bio.methods.free.fr/ImageJ/?Angiogenesis-Analyzer-for-ImageJ&lang. Accessed on 16 November 2020. (2012).

263. Mosmann, T. Rapid colorimetric assay for cellular growth and survival: application to proliferation and cytotoxicity assays. J Immunol Methods 65, 55-63 (1983).

264. Kuma, A. et al. The role of autophagy during the early neonatal starvation period. Nature 432, 1032-6 (2004).

265. Szatmari-Toth, M. et al. Clearance of autophagy-associated dying retinal pigment epithelial cells - a possible source for inflammation in age-related macular degeneration. Cell Death Dis 7, e2367 (2016).

266. Kabeya, Y. et al. LC3, a mammalian homologue of yeast Apg8p, is localized in autophagosome membranes after processing. Embo j 19, 5720-8 (2000).

267. Skibo, Y.V. et al. Induction of apoptosis and autophagy in T-lymphocytes of patients with Systemic Lupus Erythematosus. Kazan medical journal 101, 347-355 (2020).

268. Schnichels, S. et al. Retina in a dish: Cell cultures, retinal explants and animal models for common diseases of the retina. Prog Retin Eye Res 81, 100880 (2021).

269. Forest, D.L., Johnson, L.V. & Clegg, D.O. Cellular models and therapies for age-related macular degeneration. Dis Model Mech 8, 421-7 (2015).

270. Chen, L.J. et al. Microfluidic co-cultures of retinal pigment epithelial cells and vascular endothelial cells to investigate choroidal angiogenesis. Sci Rep 7, 3538 (2017).

271. Dridi, S. et al. ERK1/2 activation is a therapeutic target in age-related macular degeneration. Proc Natl Acad Sci U S A 109, 13781-6 (2012).

272. Zhang, Z.Y., Bao, X.L., Cong, Y.Y., Fan, B. & Li, G.Y. Autophagy in Age-Related Macular Degeneration: A Regulatory Mechanism of Oxidative Stress. Oxid Med Cell Longev 2020, 2896036 (2020).

273. Dunaief, J.L., Dentchev, T., Ying, G.S. & Milam, A.H. The role of apoptosis in age-related macular degeneration. Arch Ophthalmol 120, 1435-42 (2002).

274. Hanus, J., Anderson, C. & Wang, S. RPE necroptosis in response to oxidative stress and in AMD. Ageing Res Rev 24, 286-98 (2015).

275. Ferrell, J.E., Jr. & Bhatt, R.R. Mechanistic studies of the dual phosphorylation of mitogen-activated protein kinase. J Biol Chem 272, 19008-16 (1997).

276. Pearson, G. et al. Mitogen-activated protein (MAP) kinase pathways: regulation and physiological functions. Endocr Rev 22, 153-83 (2001).

277. Lamalice, L., Le Boeuf, F. & Huot, J. Endothelial cell migration during angiogenesis. Circ Res 100, 782-94 (2007).

278. Ramjaun, A.R. & Hodivala-Dilke, K. The role of cell adhesion pathways in angiogenesis. Int J Biochem Cell Biol 41, 521-30 (2009).

279. Klettner, A. et al. Cellular and molecular mechanisms of age-related macular degeneration: from impaired autophagy to neovascularization. Int J Biochem Cell Biol 45, 1457-67 (2013).

280. Zhao, S. et al. H2O2 treatment or serum deprivation induces autophagy and apoptosis in naked mole-rat skin fibroblasts by inhibiting the PI3K/Akt signaling pathway. Oncotarget 7, 84839-84850 (2016).

281. Moreira, E.F., Cai, H., Tezel, T.H., Fields, M.A. & Del Priore, L.V. Reengineering Human Bruch's Membrane Increases Rod Outer Segment Phagocytosis by Human Retinal Pigment Epithelium. Transl Vis Sci Technol 4, 10 (2015).

282. Frantz, C., Stewart, K.M. & Weaver, V.M. The extracellular matrix at a glance. J Cell Sci 123, 4195-200 (2010).

283. Kremlitzka, M. et al. Functional analyses of rare genetic variants in complement component C9 identified in patients with age-related macular degeneration. Hum Mol Genet 27, 2678-2688 (2018).

284. de Jong, S. et al. Systemic complement levels in patients with age-related macular degeneration carrying rare or low-frequency variants in the CFH gene. Hum Mol Genet 31, 455-470 (2022).

285. Strunnikova, N.V. et al. Transcriptome analysis and molecular signature of human retinal pigment epithelium. Hum Mol Genet 19, 2468-86 (2010).

286. Sharma, K., Sharma, N.K., Singh, R. & Anand, A. Exploring the role of VEGF in Indian Age related macular degeneration. Ann Neurosci 22, 232-7 (2015).

287. Declerck, P.J. et al. Purification and characterization of a plasminogen activator inhibitor 1 binding protein from human plasma. Identification as a multimeric form of S protein (vitronectin). J Biol Chem 263, 15454-61 (1988).

288. Royle, G., Deng, G., Seiffert, D. & Loskutoff, D.J. A method for defining binding sites involved in protein-protein interactions: analysis of the binding of plasminogen activator inhibitor 1 to the somatomedin domain of vitronectin. Anal Biochem 296, 245-53 (2001).

289. Mahmoud, A. & Risk, K. Evaluation of Homocysteine and Plasminogen Activator Inhibitor-1 Changes in Age Related Macular Degeneration. Bulletin of Egyptian Society for Physiological Sciences 28, 253-264 (2008).

290. Lambert, V. et al. Influence of plasminogen activator inhibitor type 1 on choroidal neovascularization. Faseb j 15, 1021-7 (2001).

291. Lambert, V. et al. Dose-dependent modulation of choroidal neovascularization by plasminogen activator inhibitor type I: implications for clinical trials. Invest Ophthalmol Vis Sci 44, 2791-7 (2003).

292. Biasella, F. et al. Vitronectin and Its Interaction with PAI-1 Suggests a Functional Link to Vascular Changes in AMD Pathobiology. Cells 11(2022).

293. Lin, Z. et al. Structural basis for recognition of urokinase-type plasminogen activator by plasminogen activator inhibitor-1. J Biol Chem 286, 7027-32 (2011).

294. Lane, J. et al. Impacts of impaired face perception on social interactions and quality of life in age-related macular degeneration: A qualitative study and new community resources. PLoS One 13, e0209218 (2018).

295. Cimarolli, V.R. et al. Anxiety and depression in patients with advanced macular degeneration: current perspectives. Clin Ophthalmol 10, 55-63 (2016).

296. Johnson, A.D., Wang, D. & Sadee, W. Polymorphisms affecting gene regulation and mRNA processing: broad implications for pharmacogenetics. Pharmacol Ther 106, 19-38 (2005).

297. Degtyareva, A.O., Antontseva, E.V. & Merkulova, T.I. Regulatory SNPs: Altered Transcription Factor Binding Sites Implicated in Complex Traits and Diseases. Int J Mol Sci 22(2021).

298. Kato, K. et al. LMNA Missense Mutation Causes Nonsense-Mediated mRNA Decay and Severe Dilated Cardiomyopathy. Circ Genom Precis Med 13, 435-443 (2020).

299. GTEx Consortium. The GTEx Consortium atlas of genetic regulatory effects across human tissues. Science 369, 1318-1330 (2020; https://gtexportal.org/home/snp/rs704, accessed on 14 May 2020).

300. Tuller, T. et al. An evolutionarily conserved mechanism for controlling the efficiency of protein translation. Cell 141, 344-54 (2010).

301. Cannarozzi, G. et al. A role for codon order in translation dynamics. Cell 141, 355-67 (2010).

302. Benson, D.A., Karsch-Mizrachi, I., Lipman, D.J., Ostell, J. & Wheeler, D.L. GenBank. Nucleic Acids Res 33, D34-8 (2005).

303. Fu, J., Dang, Y., Counter, C. & Liu, Y. Codon usage regulates human KRAS expression at both transcriptional and translational levels. J Biol Chem 293, 17929-17940 (2018).

304. Frydman, J., Nimmesgern, E., Ohtsuka, K. & Hartl, F.U. Folding of nascent polypeptide chains in a high molecular mass assembly with molecular chaperones. Nature 370, 111-7 (1994).

305. Lodish, H.F. Transport of secretory and membrane glycoproteins from the rough endoplasmic reticulum to the Golgi. A rate-limiting step in protein maturation and secretion. J Biol Chem 263, 2107-10 (1988).

306. Hurtley, S.M. & Helenius, A. Protein oligomerization in the endoplasmic reticulum. Annu Rev Cell Biol 5, 277-307 (1989).

307. Lee, W.S., Jennings, B.C., Doray, B. & Kornfeld, S. Disease-causing missense mutations within the N-terminal transmembrane domain of GlcNAc-1-phosphotransferase impair endoplasmic reticulum translocation or Golgi retention. Hum Mutat 41, 1321-1328 (2020).

308. Kirchner, F. et al. Molecular insights into arrhythmogenic right ventricular cardiomyopathy caused by plakophilin-2 missense mutations. Circ Cardiovasc Genet 5, 400-11 (2012).

309. Nakayama, K. Furin: a mammalian subtilisin/Kex2p-like endoprotease involved in processing of a wide variety of precursor proteins. Biochem J 327 (Pt 3), 625-35 (1997).

310. Hu, Y. et al. NMR-Based Methods for Protein Analysis. Anal Chem 93, 1866-1879 (2021).

311. Kelly, S.M., Jess, T.J. & Price, N.C. How to study proteins by circular dichroism. Biochim Biophys Acta 1751, 119-39 (2005).

312. Gao, K., Oerlemans, R. & Groves, M.R. Theory and applications of differential scanning fluorimetry in early-stage drug discovery. Biophys Rev 12, 85-104 (2020).

313. François, P.P. et al. Vitronectin interaction with glycosaminoglycans. Kinetics, structural determinants, and role in binding to endothelial cells. J Biol Chem 274, 37611-9 (1999).

314. Wilkins-Port, C.E., Sanderson, R.D., Tominna-Sebald, E. & McKeown-Longo, P.J. Vitronectin's basic domain is a syndecan ligand which functions in trans to regulate vitronectin turnover. Cell Commun Adhes 10, 85-103 (2003).

315. Kjøller, L. & Hall, A. Rac mediates cytoskeletal rearrangements and increased cell motility induced by urokinase-type plasminogen activator receptor binding to vitronectin. J Cell Biol 152, 1145-57 (2001).

316. Kyosseva, S.V. Targeting MAPK Signaling in Age-Related Macular Degeneration. Ophthalmol Eye Dis 8, 23-30 (2016).

317. Farazdaghi, M.K. & Ebrahimi, K.B. Role of the Choroid in Age-related Macular Degeneration: A Current Review. J Ophthalmic Vis Res 14, 78-87 (2019).

318. Kim, J., Lee, Y.J. & Won, J.Y. Molecular Mechanisms of Retinal Pigment Epithelium Dysfunction in Age-Related Macular Degeneration. Int J Mol Sci 22(2021).

319. Isik, F.F., Gibran, N.S., Jang, Y.C., Sandell, L. & Schwartz, S.M. Vitronectin decreases microvascular endothelial cell apoptosis. J Cell Physiol 175, 149-55 (1998).

320. Martínez-Morales, J.R., Martí, E., Frade, J.M. & Rodríguez-Tébar, A. Developmentally regulated vitronectin influences cell differentiation, neuron survival and process outgrowth in the developing chicken retina. Neuroscience 68, 245-53 (1995).

321. Zhang, D. et al. Integrin $\alpha v \beta 5$ inhibition protects against ischemia-reperfusion-induced lung injury in an autophagy-dependent manner. Am J Physiol Lung Cell Mol Physiol 313, L384-l394 (2017).

322. Goyal, U. & Ta, M. A novel role of vitronectin in promoting survival of mesenchymal stem cells under serum deprivation stress. Stem Cell Res Ther 11, 181 (2020).

323. Berra, E. et al. Signaling angiogenesis via p42/p44 MAP kinase and hypoxia. Biochem Pharmacol 60, 1171-8 (2000).

324. Hecquet, C., Lefevre, G., Valtink, M., Engelmann, K. & Mascarelli, F. Activation and role of MAP kinase-dependent pathways in retinal pigment epithelial cells: ERK and RPE cell proliferation. Invest Ophthalmol Vis Sci 43, 3091-8 (2002).

325. Pyakurel, A. et al. Loss of Extracellular Signal-Regulated Kinase 1/2 in the Retinal Pigment Epithelium Leads to RPE65 Decrease and Retinal Degeneration. Mol Cell Biol 37(2017).

326. Quan, J.H. et al. VEGF Production Is Regulated by the AKT/ERK1/2 Signaling Pathway and Controls the Proliferation of Toxoplasma gondii in ARPE-19 Cells. Front Cell Infect Microbiol 10, 184 (2020).

327. Ricard, N. et al. Endothelial ERK1/2 signaling maintains integrity of the quiescent endothelium. J Exp Med 216, 1874-1890 (2019).

328. Makarev, E. et al. Pathway activation profiling reveals new insights into age-related macular degeneration and provides avenues for therapeutic interventions. Aging (Albany NY) 6, 1064-75 (2014).

329. Lu, Z. & Xu, S. ERK1/2 MAP kinases in cell survival and apoptosis. IUBMB Life 58, 621-31 (2006).

330. Sawe, N., Steinberg, G. & Zhao, H. Dual roles of the MAPK/ERK1/2 cell signaling pathway after stroke. J Neurosci Res 86, 1659-69 (2008).

331. Jin, Y.J. et al. Fibronectin and vitronectin induce AP-1-mediated matrix metalloproteinase-9 expression through integrin α(5)β(1)/α(v)β(3)-dependent Akt, ERK and JNK signaling pathways in human umbilical vein endothelial cells. Cell Signal 23, 125-34 (2011).

332. Hazawa, M. et al. Vitronectin improves cell survival after radiation injury in human umbilical vein endothelial cells. FEBS Open Bio 2, 334-8 (2012).

333. Sergé, A. The Molecular Architecture of Cell Adhesion: Dynamic Remodeling Revealed by Videonanoscopy. Front Cell Dev Biol 4, 36 (2016).

334. Gumbiner, B.M. Cell adhesion: the molecular basis of tissue architecture and morphogenesis. Cell 84, 345-57 (1996).

335. Hayman, E.G., Pierschbacher, M.D., Suzuki, S. & Ruoslahti, E. Vitronectin--a major cell attachment-promoting protein in fetal bovine serum. Exp Cell Res 160, 245-58 (1985).

336. Bale, M.D., Wohlfahrt, L.A., Mosher, D.F., Tomasini, B. & Sutton, R.C. Identification of vitronectin as a major plasma protein adsorbed on polymer surfaces of different copolymer composition. Blood 74, 2698-706 (1989).

337. Sillen, M. & Declerck, P.J. A Narrative Review on Plasminogen Activator Inhibitor-1 and Its (Patho)Physiological Role: To Target or Not to Target? Int J Mol Sci 22(2021).

338. Simpson, A.J., Booth, N.A., Moore, N.R. & Bennett, B. Distribution of plasminogen activator inhibitor (PAI-1) in tissues. J Clin Pathol 44, 139-43 (1991).

339. Bartha, K., Declerck, P.J., Moreau, H., Nelles, L. & Collen, D. Synthesis and secretion of plasminogen activator inhibitor 1 by human endothelial cells in vitro. Effect of active site mutagenized tissue-type plasminogen activator. J Biol Chem 266, 792-7 (1991).

340. Philips, M., Juul, A.G. & Thorsen, S. Human endothelial cells produce a plasminogen activator inhibitor and a tissue-type plasminogen activator-inhibitor complex. Biochim Biophys Acta 802, 99-110 (1984).

341. Stefansson, S. et al. Inhibition of angiogenesis in vivo by plasminogen activator inhibitor-1. J Biol Chem 276, 8135-41 (2001).

342. Mahabeleshwar, G.H., Feng, W., Reddy, K., Plow, E.F. & Byzova, T.V. Mechanisms of integrin-vascular endothelial growth factor receptor cross-activation in angiogenesis. Circ Res 101, 570-80 (2007).

343. Somanath, P.R., Malinin, N.L. & Byzova, T.V. Cooperation between integrin alphavbeta3 and VEGFR2 in angiogenesis. Angiogenesis 12, 177-85 (2009).

344. Soldi, R. et al. Role of alphavbeta3 integrin in the activation of vascular endothelial growth factor receptor-2. Embo j 18, 882-92 (1999).

345. Brakenhielm, E. Substrate matters: reciprocally stimulatory integrin and VEGF signaling in endothelial cells. Circ Res 101, 536-8 (2007).

346. Stefansson, S. & Lawrence, D.A. The serpin PAI-1 inhibits cell migration by blocking integrin alpha V beta 3 binding to vitronectin. Nature 383, 441-3 (1996).

347. Brandal, S., Blake, C.M., Sullenger, B.A. & Fortenberry, Y.M. Effects of plasminogen activator inhibitor-1-specific RNA aptamers on cell adhesion, motility, and tube formation. Nucleic Acid Ther 21, 373-81 (2011).

348. Wang, L. et al. Glycation of vitronectin inhibits VEGF-induced angiogenesis by uncoupling VEGF receptor-2-αvβ3 integrin cross-talk. Cell Death Dis 6, e1796 (2015).

349. Croset, A. et al. Differences in the glycosylation of recombinant proteins expressed in HEK and CHO cells. J Biotechnol 161, 336-48 (2012).

350. Yi, M., Sakai, T., Fassler, R. & Ruoslahti, E. Antiangiogenic proteins require plasma fibronectin or vitronectin for in vivo activity. Proc Natl Acad Sci U S A 100, 11435-8 (2003).

351. Gebb, C., Hayman, E.G., Engvall, E. & Ruoslahti, E. Interaction of vitronectin with collagen. J Biol Chem 261, 16698-703 (1986).

352. Akama, T. et al. Immunological characterization of human vitronectin and its binding to glycosaminoglycans. J Biochem 100, 1343-51 (1986).

353. Lane, D.A. et al. Structural requirements for the neutralization of heparin-like saccharides by complement S protein/vitronectin. J Biol Chem 262, 16343-8 (1987).

354. Date, K., Sakagami, H. & Yura, K. Regulatory properties of vitronectin and its glycosylation in collagen fibril formation and collagen-degrading enzyme cathepsin K activity. Sci Rep 11, 12023 (2021).

355. Sabatelli, P. et al. Collagen VI deficiency affects the organization of fibronectin in the extracellular matrix of cultured fibroblasts. Matrix Biol 20, 475-86 (2001).

356. Katagiri, Y., Brew, S.A. & Ingham, K.C. All six modules of the gelatin-binding domain of fibronectin are required for full affinity. J Biol Chem 278, 11897-902 (2003).

357. Vakonakis, I. et al. Motogenic sites in human fibronectin are masked by long range interactions. J Biol Chem 284, 15668-75 (2009).

358. Gildner, C.D., Roy, D.C., Farrar, C.S. & Hocking, D.C. Opposing effects of collagen I and vitronectin on fibronectin fibril structure and function. Matrix Biol 34, 33-45 (2014).

359. Pankov, R. et al. Integrin dynamics and matrix assembly: tensin-dependent translocation of alpha(5)beta(1) integrins promotes early fibronectin fibrillogenesis. J Cell Biol 148, 1075-90 (2000).

360. Hocking, D.C., Sottile, J., Reho, T., Fässler, R. & McKeown-Longo, P.J. Inhibition of fibronectin matrix assembly by the heparin-binding domain of vitronectin. J Biol Chem 274, 27257-64 (1999).

361. Zhang, Q. et al. Functional beta1-integrins release the suppression of fibronectin matrix assembly by vitronectin. J Biol Chem 274, 368-75 (1999).

362. Bae, E., Sakai, T. & Mosher, D.F. Assembly of exogenous fibronectin by fibronectin-null cells is dependent on the adhesive substrate. J Biol Chem 279, 35749-59 (2004).

363. Vial, D., Monaghan-Benson, E. & McKeown-Longo, P.J. Coordinate regulation of fibronectin matrix assembly by the plasminogen activator system and vitronectin in human osteosarcoma cells. Cancer Cell Int 6, 8 (2006).

364. Harumiya, S., Jung, S.K., Sakano, Y. & Fujimoto, D. Interaction of human plasma fibronectin with alpha-elastin. J Biochem 113, 710-4 (1993).

365. Meng, L.H. & Chen, Y.X. Lipid accumulation and protein modifications of Bruch's membrane in age-related macular degeneration. Int J Ophthalmol 14, 766-773 (2021).

366. Bergen, A.A. et al. On the origin of proteins in human drusen: The meet, greet and stick hypothesis. Prog Retin Eye Res 70, 55-84 (2019).

367. Podack, E.R., Preissner, K.T. & Müller-Eberhard, H.J. Inhibition of C9 polymerization within the SC5b-9 complex of complement by S-protein. Acta Pathol Microbiol Immunol Scand Suppl 284, 89-96 (1984).

368. Koustasa Mishra, P.K., Rajan, P. & Joshi, P. Complement C9 binding site and the anti-microbial activity of caprine vitronectin are localized in close proximity in the N-terminal region of the protein. Microb Pathog 149, 104111 (2020).

369. Fields, M.A. et al. Extracellular matrix nitration alters growth factor release and activates bioactive complement in human retinal pigment epithelial cells. PLoS One 12, e0177763 (2017).

370. Clark, S.J. et al. Impaired binding of the age-related macular degeneration-associated complement factor H 402H allotype to Bruch's membrane in human retina. J Biol Chem 285, 30192-202 (2010).

371. Day, A.J., Clark, S.J. & Bishop, P.N. Understanding the molecular basis of age-related macular degeneration and how the identification of new mechanisms may aid the development of novel therapies. Expert Review of Ophthalmology 6, 123-128 (2011).

372. Clark, S.J. et al. Identification of factor H-like protein 1 as the predominant complement regulator in Bruch's membrane: implications for age-related macular degeneration. J Immunol 193, 4962-70 (2014).

373. Keir, L.S. et al. VEGF regulates local inhibitory complement proteins in the eye and kidney. J Clin Invest 127, 199-214 (2017).

374. Hutchings, H., Ortega, N. & Plouët, J. Extracellular matrix-bound vascular endothelial growth factor promotes endothelial cell adhesion, migration, and survival through integrin ligation. Faseb j 17, 1520-2 (2003).

375. You, W.K. & Stallcup, W.B. Localization of VEGF to Vascular ECM Is an Important Aspect of Tumor Angiogenesis. Cancers (Basel) 9(2017).

376. Wijelath, E.S. et al. Novel vascular endothelial growth factor binding domains of fibronectin enhance vascular endothelial growth factor biological activity. Circ Res 91, 25-31 (2002).

377. Wijelath, E.S. et al. Heparin-II domain of fibronectin is a vascular endothelial growth factor-binding domain: enhancement of VEGF biological activity by a singular growth factor/matrix protein synergism. Circ Res 99, 853-60 (2006).

378. Isogai, C. et al. Plasminogen activator inhibitor-1 promotes angiogenesis by stimulating endothelial cell migration toward fibronectin. Cancer Res 61, 5587-94 (2001).

379. Wu, J. et al. Plasminogen activator inhibitor-1 inhibits angiogenic signaling by uncoupling vascular endothelial growth factor receptor-2-αVβ3 integrin cross talk. Arterioscler Thromb Vasc Biol 35, 111-20 (2015).

380. Czekay, R.P. & Loskutoff, D.J. Plasminogen activator inhibitors regulate cell adhesion through a uPAR-dependent mechanism. J Cell Physiol 220, 655-63 (2009).

381. Barnes, D.W. & Silnutzer, J. Isolation of human serum spreading factor. J Biol Chem 258, 12548-52 (1983).

382. Hayman, E.G., Pierschbacher, M.D., Ohgren, Y. & Ruoslahti, E. Serum spreading factor (vitronectin) is present at the cell surface and in tissues. Proc Natl Acad Sci U S A 80, 4003-7 (1983).

383. Seiffert, D. & Loskutoff, D.J. Type 1 plasminogen activator inhibitor induces multimerization of plasma vitronectin. A suggested mechanism for the generation of the tissue form of vitronectin in vivo. J Biol Chem 271, 29644-51 (1996).

384. Minor, K.H. & Peterson, C.B. Plasminogen activator inhibitor type 1 promotes the self-association of vitronectin into complexes exhibiting altered incorporation into the extracellular matrix. J Biol Chem 277, 10337-45 (2002).

385. Dickey, S.W., Baker, R.P., Cho, S. & Urban, S. Proteolysis inside the membrane is a rate-governed reaction not driven by substrate affinity. Cell 155, 1270-81 (2013).

386. Preissner, K.T. Specific binding of plasminogen to vitronectin. Evidence for a modulatory role of vitronectin on fibrin(ogen)-induced plasmin formation by tissue plasminogen activator. Biochem Biophys Res Commun 168, 966-71 (1990).

387. Grulich-Henn J, Mullerberghaus G & Preissner KT. The influence of growth substratum and cell activation on the deposition of plasminogen activator inhibitor-1 in the extracellular matrix of human endothelial cells. Fibrinolysis 6: 131-137(1992).

388. Underwood, P.A. & Bean, P.A. The Effect of Vitronectin and Other Extracellular Matrix Molecules on Endothelial Expansion and Plasminogen Activation. Cells and materials 6, 20 (1996).

389. Simon, D.I., Xu, H. & Vaughan, D.E. Cathepsin D-like aspartyl protease activity mediates the degradation of tissue-type plasminogen activator/plasminogen activator inhibitor-1 complexes in human monocytes. Biochim Biophys Acta 1268, 143-51 (1995).

390. Seiffert, D., Mimuro, J., Schleef, R.R. & Loskutoff, D.J. Interactions between type 1 plasminogen activator inhibitor, extracellular matrix and vitronectin. Cell Differ Dev 32, 287-92 (1990).

391. Olson, D. et al. Internalization of the urokinase-plasminogen activator inhibitor type-1 complex is mediated by the urokinase receptor. J Biol Chem 267, 9129-33 (1992).

392. Gettins, P.G. & Dolmer, K. The High Affinity Binding Site on Plasminogen Activator Inhibitor-1 (PAI-1) for the Low Density Lipoprotein Receptor-related Protein (LRP1) Is Composed of Four Basic Residues. J Biol Chem 291, 800-12 (2016).

393. Podor, T.J. et al. Accumulation of type 1 plasminogen activator inhibitor and vitronectin at sites of cellular necrosis and inflammation. Ann N Y Acad Sci 667, 173-7 (1992).

394. Inuzuka, S. et al. The significance of colocalization of plasminogen activator inhibitor-1 and vitronectin in hepatic fibrosis. Scand J Gastroenterol 32, 1052-60 (1997).

395. Stoop, A.A., Lupu, F. & Pannekoek, H. Colocalization of thrombin, PAI-1, and vitronectin in the atherosclerotic vessel wall: A potential regulatory mechanism of thrombin activity by PAI-1/vitronectin complexes. Arterioscler Thromb Vasc Biol 20, 1143-9 (2000).

396. Eitzman, D.T., Westrick, R.J., Nabel, E.G. & Ginsburg, D. Plasminogen activator inhibitor-1 and vitronectin promote vascular thrombosis in mice. Blood 95, 577-80 (2000).

397. Peng, L., Bhatia, N., Parker, A.C., Zhu, Y. & Fay, W.P. Endogenous vitronectin and plasminogen activator inhibitor-1 promote neointima formation in murine carotid arteries. Arterioscler Thromb Vasc Biol 22, 934-9 (2002).

398. Wiman, B., Almquist, A., Sigurdardottir, O. & Lindahl, T. Plasminogen activator inhibitor 1 (PAI) is bound to vitronectin in plasma. FEBS Lett 242, 125-8 (1988).

399. Völker, W., Hess, S., Vischer, P. & Preissner, K.T. Binding and processing of multimeric vitronectin by vascular endothelial cells. J Histochem Cytochem 41, 1823-32 (1993).

400. McLeod, D.S. et al. Relationship between RPE and choriocapillaris in age-related macular degeneration. Invest Ophthalmol Vis Sci 50, 4982-91 (2009).

401.   Chirco, K.R., Sohn, E.H., Stone, E.M., Tucker, B.A. & Mullins, R.F. Structural and molecular changes in the aging choroid: implications for age-related macular degeneration. Eye (Lond) 31, 10-25 (2017).

402.   Grant, M.B. et al. Plasminogen activator inhibitor (PAI)-1 overexpression in retinal microvessels of PAI-1 transgenic mice. Invest Ophthalmol Vis Sci 41, 2296-302 (2000).

403.   Grunwald, J.E., Metelitsina, T.I., Dupont, J.C., Ying, G.S. & Maguire, M.G. Reduced foveolar choroidal blood flow in eyes with increasing AMD severity. Invest Ophthalmol Vis Sci 46, 1033-8 (2005).

404.   Lipecz, A. et al. Microvascular contributions to age-related macular degeneration (AMD): from mechanisms of choriocapillaris aging to novel interventions. Geroscience 41, 813-845 (2019).

405.   Czekay, R.P. et al. PAI-1: An Integrator of Cell Signaling and Migration. Int J Cell Biol 2011, 562481 (2011).

406.   Tang, C.H. & Wei, Y. The urokinase receptor and integrins in cancer progression. Cell Mol Life Sci 65, 1916-32 (2008).

407.   McMahon, G.A. et al. Plasminogen activator inhibitor-1 regulates tumor growth and angiogenesis. J Biol Chem 276, 33964-8 (2001).

408.   Basu, A., Menicucci, G., Maestas, J., Das, A. & McGuire, P. Plasminogen activator inhibitor-1 (PAI-1) facilitates retinal angiogenesis in a model of oxygen-induced retinopathy. Invest Ophthalmol Vis Sci 50, 4974-81 (2009).

409.   Bhatwadekar, A.D., Kansara, V., Luo, Q. & Ciulla, T. Anti-integrin therapy for retinovascular diseases. Expert Opin Investig Drugs 29, 935-945 (2020).

410.   Slack, R.J., Macdonald, S.J.F., Roper, J.A., Jenkins, R.G. & Hatley, R.J.D. Emerging therapeutic opportunities for integrin inhibitors. Nat Rev Drug Discov 21, 60-78 (2022).

411.   Askew, B.C., Furuya, T. & Edwards, D.S. Ocular Distribution and Pharmacodynamics of SF0166, a Topically Administered α(v)β(3) Integrin Antagonist, for the Treatment of Retinal Diseases. J Pharmacol Exp Ther 366, 244-250 (2018).

412.   Nebbioso, M. et al. Complement Mediators in Development to Treat Age-Related Macular Degeneration. Drugs Aging (2022).

List of Abbreviations

Abbreviation	Meaning
µg	*Microgram*
µl	*Microliter*
µm	*Micrometer*
µM	*Micromolar*
aa	*Amino acid*
AAV	*Adeno-associated virus*
AGEs	*Advanced glycation end products*
AMD	*Age-related macular degeneration*
ARPE-19	*Adult retinal pigment epithelium*
bp	*Base pair*
BRB	*Blood retinal barrier*
BSA	*Bovine serum albumin*
C3	*Complement component 3*
C5	*Complement component 5*
C9	*Complement component 9*
CFH	*Complement Factor H*
CFI	*Complement Factor I*
cm	*Centimeter*
dH2O	*Distilled water*
DNA	*Deoxyribonucleic Acid*
DPBS	*Dulbecco's phosphate-buffered saline*
E.Coli	*Escherichia Coli*
ECM	*Extracellular matrix*
EDTA	*Ethylenediamine tetraacetic acid*
eQTL	*Expression quantitative trait locus*
FCS	*Fetal calf serum*
g	*Gram*
GA	*Geographic atrophy*
GFP	*Green fluorescence protein*
GWAS	*Genome wide association studies*
h	*Hour*
H_2O	*Water*
H_2O_2	*Hydrogen peroxide*
HEK	*Human embryonic kidney*

hiPSC-RPE	*Human induced pluripotent stem cells derived RPE*
HUVEC	*Human umbilical vein endothelial cell*
HX	*Hemopexin*
IAMDGC	*International AMD Genomics Consortium*
IF	*Immunofluorescence*
kDa	*Kilodalton*
L	*Liter*
LB	*Lysogeny broth*
LB-Agar	*Lysogeny broth with Agar*
LD	*Linkage disequilibrium*
M	*Molar*
mAB	*Monoclonal antibody*
MAC	*Membrane attack complex*
mg	*Milligram*
min	*Minute*
ml	*Milliliter*
mM	*Millimolar*
mm	*Millimeter*
MMPs	*Matrix metalloproteinases*
mRNA	*Messenger RNA*
ng	*Nanogram*
NV-AMD	*Neovascular AMD*
pAB	*Polyclonal antibody*
PCR	*Polymerase chain reaction*
PFA	*Paraformaldehyde*
POS	*Photoreceptor outer segment*
pQTL	*Protein quantitative trait locus*
qRT-PCR	*Quantitative real-time (reverse transcription)-PCR*
RGD	*Arginine-glycine-aspartate*
RNA	*Ribonucleic acid*
ROS	*Reactive oxygen species*
RPE	*Retina pigment epithelium*
rpm	*Revolutions per minute*
RT	*Room temperature*
SDS	*Sodium dodecyl sulphate*
SDS-PAGE	*Sodium dodecyl sulphate-polyacrylamide gel electrophoresis*

sec	*Second*
SNPs	*Single nucleotide polymorphisms*
T_a	*Annealing temperature*
TBE	*Tris-borate-EDTA*
TBS	*Tris-buffered saline*
TEER	*Transepithelial electrical resistance*
TIMP3	*Tissue inhibitor of metalloproteinase 3*
TIMPs	*Tissue inhibitor of metalloproteinases*
uPA	*Urokinase plasminogen activator*
uPAR	*Urokinase plasminogen activator receptor*
V	*Volt*
v/v	*Volume per volume*
VEGF	*Vascular endothelial growth factor*
VEGFR-2	*Vascular endothelial growth factor receptor 2*
w/v	*Weight per volume*
WB	*Western blot*

List of Figures

List of Tables

Acknowledgements

This doctoral thesis would not be complete without properly thanking my supervisor, Prof. Dr. Bernhard Weber, for welcoming me to the Institute of Human Genetics at the University of Regensburg, giving me the great opportunity to work in his team and live an experience of both scientific and personal growth. In particular, I am very grateful for his continuous support in all aspects of my thesis, which together with his immense enthusiasm and knowledge in this field of study, helped, taught and inspired me a lot to pursue this project with hard work and dedication.

I would like to thank my mentors, Prof. Dr. Veronica Egger and Prof. Dr. Selim Corbacioglu, for their time and helpful comments and suggestions.

Special acknowledgement goes to the PRO RETINA Deutschland e. V. Foundation for contributing financially to this research.

I am very thankful to my group leader, Dr. Ulrike Friedrich, who from the very beginning of my doctoral project made her time and professional expertise available to me, providing me with a valuable support in planning experiments, evaluating data, or writing and designing presentations, poster, and manuscripts.

My gratitude goes to Martina Esser, for her precious technical assistance, for her support and friendship.

I wish to acknowledge my colleagues, Dr. Tobias Strunz and Dr. Christina Kiel, for sharing their professional experience and bioinformatics knowledge in a nice and fruitful collaboration for the purposes of this project. Thanks also for the many productive discussions on my research.

I would like to thank my colleague Dr. Karolina Plössl, for lending me her experience and intuition for my scientific and technical doubts especially at the beginning of this project, but also for brightening my days with delicious cakes.

A special thanks to Verena Schmid, who from day one has been an extraordinary base of support, a friend and an ideal office and laboratory mate in the most enjoyable moments but also in the most stressful ones.

To all the dear colleagues and students at the Institute of Human Genetics who, regardless of whether they were involved in this project or not, have enriched my daily life intellectually and humanely over the years, I say thank you for everything, but above all for always making me feel at home in a warm and stimulating atmosphere.

Last but not least, I would like to thank my family and all my friends for the encouragement they have given me. Though my biggest thanks go to Andrea, my husband to be and best friend, who with his love, patience and positivity has helped me through this challenging time. Grazie ami, dal profondo del mio cuore.

Selbständigkeitserklärung

Ich, Biasella Fabiola geboren am 04.04.1990 in Isernia (Italien), erkläre hiermit, dass ich die vorliegende Arbeit ohne unzulässige Hilfe Dritter und ohne Benutzung anderer als der angegebenen Hilfsmittel angefertigt habe.

Die aus anderen Quellen direkt oder indirekt übernommenen Daten und Konzepte sind unter Angabe der Quelle gekennzeichnet. Insbesondere habe ich nicht die entgeltliche Hilfe von Vermittlungs- bzw. Beratungsdiensten (Promotionsberater oder andere Personen) in Anspruch genommen.

Die Arbeit wurde bisher weder im In- noch im Ausland in gleicher oder ähnlicher Form einer anderen Prüfungsbehörde vorgelegt.

Regensburg,   _____

23.01.2023   Fabiola Biasella